Nuclear reaction analysis cross-sections measurements for Boron and Carbon.

by

Senzo Simo Miya

submitted to the faculty of science and agriculture in fulfillment or partial fulfillment for the degree of Master of Sciences in the Department of Physics at the University of Zululand.

Supervisors: Miss S. P. Segonyane
Dr C. B. Franklyn (NECSA)

Co -supervisor: Prof O. M. Ndwandwe (University of Zululand)

March 2007

Nuclear reaction analysis cross-sections measurements for Boron and Carbon.

Senzo Simo Miya

Keywords

Projectiles

Reaction Cross section

Energy loss

Nuclear reactions

Nuclear reaction analysis

Rutherford backscattering spectrometry

Straggling

Stopping Power

Stopping Cross section

Standards

Nuclear reaction analysis cross-sections measurements for Boron and Carbon.

Senzo Simo Miya

Abstract

The aim of the project was to measure nuclear reaction cross-sections for selected light elements such as Boron and Carbon for the database at Radiation Utilisation Group of Necsa. Deuteron-Induced and ^{3}He-induced reactions were performed at the 4 MV Van de Graaff accelerator at detection angles of $\Theta = 150^{\circ}$ and 135° for incident beam energies between 1.8 and 2.8 MeV. Immediate application of this study will help in determining:

1. The Boron contaminants or impurities in the raw material used for the operation of the Pebble Bed Modular Reactor
2. The isotopic composition of boron carbide, which is used as a neutron shielding at the SAFARI-1 research reactor.

Acknowledgements

I would like to pass my words of thanks to the following people and organisations:

- To **Dr C. B Franklyn** and **Miss S.P Segonyane at NECSA**, thanks for the guidance and assistance in making this work a success.

- To **Mr G. T Young at NECSA**, thanks a lot for your contribution with technical work.

- My **late parents, Mrs Sainah and Mr Dumanezwe Miya**, I wish you were still there to see how successful Your boy has become in science, by the way I mean thank you for supporting me relentlessly no matter what the situation was.

- My **big sister and brother, Bathobile and Mlekeleli**, thank you for being there for me after our parents had passed away, not forgetting my little brother, **Mxolisi** and the rest of the siblings for looking up on me, making me feel like somebody really great at all the times.

- I thank the **University of Zululand** for having faith in me, many thanks to **Prof O. M. Ndwandwe** in the Physics Department.

- My high school teachers, **Mrs M. Mpisi** and **Mrs Magubane**, and the rest of **Siyaphambili high** school staff, you people played a very huge role in my up bringing.

- I thank **NECSA** for enabling me to work on the on the project.

- Lastly, I thank **NRF** for their financial support, without a financial muscle this work would have not been a success.

Mandithi inkosi kakhulu nakuni maGcwanini amahle, boMunja, Zibewu, boBhincel' ohlangeni ngokuyibheka lenkwenkwana yenu kuze kube apha, manditsho-ke ndithi Zijekula!!!!

Declaration

I declare that *NRA cross sections measurements for boron and carbon in the incident energy range 1.8 – 2.8 MeV at an angle of 150° and 135°* is my own work, that it has not been submitted for any degree or any other university, and that all the resources I used or quoted have been indicated and acknowledged by complete references.

Senzo Simo Miya March 2007

Signed.....

Table Contents

KEYWORDS II
ABSTRACT III
ACKNOWLEDGEMENTS IV
DECLARATION V

Chapter 1 1

BACKGROUND AND INTRODUCTION 1
1.1 ELEMENTS OF INTEREST FOR THE STUDY. 2
1.2 ION BEAM ANALYSIS 3
1.2.1 MINOR INTERACTIONS 5
1.2.2 MAJOR INTERACTIONS 14
1.2.2.1 NUCLEAR REACTION ANALYSIS (NRA) 16
1.3 THESIS OUTLINE 29

Chapter 2 30

LITERATURE REVIEW 30
2.1 NUCLEAR REACTIONS FOR THE TARGETS OF ^{12}C, ^{13}C, ^{10}B AND ^{11}B. 30
2. 2. OVERVIEW 36

Chapter 3 39

RESEARCH DESIGN AND METHODOLOGY 39
3.1 DESCRIPTION OF FACILITIES 40
3.2 EXPERIMENTAL PROCEDURE 47
3.2.1 SAMPLE DESIGN. 47
3.2.2 DATA ACQUISITION AND ANALYSIS 48
3.2.3 MEASURING OF CROSS SECTIONS 49
3.3 OVERVIEW 49

Chapter 4 50

RESULTS: PRESENTATION AND DISCUSSIONS 50
4.1 SAMPLE DESCRIPTION AND CHARACTERIZATION 50
4.2 MAIN RESULTS 51
4.2.1 RESULTS OF THE D^- ON CARBON FOIL TARGET. 53
4.2.2 RESULTS OF THE $^3He^-$ ON THE CARBON FOIL TARGET. 65
4.2.4 RESULTS OF THE D^- ON BORIC ACID (HBO_3) CRYSTAL 70
4.2.5 RESULTS OF THE $^3He^-$ ON BORIC ACID (HBO_3) CRYSTAL. 90
4.2.6 RESULTS OF THE D^- ON BORON CARBIDE ($B4C/SiO_2$). 97
4.2.7 RESULTS OF THE $^3He^-$ ON B_4C/SiO_2. 116

Chapter 5 117

CONCLUSION AND DISCUSSIONS 117

List of Tables

Table 2.1: A table of cross sections calculated by Purser et al. at certain incident energy values ranging between 1.0 to 1.75 MeV [Pur63] 35

Table 2.2: Useful existing nuclear reactions data for the undertaking of study www09] 37

Table 2.3: Nuclear reactions data for oxygen and silicon within the study's required range of 0.8 - 3.0 MeV [www09] 38

Table 4.1: Kinetic energies of emitted protons for the $^{12}(d, p_0)$ reaction at 135° and 150° respectively, for incident deuteron energy E_i. All energies are in MeV 52

Table 4.2: Data collected for the $^{12}C(d, p_0)^{13}C$ reaction at 135° and 150° 55

Table 4.3: Data collected for the $^{12}C(d, p_1)^{13}C$ reaction at 135 and 150° 56

Table 4.4: Data collected for the measurements of the $^{12}C(d, p2)^{13}C$ at 135° and 150° 57

Table 4.5: Data collected for the reaction $^{12}C(d, d)^{12}C$ at 135 and 150° measurements 59

Table 4.6: Data collected at 135 and 150° for the measurements of the $^{16}O(d, p_0)^{17}O$ reaction 61

Table 4.7: Data collected for the measurements of the $^{16}O(d, p_1)^{17}O$ at 135 and 150° 62

Table 4.8: Number of counts taken from the spectra of $^{16}O(d, d)^{16}O$ at 135° and 150 64

Table 4.9: Number of counts taken from spectra for $^{12}C(^3He, p_0)^{14}N$ at 135 and 150° 66

Table 4.10: Number of counts taken from spectra for $^{12}C(^3He, p_1)^{14}N$ for measurements taken at 135 and 150 degrees. 67

Table 4.11: Number of counts taken from spectra for $^{12}C(^3He, p_2)^{14}N$ for measurements taken at 135 and 150° 68

Table 4.12: Number of counts taken from spectra for $^{12}C(^3He, 3He)^{12}C$ for measurements taken at 135 and 150 degrees 69

Table 4.13: Number of counts taken from spectra for $^{10}B(d, p_0)^{11}B$ collected at 135° and 150° 72

Table 4.14: Number of counts taken from spectra for $^{10}B(d, p_1)^{11}B$ collected at 135° and 150° 73

Table 4.15: Number of counts taken from spectra for $^{10}B(d, p_2)^{11}B$ collected at 135° and 150° 74

Table 4.16: Number of counts taken from a spectra of $^{10}B(d, p_3)^{11}B$ collected at 135° and 150° 75

Table 4.17: Number of counts taken from a spectra of $^{10}B(d, p_4)^{11}B$ collected at 135° and 150° 76

Table 4.18: Number of counts taken from a spectra of $^{11}B(d, p_0)^{12}B$ collected at 135° and 150° 78

Table 4.19: Number of counts taken from a spectrum of $^{10}B(d, \alpha_0)^{8}Be$ collected at 150° 80

Table 4.20: Number of counts taken from a spectra of $^{10}B(d, \alpha_1)^{8}Be$ reaction both at 135 and 150° respectively 81

Table 4.21: Number of counts taken from a spectra of $^{10}B(d, \alpha_2)^{8}Be$ reaction collected at 135 and 150° 82

Table 4.22: Number of counts taken from spectra of $^{10}B(d,\alpha_3)^{8}Be$ reaction at 135 and 150° .83

Table 4.23: Number of counts taken from spectra of $^{16}O(d,p_0)^{17}O$ reaction at 135 and 150° 85

Table 4.24: Number of counts taken from spectra of $^{16}O(d, p_1)^{17}O$ reaction at 135° and 150° 86

Table 4.25: Data collected for the measurements of the $^{18}O(d, \alpha_1)^{16}N$ at 135° and 150° 88

Table 4.26: Data collected for the measurements of the $^{18}O(d, \alpha_2)^{16}N$ at 135 and 150° 89

Table 4.27: Data collected for the $^{11}B(^3He, \alpha_0)^{10}B$ reaction measurements taken at 135° and 150° 91

Table 4.28: Data collected for the $^{11}B(^3He, \alpha_1)^{10}B$ reaction measurements taken at 150° 92

Table 4.29: Data collected for the $^{10}B(^3He, p_5)^{12}C$ reaction measurements taken at 150° 93

Table 4.30: Data collected for the $^{10}B(^3He, p_6)^{12}C$ reaction measurements taken at 150° 94

Table 4.31: Data collected for the $^{11}B(^3He, d_2)^{12}C$ reaction measurements taken at 150° ... 95

Table 4.32: Data collected for the $^{11}B(^3He, d_3)^{12}C$ reaction measurements taken at 150° ... 96

Table 4.33: Data collected for the $^{10}B(d, p_0)^{11}B$ reaction measurements taken at 135° and 150° 99

Table 4.34: Data collected for the $^{10}B(d, p_1)^{11}B$ reaction measurements taken at 135° and 150° 100

Table 4.35: Data collected for the $^{10}B(d, p_2)^{11}B$ reaction measurements taken at 135° and 150° 101

Table 4.36: Data collected for the $^{10}B(d, p_3)^{11}B$ reaction measurements taken at 135° and 150° 102

Table 4.37: Data collected for the $^{10}B(d, p_4)^{11}B$ reaction measurements taken at 135° and 150° 103

Table 4.38: Data collected for the $^{11}B(d, p_0)^{12}B$ reaction measurements taken at 135° and 150°.....105

Table 4.39: Data collected for the $^{10}B(d, a_1)^{8}Be$ reaction measurements taken at 135 and 150°.....106

Table 4.40: Data collected for the $^{12}C(d, p_0)^{13}C$ reaction measurements taken at 135 and 150°.....108

Table 4.41: Data collected for the $^{12}C(d, p_1)^{13}C$ reaction measurements taken at 135 and 150°.....109

Table 4.42: Data collected for the $^{12}C(d, p_2)^{13}C$ reaction measurements taken at 135 and 150°.....110

Table 4.43: Data collected for the $^{13}C(d, p_0)^{14}C$ reaction measurements taken at 135 and 150°.....111

Table 4.44: Data collected for the $^{16}O(d, p_0)^{17}O$ reaction measurements taken at 135 and 150°.....113

Table 4.45: Data collected for the $^{16}O(d, p_1)^{17}O$ reaction measurements taken at 135 and 150°.....114

Table 4.46: Data collected for the $^{16}O(d, a_0)^{14}N$ reaction measurements taken at 135 and 150°.....115

List of Figures

Figure 1.1: A schematic diagram illustrating the change of energy and velocity of the incident particles after colliding with an atom [Bir89].....2

Figure 1.2: A schematic diagram showing how the beam loses energy as it traverses a sample [Tes95].....6

Figure 1.3: schematic diagram showing scattering of particles in nuclear reactions.....18

Figure 1.4: A Schematic diagram illustrating the scattering geometry used for NRA and RBS experiments [Bir89].....22

Figure 2.1: A graph of cross section vs. incident beam energy for ^{12}C (d, p_0) ^{13}C [Kok06]...32

Figure 2.2: A graph differential cross section vs. incident beam energy for ^{12}C (^3He, p_1) ^{14}N [Ter97].....33

Figure 3.1: A schematic diagram of showing a setup and facilities used for ion beam analysis [Chu78].....39

Figure 3.2: A picture of the target chamber.....42

Figure 3.3: A picture showing surface barrier detectors used for the current study.....44

Figure 3.4: A schematic diagram showing how the detector solid angle was attained for current study.....45

Figure 3.5: A schematic diagram of a multi-channel analyzer [Kno79].....47

Figure 3.6: An experimental setup that was used for the research.....48

Figure 4.1: Spectrum collected for a 2.4 MeV beam of deuterons detected at 135°.....53

Figure 4.2: In A is a plot of a number of detected protons against the incident beam energy from the ^{12}C(d, p_0)^{13}C reaction in the current measurements taken at 135° compared to the cross section data found by Debras et a.l [Deb77].....55

Figure 4.3: In A is plot of counts vs. incident deuteron beam energy for the ^{12}C(d, p_1)^{13}C measurements taken at 135° and in B is a plot taken at 150°.....56

Figure 4.4: In A is a plot of counts vs. beam energy for the ^{12}C(d, p_2)^{13}C measurements taken at 135° and in B is a plot for 150° measurements normalized at 1.8 MeV to the cross section data found by Kokkoris et al. [Kok06].....57

Figure 4.5: Plots of counts vs. beam energy for the ^{12}C(d, d)^{12}C measurements taken at 135 and 150° normalized to theoretical RBS plots at 2.5 and 2.4 MeV respectively..59

Figure 4.6: Plots of counts vs. beam energy for the ^{16}O(d, p_0)^{17}O measurements taken at 135° normalized to the Debras et al. cross section data at 2.5 MeV and the150° measurements respectively[Deb77].....61

Figure 4.7: Plots of counts vs. beam energy for the $^{16}O(d, p_1)^{17}O$ measurements taken at 135° normalized to the cross sections data found by Debras et al. 2.1 MeV [Deb77], and a plot of current measurements taken at 150° respectively.....62

Figure 4.8: Experimental plot of counts vs. incident beam energy for the $^{16}O(d, d)^{16}O$ measurements taken at 150° respectively normalized to the theoretical RBS measurements at 2.3 MeV.....64

Figure 4.9: A spectrum collected for the 2.6 MeV $^3He^-$ beam on the carbon foil at 150°.....65

Figure 4.10: In A is a plot of counts vs. beam energy for the $^{12}C(^3He, p_0)^{14}N$ measurements taken at 150° normalized to the cross sections data calculated by Kuan et al. at 2.7 MeV and 159.4° [Kua64].....66

Figure 4.11: A plot of counts vs. incident beam energy for the $^{12}C(^3He, p_1)^{14}N$ measurements taken at 150° normalized to Kuan et al. cross sections data taken at 159.4° at 2.4 MeV [Kua64].....67

Figure 4.12: A plot of counts vs. incident beam energy for the $^{12}C(^3He, p_2)^{14}N$ measurements taken at 150° normalized to Kuan et al. cross sections data taken at 159.4° at 2.4 MeV [Kua64], in A is a plot of 135°.....68

Figure 4.13: An experimental plot of counts vs. incident beam energy for the $^{12}C(^3He, ^3He)^{12}C$ measurements taken at 135° normalized to the RBS theoretical plot at 1.9 MeV.....69

Figure 4.14: Un-calibrated spectrum for2.6 MeV D on boric acid at 150°.....70

Figure 4.15: Experimental plots of counts vs. incident beam energy for the $^{10}B(d, p_0)^{11}B$ measurements taken at 150°.....72

Figure 4.16: Experimental plots of counts vs. incident beam energy for the $^{10}B(d, p_1)^{11}B$ measurements taken at 150°.....73

Figure 4.17: Experimental plot of counts vs. incident beam energy for the $^{10}B(d, p_2)^{11}B$ measurements taken at 150°.....74

Figure 4.18: Experimental plot of counts vs. incident beam energy for the $^{10}B(d, p_3)^{11}B$ measurements taken at 135 and 150° respectively.....75

Figure 4.19: Experimental plot of counts vs. incident beam energy for the $^{10}B(d, p_4)^{11}B$ measurements taken at 135 and 150° respectively.....76

Figure 4.20: Experimental plot of counts vs. incident beam energy for the $^{11}B(d, p_0)^{12}B$ measurements taken at 135 and 150° respectively.....78

Figure 4.21: Experimental plot of counts vs. incident beam energy for the $^{10}B(d, \alpha_0)^8Be$ measurements taken at 150°.....80

Figure 4.22: Experimental plot of counts vs. incident beam energy for the $^{10}B(d, \alpha_1)^8Be$ measurements taken at 150°.....81

Figure 4.23: Experimental plots of counts vs. incident beam energy for the $^{10}B(d, \alpha_2)^8OBe$ measurements taken at 135 and 150° respectively 82

Figure 4.24: Experimental plots of counts vs. incident beam energy for the $^{10}B(d, \alpha_3)^8Be$ measurements taken at 135 and 150° respectively 83

Figure 4.25: In A, a 135° experimental plot of counts vs. incident beam energy for the $^{16}O(d, p_0)^{17}O$, in B is a 150° experimental plot normalized to the135° Debras et al. data at 2.6 MeV [Deb77] 85

Figure 4.26: Experimental plots of counts vs. incident beam energy for the $^{16}O(d, p_1)^{17}O$ for The 135° and 150° respectively 86

Figure 4.27: Plots of counts vs. beam energy for the $^{18}O(d, \alpha_1)^{16}N$ measurements taken at 135° and 150° respectively 88

Figure: 4.28: A spectrum collected for $^3He^+$ on boric acid at 2.6 MeV and 150° 90

Figure 4.29: Experimental plots of counts vs. incident beam energy for the $^{11}B(3He, \alpha_0)^{10}B$ measurements taken at 135° and 150° respectively 91

Figure 4.30: Experimental plot of counts vs. incident beam energy for the $^{10}B(^3He, p_5)^{12}C$measurements taken at 150° 93

Figure 4.31: Experimental plot of counts vs. incident beam energy for the $^{10}B(^3He, p_6)^{12}B$ measurements taken at 150° 94

Figure 4.32: Experimental plot of counts vs. incident beam energy for the $^{11}B(^3He, d_2)^{12}C$ measurements taken at 150° 95

Figure 4.33: Experimental plot of counts vs. incident beam energy for the $^{11}B(^3He, d_3)^{12}C$ measurements taken at 150° 96

Figure 4.34: A spectrum collected for deuterons on B_4C/SiO_2 at 2.6 MeV 97

Figure 4.35: Experimental plot of counts vs. incident beam energy for the $^{10}B(d, p_{10})^{11}B$ measurements taken at 150° 99

Figure 4.36: Experimental plot of counts vs. incident beam energy for the $^{10}B(d, p_1)^{11}B$ measurements taken at 15 101

Figure 4.37: Experimental plots of counts vs. incident beam energy for the $^{10}B(d, p_2)^{11}B$ measurements taken at 135° and 150° respectively 105

Figure 4.38: Experimental plot of counts vs. incident beam energy for the $^{10}B(d, p_3)^{11}B$ measurements taken at 135° and 150° respectivel 102

Figure 4.39: Experimental plot of counts vs. incident beam energy for the $^{10}B(d, p_4)^{11}B$ measurements taken at 135° and 150° respectively 103

Figure 4.40: Experimental plot of counts vs. incident beam energy for the $^{11}B(d, p_{11})^{12}B$ measurements taken at 135° and 150° 105

Figure 4.41: Experimental plot of counts vs. incident beam energy for the $^{10}B(d, \alpha_1)^{11}B$ measurements taken at 150° 106

Figure 4.42: In A, Experimental plot of counts vs. incident beam energy for the $^{12}C(d, p_0)^{13}C$ measurements taken at 135° in B a 150° plot normalized at 2.2 MeV to the cross sections data found by Debras et al. at 135°[Deb77] 108

Figure 4.43: Experimental plot of counts vs. incident beam energy for the $^{12}C(d, p_1)^{13}C$ measurements taken at 135 and 150° respectively 109

Figure 4.44: Experimental plost of counts vs. incident beam energy for the $^{12}C(d, p_2)^{13}C$ measurements taken at 135° and a 150° plot normalized to Kokkoris et al. cross section data at 1 .8 MeV measured at 150° [Kok06] 110

Figure 4.45: Experimental plot of counts vs. incident beam energy for the $^{13}C(d, p_0)^{14}C$ measurements taken at 150° 111

Figure 4.46: Experimental plot of counts vs. incident beam energy for the $^{16}O(d, p_0)^{17}O$ measurements taken at 135°and 150°respectively 113

Figure 4.47: Experimental plot of counts vs. incident beam energy for the $^{16}O(d, p_1)^{17}O$ measurements taken at 135° normalized to Debras et al cross sections measurements at 2.1MeV and 150° respectively[Deb77] 114

Figure 4.48: Experimental plot of counts vs. incident beam energy for the $^{16}O(d, \alpha_0)^{14}N$ measurements taken at 135 and 150° respectively 115

Chapter 1

Background and Introduction

Elements like carbon, boron, nitrogen and hydrogen can be used in the surface treatment of steels, polymers and glasses since they are light elements. Surface treatment can be coatings, protective or decorative; this can be done using different techniques such as ion beam assisted deposition and ion implantation [Ter97]. In performing these surface treatments it is useful to non-destructively measure the doping composition in terms of concentration as a function of depth below the surface. One method used for determining these properties is ion beam analysis, especially Rutherford backscattering spectroscopy (RBS) and nuclear reaction analysis (NRA).

At the South African Nuclear Energy Corporation, Radiation Utilisation Group, the nuclear reactions' data for the above-mentioned elements is incomplete. Therefore, this study has been undertaken to fill some of the gaps of missing cross sections data for boron and carbon. This is done by measuring reactions cross sections of light particles (particularly deuterons and tritons) induced reactions on the above mentioned elements at 135^{o} and 150^{o} scattering angles in the 1.8 -2.8 MeV incident energy range for the nuclear data library.

This chapter gives background of the current research's elements of interest, which are boron and carbon; it goes on with the fundamental definition and basic principles of ion beam analysis and its analytical techniques such as nuclear reaction analysis it also gives the basic definition of a reaction cross section.

1.1 Elements of interest for the study.

Boron

The element boron was discovered in 1808 by French chemists, Joseph-Louis Gay-Lussac and Louis-Jacques Thenard and independently by an English chemist Sir Humphry Davy. This element occurs usually as orthoboric acid in certain volcanic spring waters. It is also found in the earth's crust whereby about 0.001% is in the form of its compounds [htt01]. Boron is also obtained by heating borax with carbon, but this is regarded as boron of low purity [htt02].

Boron has been discovered to have about nine isotopes, with the naturally occurring isotopes being ^{10}B and ^{11}B. Boron exists as 19.9% ^{10}B and 80.1% ^{11}B. All the other seven boron isotopes have very short half-lives in a way that they become less important. The element is used in pyrotechnics and flares to produce a green colour. The ^{10}B isotope is a very good neutron absorber so it is used for neutron shielding in nuclear reactors [htt02].

Since boron is a light element it can also be used to coat the walls of thermonuclear experiments for reduction of the influx of high Z impurities into the fusion plasma, then the term is called boronization. It is also used for doping of semiconductors, and boron nitride is used for hard coatings in plasma technological applications [May98].

Carbon

This element has been utilized since ancient times, it is freely found in nature in three allotropic forms, which are amorphous, graphite and diamond [www04]. Carbon naturally occurs as 98.93% ^{12}C isotope and 1.07% ^{13}C isotope while the ^{14}C sometimes also occurs due to cosmic rays. It has been regarded as the sixth most abundant element in the universe. The main source of the element is coal deposits.

---

1. Reaction cross-section is the measure of the probability of a reaction to occur

Amorphous Carbon is artificially produced by incomplete burning of carbon containing material due to the absence of oxygen. Its uses are to make pen inks, paints and rubber products, if it is pressed into shapes it is used to form the cores of most dry cell batteries [htt03].

Diamond is one of the hardest substances known; it is the third occurring form of Carbon. This form of Carbon is typically used for jewellery. Diamond tipped saw blades are made from squeezing graphite under high temperatures and pressures for several days or weeks [htt03].

Graphite is very soft to the touch so it is primarily used as a lubricant. This form of carbon occurs naturally but treating petroleum coke, in an oxygen-free oven, can also artificially produce it. The natural form occurs in two forms, which are alpha and beta, with all the artificially produced graphite in the alpha form [htt03]. This form of carbon is used for the manufacturing of fuel pebbles used for the operation of the pebble bed modular reactor [www08].

1.2 Ion Beam Analysis

When charged particles (projectiles) travelling at high speeds collide with material (hits the target) they change the direction of their initial trajectory. These collisions lead to the emission of particles (alpha, gamma rays, etc) with their energy being the characteristic of the elements constituting the sample material [www01].

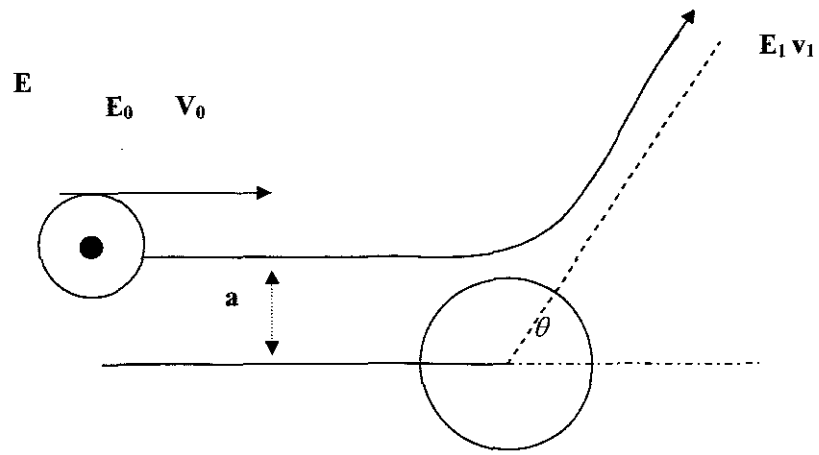

Figure 1.1: a schematic diagram illustrating the change of energy and velocity of the incident particles after colliding with an atom. E_0 and V_0 is the energy and velocity of an incident particle before collision, E_1 and V_1 is the energy and velocity after collision, a is the impact parameter then θ is the angle of scattering [Bir89].

A number of parameters determine ion-atom interactions, these parameters can be the velocity and energy of the incident particles (projectiles), atom and particle size, sample geometry and composition (stopping power) and the distance of closest approach, as shown on Figure 1.1. The principle based on these particle-atom interactions at both atomic and nuclear level is called ion beam analysis (IBA) [Bir89].

The basic principle of IBA is: when an incoming ion beam enters the surface of a thin film it loses some energy while penetrating the film, this stopping process is due to interactions of the beam with the atomic electrons in the energy shells of atoms (electronic stopping). The loss of energy can also be caused by the interactions of the beam with nuclei of the target sample (nuclear stopping).

The collisions leading to interactions are divided into two groups at nuclear level, which are nuclear elastic collisions and nuclear inelastic collisions. Nuclear elastic collisions are the ones that leave reaction products at the same state as reactants. In nuclear inelastic collisions, the reaction products are left at a state different from the one of the reactants (an excited state) [Bir89].

Ions undergo two different types of interactions, minor interactions and major interactions. Minor interactions are those controlling the slowing down of ions and perturb their trajectories as they traverse matter. Major interactions are the interactions that involve sputtering, inner shell ionisation or nuclear reactions, atomic displacements and large angle scattering. The information on the products of major interactions is the basis of the IBA applications [Bir89].

1.2.1 Minor Interactions

Under minor interactions, we find energy loss and multiple scattering, which occurs if a sample is penetrated by a beam of medium to high-energy ions. These processes' importance comes with bringing about the unique capability of deriving depth information to the IBA methods. This is because these processes only involve low energy transfer ion-atom collisions, which have only minor affects on the ion energy and direction [Bir89]. Another process that is a consequence of minor interactions is secondary electron emission, which goes with sample irradiation. Secondary electron emission can only be used as a tool for imaging in the high-energy proton microprobe.

Energy loss

In methods of material analysis using charged atomic particle beams, knowledge of the slowing down of ions in traversing matter is of fundamental importance. Depth perception comes directly after the energy lost by the probing particles and both quantitative and compositional analysis are affected by the energy loss. There are some parameters, which are dependant on energy loss processes such as stopping cross section or stopping power, straggling and multiple scattering, range and path length [Tes95].

Energy loss phenomenon involves many kinds of interactions between projectile particles, target nuclei and target electrons. Energy loss can be defined as the amount

of energy lost per unit distance traversed. The figure below shows a schematic illustration of energy loss [Tes95].

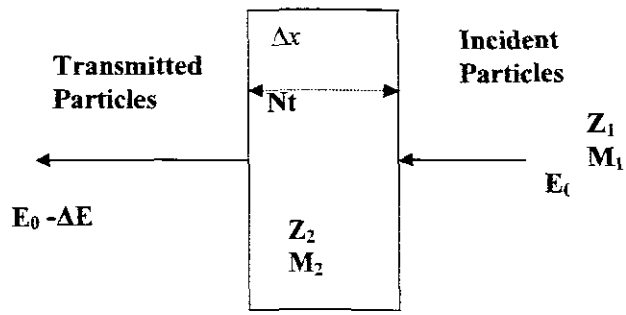

Figure 1.2: A schematic diagram showing how the beam loses energy as it traverses a sample, Z_1 and M_1 are atomic number and mass of the incident beam, Z_2 and M_2 are target atomic number and mass. ΔE is the energy lost and Δx is the target thickness corresponding to the areal density, Nt [Tes95].

This can be mathematically presented by $\frac{\Delta E}{\Delta x}$; its units are eV/$u$ m. $\frac{\Delta E}{\Delta x} \rightarrow \frac{dE}{dx}$

When $\Delta x \rightarrow 0$, with $\frac{dE}{dx}$ often-called stopping power or specific energy loss, which is sometimes denoted with S. In the literature, energy loss is sometimes denoted by ΔE.

The stopping cross-section given by $\varepsilon = (\frac{1}{N})(\frac{dE}{dx})$ or $\varepsilon = (\frac{1}{p})(\frac{dE}{dx})$, where N and p is the volume density in atoms per cubic centimetres and the mass density in grams per cubic centimetre. Sometimes ε is also called a stopping power [Tes95].

Energy loss models

These models state that the relative importance of the interaction processes between the ion and the target medium are more dependent on the ion velocity and on the ion and target atoms charges. The ions carry their electrons and tend to be neutralised by electron capture at ion velocities lower than the Bohr velocity, v_0, of the atomic electrons the nuclear energy loss dominates at these velocities. And the nuclear energy loss decreases as $\frac{1}{E}$ when the ion velocity increases.

At ion velocities higher than the Bohr velocity, the ion charge increases until all its electrons are stripped off. Then at a certain velocity, the energy loss will be proportional to the square of ion charge. This is better shown by the Betha Bloch formula:

$$\frac{dE}{dx} = NZ_2(Z_1e^2)f(\frac{E}{m_1}) \quad \ldots (1.1)$$

where $f(\frac{E}{m_1})$ is a function depending only on the target material, e is the charge of an electron, then Z_1 and Z_2 are the atomic numbers of the target and projectile particles respectively [Tes95].

Conversion methods.

The conversion methods of energy loss are units, low vs. high energies, light to heavy ions, elemental targets vs. compounds and mixtures, stopping and ΔE to depth scale and isotopes [Tes95].

i. Units

The mass of the projectile ion M_1 and the mass of the target M_2 are converted into atomic mass units (amu) [Tes95].

ii. Low vs. high energy

The nuclear stopping cross section at energy E can be calculated from:

$$\varepsilon(E) = \frac{8.462Z_1Z_2S_n(E_r)}{(M_1+M_2)(Z_1^{0.23}+Z_2^{0.23})} \; eV/10^{15}\,atoms \quad \ldots (1.2)$$

Where E_r is the reduced energy and $S_n(E_r)$ is the reduced nuclear stopping.

$$E_r = \frac{2.53M_2E}{Z_1Z_2(M_1+M_2)(Z_1^{0.23}+Z_2^{0.23})} \quad \ldots (1.3a)$$

Then for $E_r \le 30keV$ S_n becomes:

$$S_n(E_r) = \frac{\ln(1+1.1.1383E_r)}{2\left(E_r + 0.01321E_r^{0.21226} + 0.19593E_r^{0.5}\right)} \quad \ldots (1.3b)$$

for $E_r > 30keV$: $\quad S_n(E_r) = \frac{\ln(E_r)}{2E_r}$

E_r in Equation (1.3a) is evaluated then equation (1.3b) is selected for $S_n(E_r)$ then used in equation (1.2) to compute the nuclear cross section $\varepsilon_n(E)$ at an energy E. The nuclear stopping contribution becomes so small above the 200 keV/amu energy loss; it typically becomes less than 1% of the electronic stopping [Tes95].

iii. Light to heavy ions

Equation (1.1) is used to derive the stopping cross sections of two projectiles a, and b having the same velocity in a medium, then this rule is called the heavy ion rule.

$$\left[\frac{\varepsilon}{(\gamma Z_1)^2}\right]_a = \left[\frac{\varepsilon}{(\gamma Z_1)^2}\right]_b \quad \ldots (1.4)$$

where γ is the fractional effective charge, given by $\gamma = {Z_1^*(v, Z_2)}/{Z_1(v, Z_2)}$ with $Z_1^*(v, Z_2)$ being the effective charge of the ion at velocity v in the medium (Z_2). The stopping of protons (H) is used to determine the stopping cross section of a heavy ion (HI) at the same velocity. Then the stopping cross section of heavy ions is given by:

$\varepsilon_{HI} = \varepsilon_H Z_{HI}^2 \gamma_{HI}^2$

where ε_H denotes the proton stopping cross section. The high ion energy at the same energy is given by: $E_{HI} = \left({m_{HI}}/{m_H}\right) \cdot E_H$ and the higher the ion energy means the closer the fractional effective charge to 1 [Tes95].

iv. Elemental targets vs. compounds and mixtures.

If an assumption that the interaction process between ions and target elements are independent of the surrounding target atoms, then a simpler linear additivity rule of

energy loss in compounds may be used, this rule is called Bragg's rule. Considering a compound A_mB_n the Bragg's rule for the stopping cross section ε^{AB} (acme/at) for the compound can be written as $\varepsilon^{AB} = m\varepsilon^{A} + n\varepsilon^{B}$ where $m+n=1$ [Tes95].

v. Stopping and ΔE to depth scale.

In this conversion method the energy loss of $\frac{dE}{dx}$ or the stopping cross section is used to relate the energy ΔE lost by the probing ions to the thickness penetrated in the material. This calculation involves solving integrals of the form;

$$\Delta E = \int_0^x \left(\frac{dE}{dx}\right) dx \text{ or } x = \int_E^{E_0} \left(\frac{dE}{dx}\right)^{-1} dE \qquad \ldots (1.5)$$

With the former giving ΔE when the depth dependence of stopping is assumed, the latter the depth scale x for a given energy interval $\Delta E = E - E_0$.

$\frac{dE}{dx}$ Alternatively, ε may be evaluated either at ion surface energy E_0 or at some mean energy, this depends on the thickness of the target and the stopping variation in the ion energy region in question.

For thin targets the surface energy approximation yields

$\Delta E = \frac{dE}{dx}(E_0)\Delta x$ or $\Delta E = \varepsilon(E_0)Nt$, which may also be used for obtaining the mean energy $E_{av} = E_0 - \Delta E/2$ for the mean energy approximation, which then gives

$\Delta E = \frac{dE}{dx}(E_0)\Delta x$ or $\Delta E = \varepsilon(E_{av})Nt$.

Thicker targets are divided into slabs, then surface energy approximation is used in each of the slabs, i.e. the energy lost in the ith slab ΔE_i and the total ΔE in the target is calculated as; $\Delta E = \frac{dE}{dx_i}(E_i - 1)\Delta x_i$ or

$$\Delta E = \varepsilon(E_i - 1)\,(Nt)_i \qquad \ldots (1.6)$$

$$\Delta E = \sum_{1}^{n} \Delta E_i$$

Where $\varepsilon(E_i - 1)$ and $\frac{dE}{dx}(E_i - 1)$ are the stopping cross section and energy loss evaluated at the energy of the $(i-1)th$ slab ion [Tes95].

vi. Isotopes

This conversion coefficient method uses the idea that electronic stopping for a given ion x with atomic number Z_1 at an energy E/A is the same no matter what the ion mass number is. For instance, the stopping of 2 MeV $^2H^-$ ions is in this way equal to the stopping of 1 MeV $^1H^-$ ions.

In the target medium only with an average mass, M_{av} different from the natural composition for isotopic compositions, an approximation for the stopping [MeVcm^2/µg] is made by:

Stopping (medium [M_{av}, Z_2]) = Stopping (medium [M_{av}, Z_2]). (Mav / M$^-_{av}$)

where M_{av} is a parameter denoting the average mass of a medium mass of the natural isotopic composition [Tes95].

Straggling

This is due to statistical fluctuations in the number of collision processes. Straggling^2 widens the measured energy distributions and resonances and impairs depth and mass resolutions in ion beams for materials analysis [Tes95].

Models

Straggling is based on four models, these are: Bohr's theory, corrections to Bohr's theory (other models), compounds and mixtures and additivity loss fluctuations [Tes95].

i. Bohr's theory

When the energy loss width of the energy distribution is higher than the energy transferred to the atomic electrons by the beam, the distribution is close to a Gaussian. And its conditions satisfy the ones of a Gaussian formulated as

$$Nt\left[atoms/cm^2\right] \geq 2.10^{20}\frac{1}{Z_2}\left(E\left[\frac{MeV/amu}{Z_1}\right]\right)^2 \quad \ldots (1.7)$$

Here is an expression that was derived by Bohr in this regime

$$\Omega_B^2[keV^2] = 0{,}26 Z_1^2 Z_2 Nt\left[10^{18}\, at/cm^2\right] \quad \ldots (1.8)$$

Where Ω_B^2 is the Bohr value for the variance of the average energy loss fluctuation Ω (Full Width at Half Maximum height is $\equiv 2.355\Omega$). However, this fails for thick targets where energy loss during penetration exceeds 25%. In some regions where energy loss is dominated by electronic excitations, in the limits of high ion velocity the straggling becomes independent of projectile velocity [Tes95].

ii. Corrections to Bohr's theory (other models)

Bohr's theory got improved to extend its applicability to lower velocities of light ions by some other authors ($Z_1 < Z_2$), and then they came up with this correction for low velocities below $E\left[keV/amu\right] = 75Z_2$

$$\frac{\Omega^2}{\Omega_B^2} = \begin{cases} 0.5L(x) \, for E < 75Z_2\left(keV/amu\right) \\ 1, \, for E \geq 75Z_2\left(keV/amu\right) \end{cases} \quad \ldots (1.9)$$

$$L(x) = 1.36x^{\frac{1}{2}} - 0.016x^{\frac{3}{2}}$$

$$x = E\left[keV/amu\right]/(25Z_2) \quad \text{[Tes95].}$$

iii. Compound and mixtures

An approach similar to the one used for conversion method, elemental targets vs. compound mixtures, and a linear additivity rule is used for energy straggling. A

---

2. This is the spreading of beam energy as the beam traverses matter, while it slows down.

compound of composition A_mB_n for $m+n=1$ with an atom density $N^{AB}\left(atoms/cm^3\right)$ and atomic densities N_A and N_B. If an assumption is made that straggling for the elements are Ω^A and Ω^B in a layer of thickness t. Straggling in the layer of the compound is given by.

$$\frac{\left(\Omega^{AB}\right)^2}{N^{AB}t}=\frac{m\left(\Omega^A\right)^2}{N_At}+\frac{n\left(\Omega^B\right)^2}{N_Bt} \quad \ldots (1.11) \quad \text{[Tes95].}$$

iv. Additivity of energy loss fluctuations

All the Gaussian contributions to energy loss are added in quadrature. These contributions are the system resolution, Ω_{Det}, energy straggling, Ω_{Str} and beam profile, Ω_{Beam}. Then the total variance of energy loss fluctuations is given by the sum of these contributions.

$$\Omega^2_{Tot}=\Omega^2_{Det}+\Omega^2_{Str}+\Omega^2_{Beam}+\ldots \qquad \ldots (1.12)$$

This is also done for contributions to energy loss fluctuation resulting from multi-layered targets. The total variance of energy loss fluctuation is given by:

$$\Omega^2_{Tot}=\Omega^2_A+\Omega^2_B+\ldots$$

Where A and B denote successive layers in a medium, which are penetrated by ions. In target thickness with a variance Δt, the distribution is directly proportional to the energy loss fluctuation this is shown by:

$$\Omega^2_{\Delta t}=\left(dE/dx\right)^2(\Delta t)^2 \qquad \text{[Tes95].}$$

Ranges

The total distance ions traverse along the trajectory is the range along the path. The projected range can be defined as the mean depth at which ions come to a halt from the target surface. Range straggling is the width of the ions' range distribution; range distribution is characterized by higher moments such as skewness and kurtosis [Tes95].

Calculations and simulations

The range distribution calculation in range theory is regarded as a transport problem describing the motion of the ions during their slowing down to zero energy. These calculations are divided into analytical methods and simulation methods.

The analytical approach involves simple universal expressions for ion-projected ranges, R_p in the low energy region where nuclear stopping dominates. These expressions are given in terms of reduced variables, energy and length (E_r and R_r).

$$R_r = \frac{0.275N\left[10^{22}\,at/cm^3\right]M_1M_2}{(M_1+M_2)^2\left(Z_1^{0.23}+Z_2^{0.23}\right)^2} \qquad \ldots (1.13)$$

Projected range is given in terms of the reduced variables by power law expressions.

$$\begin{aligned} R_r &= 1.63E_r^{2/3} \quad for 0.01 < E_r < 0.3 \\ R_r &= 2.2E_r \qquad for 0.3 < Er < 6 \end{aligned} \qquad \ldots (1.14)$$

At the higher reduced energy region R_p is given by:

$$R_p[nm] = \frac{72(M_1+M_2)\left(Z_1^{0.23}+Z_2^{0.23}\right)}{ZZ_2M_1N\left[10^{22}\,at/cm^3\right]} \times E[keV] \quad for 0.3 < E_r < 6 \qquad \ldots (1.14)$$

The simulation approach's basis is molecular dynamic or binary collision approximation (BCA) calculations [Tes95].

Range in compounds

There are two techniques using the corresponding ranges in element materials,

a. Averaging the ranges for the ion in each element of the compound, weighted by the relative composition. For the reduced energy and length this method gives for a composite A_mB_n.

$E_r^{AB} = mE_r^A + nE_r^B$ and $R_r^{AB} = mR_r^A + nR_r^B$ where m + n = 1

b. Finding the range of the ion in a target that has an atomic number equal to the average of the atomic number in compound [Tes95].

ii. Isotopic effects

The mass number ratio is used to scale the range for different isotopes of ions ${}^{A}_{Z_1}x$ at energies E/A: $\text{Range}\left({}^{A}_{Z_1}x\right) = Range\left({}^{A}_{Z_1}x\right) \bullet \left(A'/A\right)$

In the target medium differing from the natural composition, for isotopic composition the range is approximated from:

$$Range(medium[M_{av}', Z_2]) = Range(medium[M_{ave}, Z_2]) \bullet \left(M'_{av}/M_{av}\right) \qquad \text{[Tes95]}$$

1.2.2 Major Interactions

Major interactions can be described as those determined by the emitted products particles used to give some information on target material composition. These include scattered ions, sputtered ions and atoms, recoiled atoms and de-excitation products. In the study of materials analysis, the most important products are scattered or sputtered ions, which occur only occasionally. The major processes for high-energy interactions regime are elastic scattering, nuclear reactions and inner shell ionisation. High-energy techniques are based on the use of light ions (A<5) whereas low energy uses medium to high atomic weight (A>10) [Bir89].

Low energy interactions

i. Low energy ion scattering (LEIS) is whereby elastic scattering of ions is used at energies less than 10 keV. The scattered ions' energy is given by:

$$E_{sc} = E_{inc}\left\{\left[\cos\theta \pm \left(\frac{M_2^2}{M_1^2} - \sin^2\theta\right)^{1/2}\right] \Big/ \left(1 + \frac{M_2}{M_1}\right)\right\}^2 \qquad \ldots (1.15)$$

Where M_1 and M_2 are atomic mass numbers of the incident particle

and target atom, E_{inc} is the incident energy and θ is the scattering angle. The term in brackets can be referred to as K, the kinematic factor.

ii. Ion beam modification of materials is the modification of the structure of the surface layers of a sample during low energy heavy ion irradiation. This involves four main processes, which are ion implantation, sputtering, radiation damage and ion beam mixing [Bir89].

High-energy interactions

Under this regime, there falls Rutherford's backscattering (RBS), elastic recoil detection analysis (ERDA), particle induced x-ray emission (PIXE) and nuclear reactions.

i. Rutherford or coulomb scattering: Rutherford backscattering spectrometry (RBS) is used for sample analysis. The energy of a scattered ion is given by equation (1.15).

ii. Elastic recoil analysis (ERA) uses recoiling target atoms which are detected if they get adequate energy from the projectile-target collisions. It is also used for light elements depth profiling.

iii. Inner shell ionisation: this technique is given rise by ion collisions with small impact parameters which result in emission of electrons from the shell of atoms.

Nuclear reactions are used for sample analysis then the technique is called nuclear reaction analysis (NRA) [Bir89]. The present research is based on this technique, so it is worth discussing in more detail, specifically on ion-ion reactions.

1.2.2.1 Nuclear reaction analysis (NRA)

Nuclear reactions are a very useful tool for light elements depth profiling on heavy matrix [Del05]. They are specifically more important in the profiling of deuterium in polymers [www02].

The basic principle is when projectiles undergo nuclear reactions with the nuclei of the target material, which leads to the emission of product particles.

There is one condition that is always important for nuclear reactions to occur, which is the incident particle should possess energy greater than the coulomb barrier potential. Examples of such reactions are nuclear fission reactions. Coulomb barrier potential is given by:

$$E_b = \frac{zZ(m+M)}{M(a^{\frac{1}{3}} + A^{\frac{1}{3}})} \qquad \ldots (1.16)$$

Since the mass of the incident, m is very small compared to the mass of the target nucleus, M in a way that it can be ignored then the equation becomes:

$$E = \frac{zZ}{[a^{\frac{1}{3}} + A^{\frac{1}{3}}]} \qquad \ldots (1.16\ b)$$

Where z and Z denote the atomic number of the incident and target particle respectively. The capital A and small letter a, denote the atomic mass of the incident and target particle respectively [Bir89].
Equation (1.16b) shows clearly how the coulomb barrier potential depends on Z for very light incident ions, showing how much more probable low Z reactions are likely to occur. This makes NRA to be more suitable for low Z target reactions.

The laws of conservation of charge, energy, momentum, govern nuclear reactions and nucleons number (atomic mass number). However, the law of conservation of energy is the one that plays a major role in materials analysis, which will be discussed in details under NRA kinematics.

NRA kinematics

According to Einstein the energy of a particle at rest can be calculated using the equation: $E = Mc^2$,

where M is the mass of the particle in atomic mass units (amu) and c is the speed of light, which is equal to 931.4 MeV for a 1 amu. For a reaction: $X + a \rightarrow Y + b$, a schematic diagram for this nuclear reaction is shown in figure 1.3, the total energy of the reaction can be determined from:

$$E_{total} = \sum E_{reacts} = \sum E_{products} + Q_{value} \qquad \ldots (1.17)$$

where E_{reacts} is the energy of reactants, which is for the above given by:

$\sum E_{reacts} = (M_2 + M_1) \cdot c^2$,

$E_{products}$ is the energy of products, which is for the above reaction given by:

$\sum E_{products} = (M_4 + M_3) \cdot c^2$ and Q_{value} is the amount of energy released or absorbed by the reaction depending on its sign.

$Q_{value} = (M_1 + M_2) \cdot c^2 - (M_4 + M_3) \cdot c^2$

A positive Q_{value} means the nuclear reaction releases energy whereas a negative value means absorbed energy. This value is always zero for RBS since RBS is under elastic scattering meaning the reactants and the products are in the same state. The Q_{value} differs for each state of the nucleus, for instance the reactions leaving the residual nuclei in the first excited states have much higher Q_{value} than the ones leaving nuclei in the higher excited states. The scattering geometry for NRA is shown in the figure 1.3.

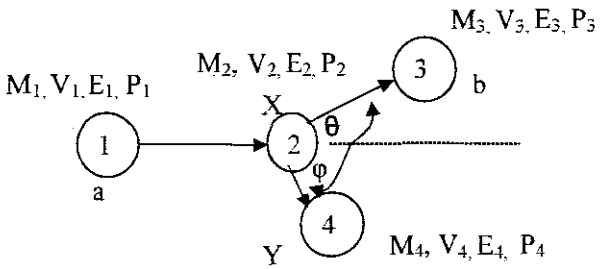

Figure 1.3: schematic diagram showing scattering of particles in nuclear reactions with a being the projectile, b the scattered particle, X is the target and Y the recoiling nucleus.

For the scattering geometry shown in Fig. 1.5, the law of conservation of energy states that the total energy should be as given by:

$$E_1 + E_2 = E_3 + E_4 - Q \qquad \ldots (1.18)$$

in the above equation E_1 is the kinetic energy of the incident particles, E_2 is the kinetic energy of the target, which is 0 since the target is stationary, E_3 is the kinetic energy of the emitted particle, E_4 is the kinetic energy of the residual nucleus And Q is the Q_{value}.

Then the law of conservation of momentum gives:

$$P_1 + P_2 = P_3 + P_4$$

Momentum along x-axis:

$$m_1 v_1 = m_3 v_3 \cos\theta + m_4 v_4 \cos\phi \qquad \ldots (1.19)$$

Momentum along y-axis:

$$0 = m_3 v_3 \sin\theta + m_4 v_4 \sin\phi \qquad \ldots (1.19b)$$

To eliminate Φ $(1.19a)^2 + (1.19b)^2$

$$m_1^2 v_1^2 - 2m_1 v_1 m_3 v_3 \cos\theta + m_3^2 v_3^2 = m_4^2 v_4^2 \cos^2\phi$$

$$m_3^2 v_3^2 = m_4^2 v_4^2 \sin^2\phi$$

This gives:

$$m_1^2 v_1^2 - 2m_1 v_1 m_3 v_3 \cos\theta + m_3^2 v_3^2 = m_4^2 v_4^2 \qquad \ldots (1.19c)$$

It is known that:

$$E = \frac{p^2}{2m} = \frac{m^2v^2}{2m}$$

Substituting $m^2v^2 = 2mE$ into (1.19c)

$$2m_1E_1 - 2\sqrt{4m_1E_1m_3E_3}\cos\theta + 2m_3E_3 = 2m_4E_4$$

Making E_4 the subject of (4)

$$E_4 = \frac{mE_1 - 2\sqrt{m_1m_3E_1E_3}\cos\theta + m_3E_3}{m_4}$$

From Eq. (1):

$$E_4 = E_1 - E_3 + Q$$

Then

$$mE_1 - 2\sqrt{m_1m_3E_1E_3}\cos\theta + m_3E_3 = (E_1 - E_3 + Q)\cdot m_4$$

$$E_3(m_3 + m_4) - \sqrt{m_1m_3E_1}\cos\theta\sqrt{E_3} - [E_1(m_4 - m_1) + m_4Q] = 0$$

Using the old equation used to solve for the roots of a function

$$x = \frac{-b \pm \sqrt{b^2 - 4ac}}{2a}$$

$$\sqrt{E_3} = \frac{2\sqrt{m_1m_3E_1}\cos\theta \pm \sqrt{4m_1m_3E_1\cos^2\theta + 4(m_3 + m_4)[E_1(m_4 - m_1) + m_4Q]}}{2(m_3 + m_4)}$$

$$\sqrt{E_3} = \frac{\sqrt{m_1m_3E_1}\cos\theta}{(m_3 + m_4)} \pm \frac{\sqrt{m_1m_3E_1\cos^2\theta + (m_3 + m_4)[E(m_4 - m_1) + m_4Q]}}{(m_3 + m_4)}$$

$$E_3 = \left[\frac{\sqrt{m_1m_3E_1}\cos\theta}{(m_3 + m_4)} \pm \frac{\sqrt{m_1m_3E_1\cos^2\theta + (m_3 + m_4)[E_1(m_4 - m_1) + m_4Q]}}{(m_3 + m_4)}\right]^2 \quad \ldots(1.20)$$

The $\pm$ sign in Eq. 1.20 is positive for all $M_2 > M_1$. In the above equation, the effect of m_2 only comes through the Q_{value}.

Abilities of NRA

What makes this technique more special than any other IBA analytical technique is that every isotope can undergo a variety of nuclear reactions, each having unique characteristics such as energy release, excitation states angular distributions and cross sections [Bir89].

This technique has some important features, which include:

- High selectivity for the determination of particular light nuclides.
- High sensitivity for many nuclides, which are difficult to determine using some other techniques.
- It can non-destructively be used to depth profile specific nuclides [Bir89].
- It can be used to analyse more than one light element in near surface layers of materials at once.

These features have earned NRA an establishment as a principal IBA method. NRA's ability to depth profile with nanometre resolution makes it to be the more suitable IBA technique for concentration determination and light elements depth profiling [Kok06].

The NRA's special case by charged particle detection is Rutherford backscattering spectroscopy (RBS) [Tes95]. These techniques (NRA and RBS) are both governed by kinematics equations and their scattering geometry is the same. Figure 1.3 shows the scattering geometry of NRA or RBS. An incident beam of energy E_0 and mass M_1 penetrates a target of thickness t and mass M_2 to a depth of Δx, and then the scattered beam has energy E_1 for RBS given by:

$$E_1 = KE_0 \quad \ldots (1.21)$$

In this equation K is the kinematic factor that gives information on the mass, concentration and the depth of the target. K is a function of M_1, M2 and θ. K is shown in equation (1.15). The RBS cross section is given by:

$$\frac{d\sigma}{d\Omega}=\left(\frac{Z_1Z_2e^2}{16\pi\varepsilon_0E_0}\right)^2\frac{4}{\sin^4\theta}\frac{\left\{\left[1-\left(\left(M_1/M_2\right)\sin\theta\right)^2\right]^{\frac{1}{2}}+\cos\theta\right\}^2}{\left[1-\left(\left(M_1/M_2\right)\sin\theta\right)^2\right]^{\frac{1}{2}}} \quad \ldots (1.22)$$

where Z_1 and Z_2 are the atomic numbers of the projectile and the target, e is the charge of an electron in coulombs, ε_0 is the permittivity of free space.

NRA's Equipment

The equipment used in NRA and RBS is the same; it includes an accelerator up to 4 MeV energy, high vacuum, surface barrier detectors, standard nuclear electronics, scattering chamber and multi-channel analyzer, although for some of the equipment parameters differ. Some properties of the NRA make it demand some special equipment, these are.

- Higher reaction products energy compared to the incident particles' energy. Lower cross sections compared to the RBS.
- The possibility of more than one reaction on a certain nucleus that can result in different particles.
- High resolution depth profiling allowed by relatively narrow resonances.
- The possible generation of neutrons especially by deuteron-induced reactions [Tes95].

NRA's Geometry and filtering of unwanted particles.

It has been previously discussed that the scattering geometry for the NRA and RBS is the same, but there is one exception in NRA that is some filtering material has to be placed in front of the detector. This is shown in figure 1.4

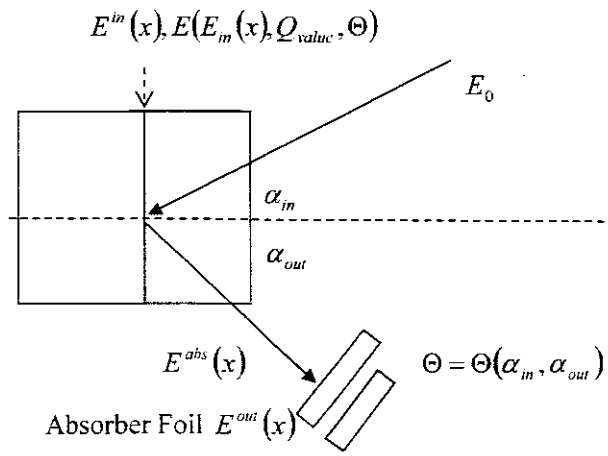

Figure 1.4: A Schematic diagram illustrating the scattering geometry used for NRA and RBS experiments. E_0 Is the energy of the incident beam, $E_{in}(x)$ is the incident particle at depth x, Q_{value} is the energy released by the reaction, $E(E_{in}(x), Q, \Theta)$ is the energy of the reaction product in the sample at depth x. $E^{out}(x)$ is the energy of the reaction product, $E^{abs}(x)$ is the energy of the product particles after penetrating the absorber foil. α_{in} And α_{out} are the angles of the incident beam and of the detector and Θ is the scattering angle [Bir89].

The energy of scattered particle can be given by:

$$E_{0out}(x) = E[E_{in}(x, Q, \theta)] - \int_0^{\frac{x}{\cos\alpha_{out}}} S_{out}(E)dx \qquad \ldots (1.23)$$

$$E_{in}(x) = E_0 - \int_0^{\frac{x}{\cos\alpha_{in}}} S_{in}(E)dx \qquad \ldots (1.23b)$$

Where x denotes the depth at which the reaction occurs, E_0 is the incident beam energy, $S_{in}(E)$ and $S_{out}(E)$ are stopping power of the incoming and outgoing particles, α_{in} and α_{out} are incident beam and detector angles respectively, with E_2 being the reaction product energy and θ is the angle of scattering [Tes95].

To filter unwanted particles five methods can be used; these are the time of flight (TOF), absorber foil, electrostatic or magnetic deflection, thin detector and coincidence techniques [Tes95].

a. Absorber foils technique.

Placing an absorber foil in front of the detector is the simplest technique to stop backscattered beam particles. In this technique a pinhole, free Mylar is usually used for the foil. After passing through the foil, the particles possess energy given by:

$$E_{abs}(x) = E_{0ut}(x) - \int_{0}^{x_{abs}} S_{abs}(E)dx \qquad \ldots (1.24)$$

Where x_{abs} is the thickness of the absorber foil, and S_{abs} (E) is the stopping power of the absorber foil.

The drawback of this technique is; the large energy straggling in the foil causes poor depth resolution [Tes95].

b. Electrostatic or magnetic deflection technique

This technique uses the effects of the electrostatic or magnetic fields on charged particles. The charged particles are deflected to some certain distances by the fields; the distance to which they are deflected depends on the charge they carry, their mass and energy.

The depth resolution of this technique is better compared to the one of the absorber foil technique, but its disadvantage is its complication so it is rarely used [Tes95].

c. Time of flight (TOF) technique

This method is used to distinguish between the particles generated simultaneously; it is based on the simultaneous measurement of the detector particles' velocity and energy from which the mass of the particle can be calculated. The velocity of the particle can be measured by measuring the time elapsed between the detection of the particle in two sequential detectors at a fixed distance from one another.

The disadvantage of this technique is the requirement of a two-dimensional multi-channel analyzer, which is hardly found in every ion beam laboratory. Another disadvantage of this technique is even though the multi-channel analyzer cannot detect all the low-energy particles, some particles can reach the detector and it can be killed [Tes95].

d. Thin detector technique

Thin detector technique is used when proton and alpha peaks overlap with the alpha spectrum containing more information than the proton spectrum. The opposite of this is the absorber foil technique used to filter out alpha particles. Here filtering is achieved with a well-chosen detector thickness due to differences in the stopping powers between particles and protons. Expensive detectors specifically designed to measure energy loss are used to filter alpha particles [Tes95].

e. Coincidence technique

This technique uses coincidence arrangement for the detection of back-scattered particles. In coincidence arrangement, different detectors are used to detect two reaction products. The detectors are spread in a way that a particle that cannot be reachable for the other detector can be detected on the other detector; this is due to the coincidence requirement.

Coincidence technique's disadvantage is it is limited to transmission geometries due to the conservation of momentum [Tes95].

Nuclear reaction cross section

In the present research. NRA is used to measure nuclear reaction cross sections for Boron and Carbon. As reaction cross section has previously been defined as the measure of the probability of a reaction to occur, denoted by σ, in barns ($1b = 10^{-28}m^2$). This can mathematically be presented by:

$$P = \sigma d x \ldots (1.25)$$

Where P is the probability of a reaction to occur, dx is the real density of an atom in g/cm^3 [Tes95].The cross section can be measured using the equation:

$$A = \frac{Q\Omega\sigma Nt}{\cos\alpha_{in}} \qquad \ldots (1.26)$$

Where A is the area under peak, Ω is the detector solid angle in units steradians, sr [Bir89], Q is the number of charged particles and Nt is the number of nuclei per cm^2 [Tes95]. For targets that are not tilted, the denominator becomes 1, and then Equation (1.26) can sometimes be also written as follows:

$$Q_d = Q_{inc} \cdot \sigma \cdot \Omega \cdot Nt$$

where Q_d is the number of detected particles.

NRA measurement methods

NRA has 3 measurement methods these are, overall near surface contents, non-resonant depth profiling and resonant depth profiling [Tes95].

a. Overall near surface contents

The value of nuclei per cm^2 can be determined in thin layers independently of the concentration profile and of the other target's components provided the cross section of a given nucleus changes slowly with energy near the incident beam energy. The number of counts in the peak area, A from the thin layer can be calculated from Equation (1.26).

If $\sigma(E) \approx \sigma(E_0)$ for $E_0 > E > E - \Delta E$, where E_0 is the incident beam energy and ΔE is the energy lost.

If all the quantities in the above equation are known the absolute value of nuclei per cm^2 can be easy to calculate. Since A depends on the number of nuclei per cm^2 in different matrices, the measurements can be compared to a known standard by:

$$\frac{Nt}{Nt_{standard}} = \frac{A}{A_{standard}} \qquad \ldots (1.27)$$

Then the accuracy of the measurement is determined by measurement statistics and accuracy of a standard [Tes95].

b. Non resonant depth profiling

The peaks of resolution products become wider as the thickness of the sample is increased. The shape of peaks is the convolution of the concentration profile with the cross section and the depth resolution. Then the depth resolution, Δx can be calculated using:

$$\Delta x = \frac{\sqrt{\left[\Delta E^2_d + \Delta E_\gamma{}^2 + \Delta E_{ms}{}^2 + \Delta E_{abs}{}^2 + \left[\frac{\sigma^2_{out}}{\cos\alpha_{out}} + \left(\frac{dE_1}{dE_2}\right)^2\left(\frac{\sigma_{in}{}^2}{\cos\alpha_{in}}\right)\right]\right]}}{\left(\frac{S_{in}}{\cos\alpha_{in}} \times \frac{dE_1}{dE_2}\right) + \frac{S_{out}}{\cos\alpha_{out}}} \quad \ldots (1.28)$$

Where ΔE_d is the detector resolution, ΔE_γ is the geometrical energy spread, ΔE_{ms}, the energy from the multiple scattering, ΔE_{abs} is the absorber foil energy straggling, σ_{in} and σ_{out} are the Bohr straggling for the reaction product, and E_1 and E_2 are incident ion and reaction product energies in depth x [Tes95].

c. Resonant depth profiling.

The absorber foil reduces the depth resolution of the NRA, and this shows that resonances are so important for the resolution improvement. In this method, the depth scale can be given by:

$$x = \frac{E_0 - E_{resonance}}{\frac{S(E_{ave})}{\cos\alpha_{in}}} \quad \ldots (1.29)$$

Where $E_{resonance}$ is the resonance energy, E_{ave} is the average energy approximation given by: $E_{ave} = (E_0 - E_{resonance})/2$ and it can be used to calculate the energy loss integral, as the energy change is small. Then the depth resolution is given by:

$$\Delta x = \frac{\sqrt{\Gamma^2 + \frac{x}{\cos\alpha_{in}}\sigma_{st}^{\ 2} + \Delta E_{beam}^{\ 2}}}{\frac{S_{in}(E_{resonance})}{\cos\alpha_{in}}} \qquad \ldots (1.30)$$

Where Γ is the resonance width, σ_{st} is the incident particle Bohr straggling, ΔE is the incident beam energy spread. The above equation shows clearly that if the sample is tilted the better the resolution is, but as the beam penetrates deeper, the energy straggling increases so that the resolution becomes the same as of an un-tilted sample [Tes95].

Usage of standards

Since there is uncertainty in the calculation of the absolute overall surface content of an element it is advisable to use reference targets, these targets are called standards. The requirements for standards include

- High lateral uniformity over the beam.
- They should be amorphous to avoid channelling effects.
- They should have long-term stability in air, vacuum, and under ion bombardment.
- The target preparation should be highly reproducible.

There are some requirements for the measurement apparatus, which need to be met so that standards can be used and these are:

- Current measurements must be reproducible to avoid charge exchange after the beam analysis.
- Energy calibration must be reproducible and precise.
- The detection angle must be reproducible.
- Dead time and pile-up rejection should be accurate.

The measurements of unknown sample and a standard sample must be performed under the same conditions, for instance the solid angle, absorber, incident energy or the uncertainty of the current measurement. Then the number of the measured nuclei in the unknown sample can be given by:

$$Nt = Nt_{ref}\frac{A}{A_{ref}}\frac{Q^{ref}{}_c}{Q_c} \qquad \ldots. (1.31)$$

Where And A_{ref} are the peak areas in the spectra, Q_c and Q_c^{ref} are the total collected charges and Nt and Nt_{ref} are the number of nuclei per cm^2 for the unknown sample and the standard respectively.

In a situation where the standard and the unknown sample are both bulk, the composition at the surface is obtained by using a surface energy approximation to nuclear reaction analysis [Tes95]

Considering the binary-element unknown sample of composition A_xB_y, composed of A and B elements where x and y are the atomic fractions of A and B respectively. If the amount of element A in the unknown is to be measured, a standard containing element A is chosen. Suppose the standard is composed of element A and element C atoms of the composition A_zW_z. The surface heights of the element, A, in the two samples, in the unknown, $H_{A_0}{}^{U}$ and in the standard, $H_{A_0}{}^{K}$ is given by:

$$H_{A_0}{}^{U} = \frac{\sigma_A(E_0)\Omega_U Q_U \varepsilon_U x}{[\varepsilon]_{Anr}{}^{AB}\cos\alpha_{in}} \qquad \ldots (1.32)$$

$$H_{A_0}{}^{K} = \frac{\sigma_A(E_0)\Omega_K Q_K \varepsilon_K z}{[\varepsilon]_{Anr}{}^{AC}\cos\alpha_{in}} \qquad \ldots (1.32\ b)$$

Where $\sigma_A(E_0)$ is the nuclear reaction cross section for element A, $[\varepsilon]_{Anr}{}^{AB}$ and $[\varepsilon]_{Anr}{}^{AC}$ are nuclear reaction cross section factors for element A in the standard and the unknown respectively, Q, ε and Ω are total collected charge, energy per channel and solid angle respectively. Then making $\sigma_A(E_0)$ in (1.32b) the subject of the equation then substituting into (1.32) gives:

$$x = \frac{H_{A0}{}^{U}}{H_{A0}{}^{K}} \times \frac{[\varepsilon]_{Anr}{}^{AB}}{[\varepsilon]_{Anr}{}^{AC}} \frac{\Omega_K Q_K \varepsilon_K z}{\Omega_U Q_U \varepsilon_U} \qquad \ldots (1.33)$$

When both the standard and unknown measurements are in the same conditions the factor:

$$\frac{\Omega_K Q_K \varepsilon_K z}{\Omega_U Q_U \varepsilon_U} = 1 \ldots (1.34)$$ [Tes95].

1.3 Thesis outline

Chapter one has been introducing the technique to be used, NRA, reaction cross-sections and the way standards are used to reduce uncertainty in current measurements. The other more chapters are organized as follows:

- Literature review, which gives some works that have been previously done by some other authors using similar techniques which would somewhere somehow guide us is presented in chapter two.
- Research design and methodology, which is the way in which data is collected, analysed and presented is in chapter 3.
- Chapter 4 presents results and discussions.
- Then the last chapter is chapter 5 whereby conclusion and recommendations are drawn or presented from the preceding chapter.

Chapter 2

Literature Review

This chapter is about the previous works that have been done on ion beam analysis using techniques similar to the one used for the current work which is NRA, but due to the lack of works published under this IBA analytical technique this chapter is going to be looking at works done not necessarily at 150° or 135° (the angles of interest of this research) but within the required incident energy range 1.8 -2.8 MeV.

2.1 Nuclear reactions for the targets of ^{12}C, ^{13}C, ^{10}B and ^{11}B.

In most cases light elements depth profiling is performed using resonant nuclear reactions analysis (RNRA), which is most often induced by alpha, deuterons or proton particles, but one drawback of this is: it gives good depth resolution for one element at a time [Ter97].

Deuteron induced, proton-producing reactions, (d, p) are the ones that are often used to perform depth profiling of light elements in solids [Jul05]. Cross-sections of these deuteron-induced reactions are higher than those of ^{3}He induced reactions at the same energy. Even though ^{3}He particle induced reactions have lower cross sections but they are more sensitive to the linear surface. The more sensitivity of the ^{3}He particle induced reactions is due to the higher stopping power for ^{3}He than for deuterons at the same energy. It is therefore advisable to increase ^{3}He particles' incident energy when depth profiling nitrogen and some other light elements since cross sections for the reactions induced by 2.4 MeV ^{3}He particles on nitrogen are too low [Ter97]

Carbon analysis

Carbon depth profiling and quantitative analysis are normally performed using non-resonant nuclear reaction analysis induced by deuterons. Sometimes the ^{3}He induced reactions alternatively used to depth profile carbon in the first few microns below the surface; this is due to their more sensitivity to the near surface and the less they produce compared to the deuteron induced reactions [Ter97].

In a depth profiling work performed by Julien and Terwagne the $^{12}C(d, p_0)^{13}C$ and $^{13}C(d, p_0)^{14}C$ reactions with protons emitted at very different energies were used to depth profiling both ^{12}C and ^{13}C simultaneously. In this depth profiling performance it was observed that the $^{12}C(d, p_0)^{13}C$ reactions' cross-section was 10 times less than for $^{13}C(d, p_0)^{14}C$, this showed the importance of well chosen detection geometry in order to depth profile ^{12}C and ^{13}C with a high sensitivity and good resolution [Jul05].

The geometry that was chosen for the above depth profiling work is: two silicon surface detectors with one positioned at NRA position, 135° the other at RBS position, 165° relative to the incident beam induced by 1.05 MeV deuterons. The NRA detector measured protons and the RBS detecting backscattered deuterons. It was concluded that for oxygen to be precisely measured, the cross-section of ^{13}C $(d,\alpha_0)^{11}B$ nuclear reaction must be measured for incident particles of energy less than 1 MeV [Jul05].

The nuclear reaction $^{12}C(d, p_0)^{13}C$ shows to be one of the very important reactions for low concentration determination and depth profiling of Carbon in heavy matrices if there are some other light elements or not. In another study Kokkoris et al. measured the differential cross sections of the above reaction at incident energies between 900 – 2000 keV in steps of 25 keV at a scattering angle range of 135° – 170° in steps of 5°, the target used in this work was a self supported natural Carbon foil of 99.9% purity and 1×10^{18} atom/cm^2 thickness. The results of this work were compared to the relevant data that had already existed in literature and they showed to be in good agreement [Kok06]. The results were then presented in plots of cross sections vs. incident particles energies, figure 2.1 shows a plot of nuclear reaction cross section vs.

incident beam energy at a scattering angle of 150° Kok06].

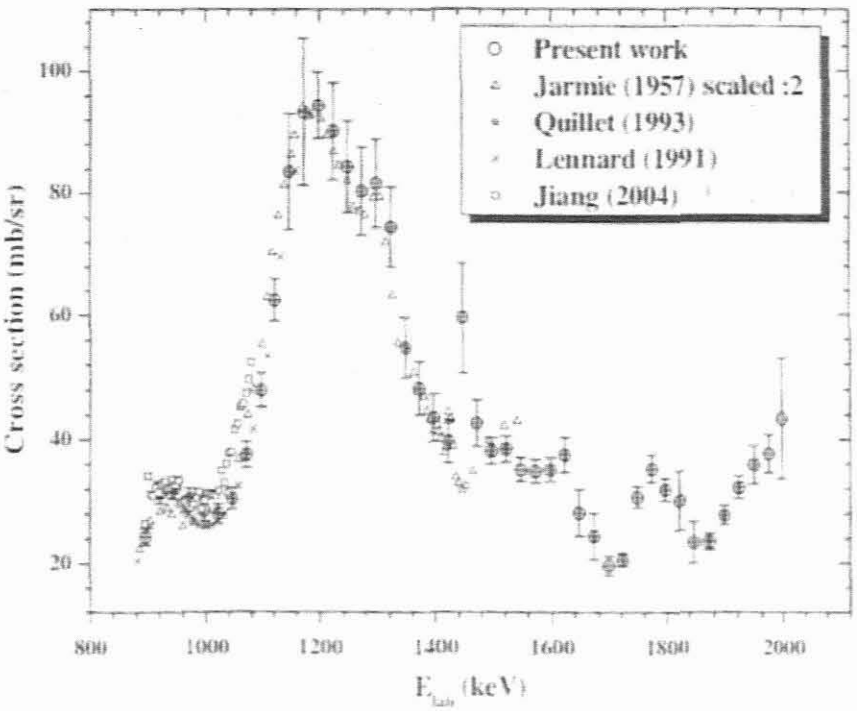

Figure 2.1: A graph of cross section vs. incident beam energy for ^{12}C (d, p_0) ^{13}C [Kok06].

In another experiment Terwagne et al. measured the cross-section of $^{12}C(^3He, p_i)^{14}N$ reaction (for i = 0, 1, 2, 3, 4) at an angle of 90° for incident energies between 1.6 –3.0 MeV. Also the cross-sections of the $^{12}C(^3He, p_i)^{14}N$ reaction (for i = 1, 2), the $^{12}C(^3He, \alpha_0)^{11}C$ reaction and the elastic $^{12}C(^3He, ^3He)^{12}C$ were also measured at an RBS angle of 177.2° in the incident energy range of 1.96 – 2.93 MeV. The conclusion to this work was: detecting backscattered particles simultaneously with protons at 90° makes it possible to profile heavy elements like titanium in addition to light elements [Ter97]. The results were then presented in plots of cross sections vs. incident particles energies. Figure 2.2 shows a plot obtained by Terwagne et al. in a reaction where the first proton was scattered.

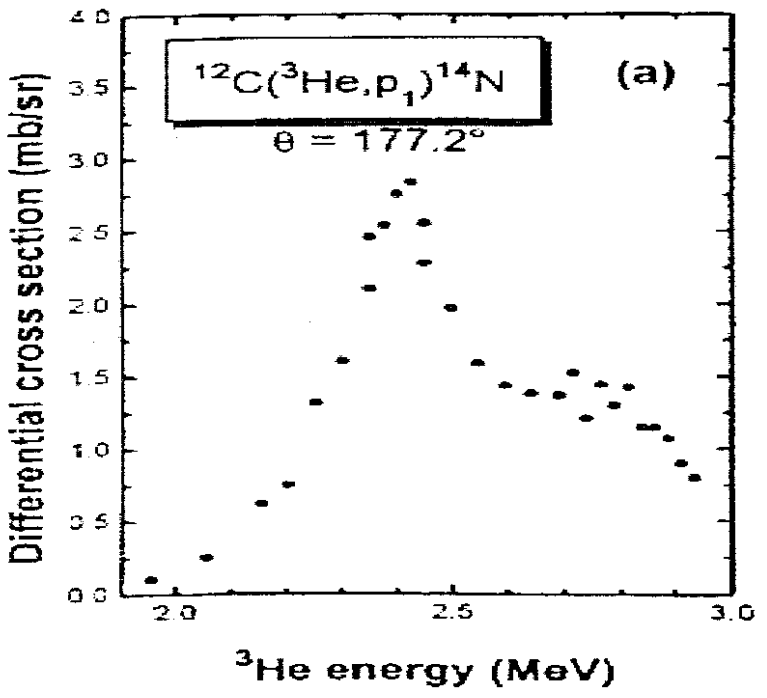

Figure 2.2: A graph differential cross section vs. incident beam energy for ^{12}C (^3He, p_1) ^{14}N [Ter97]

Boron Analysis.

It has been many years since the study of boron depth profiling by $^{11}B(p, \alpha)^8Be$ in semiconductors begun. During this study a number of approaches based on the above reaction have been discovered. These are: profiling by spectrum fitting at broad resonance at 660 keV, energy analysis at 262 MeV and by low energy resonance at 160keV [Jia02].

NRA has shown to be more useful if the $^{11}B(p, \alpha_0)^8Be$ nuclear reaction is used by offering the advantage of an isolated α peak above the energy of the incident protons and a higher cross-section. In addition even though the depth resolution is very limited, some information about the distribution can be obtained [May98].

The reaction induced by protons on a ^{11}B target has four exit channels.

(I) $^{11}B + p \longrightarrow {}^{12}C^{*} \longrightarrow \alpha_0 + {}^{8}Be^{*} \longrightarrow \alpha_0 + \alpha_{01} + \alpha_{02}$

(II) $^{11}B + p \longrightarrow {}^{12}C^{*} \longrightarrow \alpha_1 + {}^{8}Be^{*} \longrightarrow \alpha_1 + \alpha_{11} + \alpha_{12}$

(III) $^{11}B + p \longrightarrow {}^{12}C^{*} \longrightarrow \alpha_2 + \alpha_3 + \alpha_4$

(IV) $^{11}B + p \longrightarrow {}^{12}C^{*} \longrightarrow {}^{12}C + \gamma$

In channels (I) and (II) the $^{8}Be^{*}$ nucleus splits into two alpha particles α_{01} and α_{01}, and α_{11} and α_{12} with energy released being 8.583 MeV. $^{8}Be^{*}$ nucleus is in the first excited state in channel (II) thus when it splits into 2 alpha particles α_{11} and α_{12} it releases a 5.683 MeV energy. With channel (IV) having a total cross section of 10μb in the energy range 2.0 – 2.7 MeV [May98].

Mayer et al measured a cross section of $^{11}B(p, \alpha)^{8}Be$ and $^{11}B(p, p)^{11}B$ nuclear reaction at a scattering angle of 165° with incident beam at 1.7 – 2.7 MeV energy with an absolute accuracy of 7%, then derived cross section values using the simultaneously measured RBS spectra of protons backscattered from a thin gold layer. Then it was concluded that the values obtained by different methods agreed at the same energy within about 10% [May98].

McIntyre et al. used the reaction $^{10}B(\alpha, p)^{13}C$ and $^{11}B(\alpha, p)^{14}C$ reactions to quantify the boron content of multiplayer thin film used in X-ray optics applications. In addition to this measured relative proton yield from the $^{10}B(\alpha, p)^{13}C$ and $^{11}B(\alpha, p)^{14}C$ reactions at incident energies between 1.4 and 3.3 MeV at an angle of 135°. A comparison was made between ^{4}He backscattering and the B (α, p) C reactions in determining the boron content of thin films, particularly Pd/B [McI92].

In the above-mentioned experiment a 5.5 MeV Van de Graaff accelerator was used to obtain $^{4}He^{-}$ ions. A large area surface barrier detector was added to a standard backscattering set up to detect production particles, protons from the (α, p) reaction, it was placed 40 mm from the target with a 0.3 sr solid angle. The Mylar foil was used to stop backscattered alpha particles. Then a multi-channel analyzer and standard nuclear electronics were used to obtain proton spectra [McI92].

In conclusion B(α, p)C reaction method was found to be simpler for determining boron content of thin films than the ^{4}He backscattering method, it was found simpler for both ^{10}B and ^{11}B isotopes near 3.0 MeV incident energy. It was also found that using the above method could result in simultaneous determination of the boron area density from the observation of protons and the determination of the Pd or Ag area density from observation of backscattered $^{4}He^{+}$ particles [McI92].

Purser and Widenthal [Pur63] measured the angular distributions and differential cross sections of the α particle groups leading to the ground and first excited states of ^{8}Be over the deuteron energy range of 1.0 –1.8 MeV. The α particles were observed from the reaction $^{10}B(d, \alpha)^{8}Be$ with solid state particle detectors and a 256-channel analyzer. The differential cross sections were measured at 156° in the laboratory system. For the reaction channel leading to the ground state of ^{8}Be, the differential cross section showed a steady increase from approximately 0.28 to .3 mb/sr in the energy range 1.0-1.8 MeV.

The differential cross sections for the reaction channel leading to the 2.94 MeV, first excited state of ^{8}Be showed an increase from 2.63 mb/sr to a maximum of 5.54 mb/sr at 1.6 MeV and then decreased to 4.88 mb/sr over the same energy range. Angular distributions of the α particles leading to the ground and first excited states of ^{8}Be were measured at five energies within 1.0 –1.8 MeV. Forward peaking was observed with an energy dependant second maximum at approximately 115°. The table below shows the values of cross sections obtained in the deuteron energy range of 1.0 – 1.8 MeV [Pur63].

Ed (MeV)	σ (mb)
1.0	7.5
1.2	7.2
1.46	6.75
1.59	9.2
1.75	9.3

Table 2.1: A table of cross sections calculated by Purser et al. at certain incident energy values ranging between 1.0 to 1.75 MeV [Pur63].

The results of this research seemed to indicate that, in the energy range studied, the interaction radius of two α particles is comparatively large [Pur63].

In another research Jiarui and Chu analyzed boron by measuring accurately the cross sections of the nuclear reaction $^{11}B(p, \alpha)^{8}Be$ using three different improvements, self supported ^{11}B foil target, high resolution detection and careful analysis of spectra [Jia02].

For the self supported thin ^{11}B target improvement a self supported ^{11}B thin foil target of 50 nm thicknesses, up to 99% ^{11}B purity was used. This was done to eliminate interference of the (p, α) spectrum by backscattering protons to get a clean RBS spectrum with a well separated RBS peak for ^{11}B by α-beam [Jia02].

In a high-resolution detector without front absorber improvement, a silicon surface barrier detector was placed 70 mm away from the target center, the detector's energy resolution was 14 keV. The detector without an absorber was to make sure that α peaks are clean and separated in both (p,α) reaction and RBS measurement [Jia02].

In conclusion the real cross section of the $^{11}B(p,\alpha)^{8}Be$ was obtained for the first time in the incident energy range of 0.4 – 1.6 MeV, the experimental error to this was 3.3%. The cross sections under convention with correctly defined lower discrimination level obtained could be used for applications in ^{11}B analysis [Jia02].

2. 2. Overview

The previously mentioned works emerged with the study undertaken for this research since the targets used are the same as the ones that will be used in this research, although the angles of scattering are different from the one required here which are 135° and 150°. The above-mentioned work's incident energy is within the required range, which is 1.8 - 2.8 MeV. The type of detectors and facility that are

going to be used are the same as the ones used in the above-mentioned work, but in the current work we will use two detectors and a Van de Graff accelerator. All in all the previous works mentioned in this chapter help us to know what to expect from the current study.

In summarizing this chapter a table containing nuclear reaction data of the current research's ions on targets of boron, carbon, silicon and oxygen is presented in Table 2.2.

Target	Reaction	Angle	Q_{value} (MeV)	σ_{max} (mb/sr)	$E_{\sigma max}$ (MeV)	Energy Range (keV)	Useful?
^{10}B	$(p, p_0)^{10}B$	154°	0.000	1.3	2.98	1000-3530	Yes
	$(p, \alpha_0)^{7}Be$	90°	1.147	1.9	2.25	1300-2580	Yes
	$(p, \alpha_1)^{7}Be$	90°	0.717	4.9	4.21	2660-7110	No
	$(d, \alpha_0)^{7}Be$	156°	17.818	0.43	1.62	980-1800	Yes
	$(d, \alpha_1)^{7}Be$	156°	14.918	5.8	1.62	980-1800	Yes
	$(^3He,p_0)^{12}C$	135°	19.694	0.91	3.30	1970-3980	Yes
	$(^3He,p_1)^{12}C$	135°	15.261	0.91	3.30	1970-3980	Yes
	$(\alpha, \alpha_0)^{10}B$	170°	0.000	1.78	2.38	980-3980	Yes
	$(\alpha, p_0)^{13}C$	135°	4.064	6.3	4.60	4000-5010	No
	$(\alpha, p_1)^{13}C$	135°	0.979	0.675	4.56	4000-5010	No
^{11}B	$(p, \alpha_0)^{8}Be$	154°	8.586	4.4	2.50	310-4940	Yes
		165°	8.583	6.8	2.6	1690-2690	Yes
	$(^3He,p_0)^{13}C$	135°	13.185	0.26	4.2	1970-3980	No
	$(\alpha, p_0)^{14}C$	135°	0.784	3.9	4.78	4000-5010	No
^{12}C	$(p, p_0)^{12}C$	150°	0.000	5.75	1.738	1000-3500	Yes
	$(d, p_0)^{13}C$	135°	2.722	9.1	1.28	900-2000	Yes
		140°	2.722	9.5	1.28	900-2000	Yes
	$(d, p_1)^{13}C$	145°	-0.3677	3.18	1.45	900-2000	Yes
		150°	-0.3677	3.3	1.45	900-2000	Yes
		170°	-0.3677	3.62	1.45	900-2000	Yes
	$(^3He,^3He)^{12}C$	177.2°	0.000	3.335	2.02	1960-2940	Yes
	$(^3He,p_1)^{14}N$	159.4°	2.467	5.0	2.9	1770-5390	Yes
	$(^3He,p_2)^{14}N$	159.4°	0.834	9.8	4.4	1960-2940	No
		177.2°	0.831	0.27	2.35	1780-5390	Yes
	$(\alpha, \alpha_0)^{12}C$	170.5°	0.000	1.3	4.25	1560-4980	No
^{13}C	$(p, p_0)^{13}C$	163.8°	0.000	9.5	4.0	2610-4990	No
	$(d, p_0)^{14}C$	135°	5.947	3.85	1.4	500-1650	Yes
	$(d, p_0)^{14}C$	150°	5.952	4.4	1.325	500-1650	Yes
	$(^3He, p_0)^{15}N$	150°	10.666	1.08	3.15	1900-3530	Yes
	$(\alpha, \alpha_0)^{13}C$	165°	0.000	8.4	2.78	1980-3530	Yes

Table 2.2: Useful existing nuclear reactions data for the undertaking of study. $E_{\sigma max}$ in the table is the energy at which the maximum cross section is found, the column labeled "useful?" refers to whether the reaction's incident energy is within the study's required range 0.8 - 3.0 MeV [www09].

Target	Reaction	Angle	Q_{value} (MeV)	σ_{max} (mb/sr)	$E_{\sigma max}$ (MeV)	Energy Range (keV)	Useful?
^{16}O	(d, α_0)^{14}N	135°	3.11	1.28	1.0	820-2020	Yes
		142.2°	3.11	1.21	1.0	790-1680	Yes
		150°	3.11	1.0	1.0	700-1060	Yes
	(d, p_0)^{17}O	135°	1.919	2.3	2.65	700-1800	Yes
		142.2°	1.919	1.2	1.68	790-1700	Yes
		150°	1.919	1.90	1.68	700-1800	Yes
	(d, p_1)^{17}O	135°	1.048	3.4	2.1	510-2970	Yes
		142.2°	1.046	1.36	1.38	790-1700	Yes
		145°	1.047	0.95	0.96	760-950	Yes
		150°	1.046	1.046	1.33	700-1800	Yes
	(^{3}He, α_0)^{15}O	90°	4.914	3.4	2.4	1590-2590	Yes
	(α, α_0)^{16}O	150°	0.000	8.7	3.03	2950-3050	Yes
	(p, p_0)^{16}O	149.5°	0.000	6.2	2.77	248-2810	Yes
^{18}O	(p, α_0)^{15}N	144°	3.980	1.0	1.765	1730-1770	Yes
		155°	3.980	1.45	1.761	169-1770	Yes
		165°	3.980	8.0	1.780	920-2060	Yes
	(d, α_0)^{16}N	165°	4.247	2.2	1.920	830-2000	Yes
	(d, α_1)^{16}N	165°	4.117	2.45	1.75	820-1990	Yes
	(d, α_2)^{16}N	165°	3.942	1.15	1.68	840-2010	Yes
	(d, α_3)^{16}N	165°	3.845	0.72	1.76	840-2000	Yes
^{28}Si	(d, p_0)^{29}Si	150°	6.249	1.28	1.93	1040-2100	Yes
	(d, p_1)^{29}Si	150°	4.972	2.48	1.15	1040-2100	Yes
$^{Natural}Si$	(p,p_0)$^{Natural}Si$	160°	0.000	2.175	1.69	1530-2130	Yes
	(α,α_0)$^{natural}Si$	150°	0.000	1.29	3.89	2490-4920	No

Table 2.3: Nuclear reactions data for oxygen and silicon within the study's required range of 0.8 - 3.0 MeV [www09].

To reduce uncertainties in our measurements we will compare them with data taken from the literature and standards of ^{16}O measurements, which are the standards for which we are having enough data in our nuclear data library especially at the angles 150° and 135°.

Chapter 3

Research design and Methodology

In the current research we are dealing with light nuclides so we opted to use NRA, an IBA method, this was due to NRA's high sensitivity and its ability to depth profile nondestructively [Bir89]. When performing IBA there are three important processes: beam production, transportation and products detection [Tes95]. Its facilities comprise a Van de Graaff accelerator, ion source, ion beams, target chamber or scattering chamber, targets, solid state detectors, preamplifiers, linear amplifiers, standard nuclear electronics and multi-channel analyzers, figure 3.1 shows a schematic diagram of the arrangement of facilities for scattering experiments. Chapter 3 is going to be about description of facilities and the experimental procedure then overview.

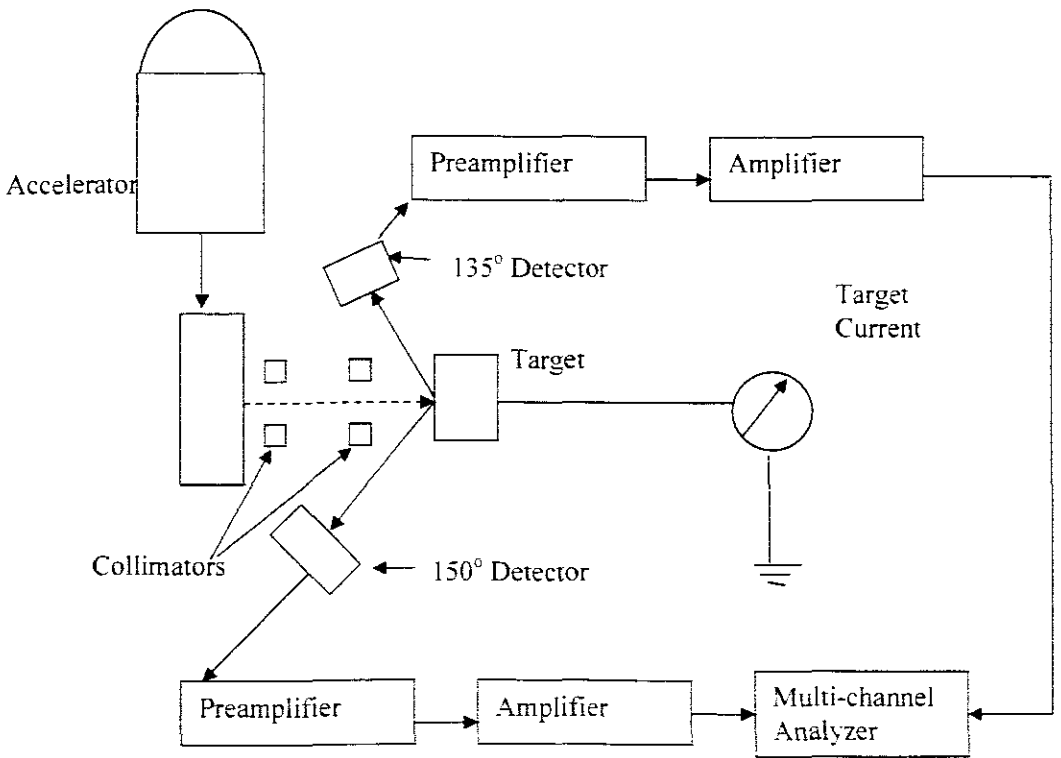

Figure 3.1: A schematic diagram of showing a setup and facilities used for ion beam analysis [Chu78].

3.1 Description of facilities

a. Ion sources

The name, ion source indicates clearly that ion sources were basically designed for the production of ions and they are located inside accelerators. Ion sources' principles of operation are based on stripping off of electrons from gas atoms thus giving the gas atoms charge states [Bir89], this is normally done by electron bombardment of the gas enclosed in the chamber. Ion sources are grouped into those suitable for high energy ion production and those suitable for low energy ion production [Bir89]. So in the present work we will use high-energy positive ion production ion sources. Under this group we find radio frequency (RF) and duoplasmatron ion sources. RF is used for RBS and PIXE[3] analysis whereas duoplasmatron is used for NRA [Bir89].

Duoplasmatrons can give beams currents up to a few mA which is quite high compared to any other high energy positive ion sources, as it has been mentioned above that ion sources give charge states to gases, thus the beam coming out of the duoplasmatron usually contains positive beams, but sometimes it also contains a mixture of various atomic species and charge states [Bir89].

b. Van De Graaff Accelerator

Before the invention of particle accelerators the only sources of particles that could induce nuclear reactions were natural alpha particle emitters. These natural alpha emitters were used until 1932, the year in which particle accelerators were first constructed. Nowadays the use of these sources is no longer important due to the fact that the accelerators are capable of accelerating particles up to the required energies [www06]. These devices use electric and magnetic fields to propel charged particles to higher energies, since their purpose is to generate high-energy particles for interaction with matter. Accelerators are categorized into circular and linear accelerators. Circular ones are the ones that can accelerate particles along circular paths in machines of different sizes e.g. synchrotrons and linear ones are the ones that

use linear array of plates with alternating high-energy field, they are more often used to accelerate particles traveling in short lines, although they can sometimes be used to accelerate particles traveling over very long distances [www07].

Van de Graaff accelerator is made of three important parts, these are: the pressure tank, the generator, and the accelerator proper. The principle of operation of the Van de Graaff accelerator: a conveyor belt is used to collect positive charges from a high voltage source at the end of the belt and transport the charges to the outside of the terminal at another end of the belt situated at the top of the accelerator. Nowadays' Van de Graaff accelerators can be operated at voltages up to 20 MV, but the one we will use for this research located within South African Nuclear Energy Corporation lab can be operated up to a voltage of 3.8 MV. The Van de Graaff accelerator at NECSA is shown in figure 3.1.

Figure 3.1: The tank of the van de Graaff accelerator used at NECSA.

c. Target chambers.

This device is basically used to hold targets and detectors, it is also used for radiation shielding especially for NRA when scattering experiments a run [Bir89]. It is sometimes called scattering chamber or vacuum chamber due to the fact that vacuum is maintained when scattering experiments are performed. Vacuum is maintained otherwise the beam would rapidly loose energy in air. Pumping systems are used to remove any gases evolved from the target and chamber [Bir89].

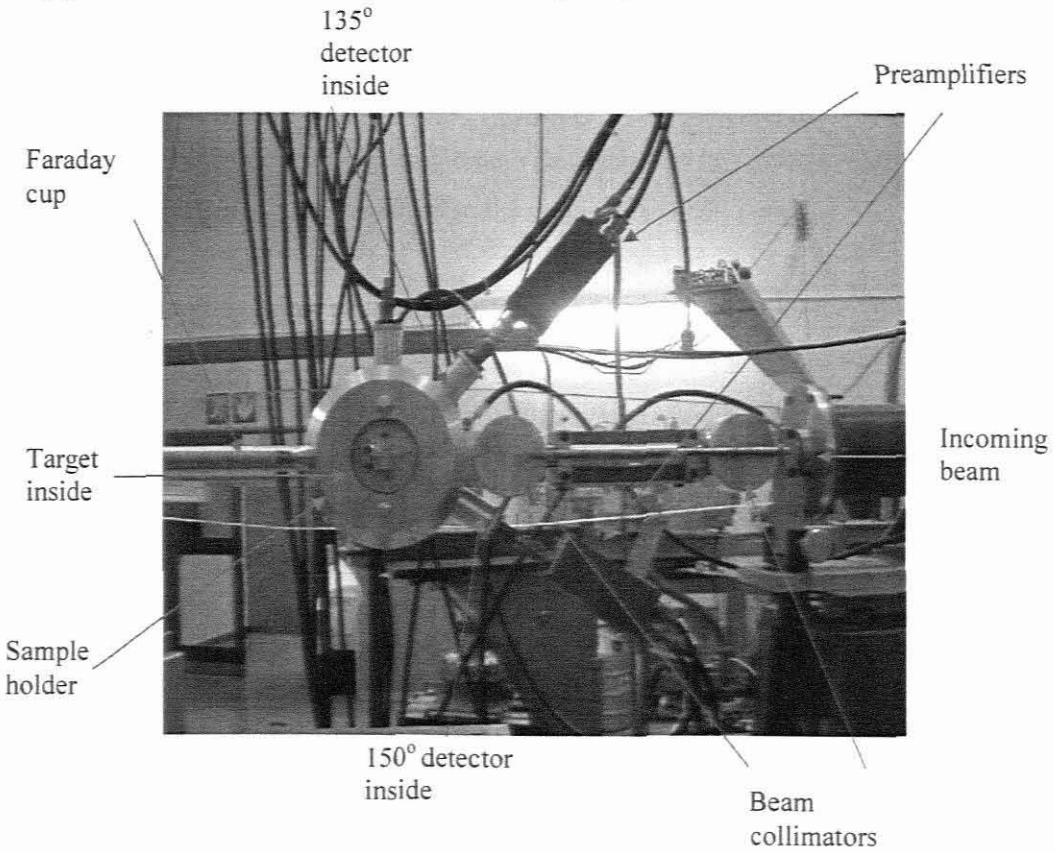

Figure 3.2: A picture of the target chamber.

d. Silicon surface barrier detectors

These are the most used particle detectors for ion beam analysis; they are used especially for light ion detection, mainly proton and alpha particle detection. Semiconductor detectors' principle of operation is like the one of a semiconductor diode: a semiconductor does not conduct electricity if reverse biased; this is due to enlarged depletion layer, the layer where charge carriers have been depleted. But if charge carriers (electron-holes) are formed in the depletion region and the temperature of the diode is raised, the electrons and holes are moved to the opposite directions by the reverse-biasing electric field. The leakage current is temperature dependant current is produced. The generation of electron hole pairs can also be caused by light by promoting electrons from the valence band to the conduction band [Tes95].

In semiconductor detectors: energetic ions start loosing energy as they enter the depletion region of the detector, this is due to its collisions with the electrons of the detector's constituent atoms or nuclei. Photons are formed during these collisions. This process is called electronic stopping. During this process charge carriers (electron-hole) pairs are produced at a rate of a few eV per pair. If the detector is thick enough ions come to rest in a period of only a few picoseconds leaving a number of electron-hole pairs behind. The swept electron-hole pairs appear as a current pulse of a few ns at the detector terminal, which is collected by a charge-sensitive preamplifier [Tes95].

In Silicon surface barrier detectors the quantity of collected charge is linear in the total energy lost by protons and alphas due to electronic stopping processes. But this quantity is non linear for all ions' energy lost due to nuclear stopping processes and charge recombination the quantity is then called pulse height defect. The preceding phenomena can make the detector's energy resolution worse, which is typically in the range of 15 -20 keV for light ions. Some of ions' energy gets lost as they penetrate the gold entrance window of the detector. Heavy ions have a large pulse height defect, and they can cause irreversible radiation damage to the detector thus their detection must be done with caution. In order to assure required detector depletion thickness to

stop the corresponding highest energy particle a nonogram provided by the supplier is used [Tes95]. There are some precautions with which surface barrier detectors should be operated, these are: surface barrier detectors should be kept dark since they are very sensitive to light, they should not be operated in atmospheric conditions unless they are ruggedised and their electrodes should not be touched [Bir89].

For the present study an EG&G ORTEC model 1759I silicon surface barrier detector of 100% efficiency and mounted such that it subtends a solid angle, $d\Omega$ of 2.03 msr, which then gave a scattering angle accuracy of $\pm$ 0.5° placed at an angle of 150°. While another EG&G 20-492I model surface barrier detector of the same efficiency was placed at 135°, subtending a 1.97 msr solid angle.

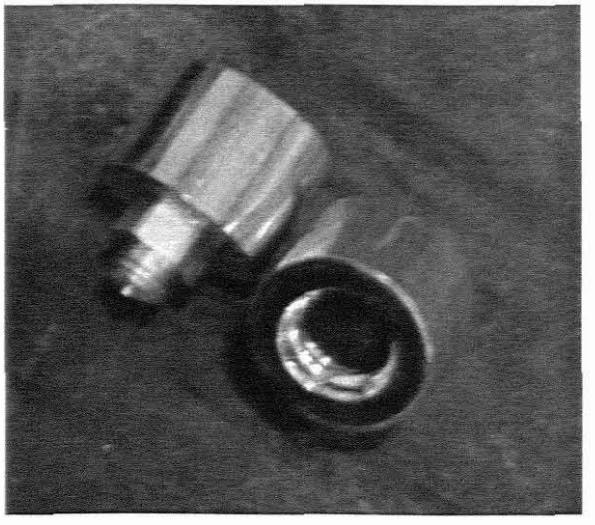

Figure 3.3: A picture showing surface barrier detectors used for the current study

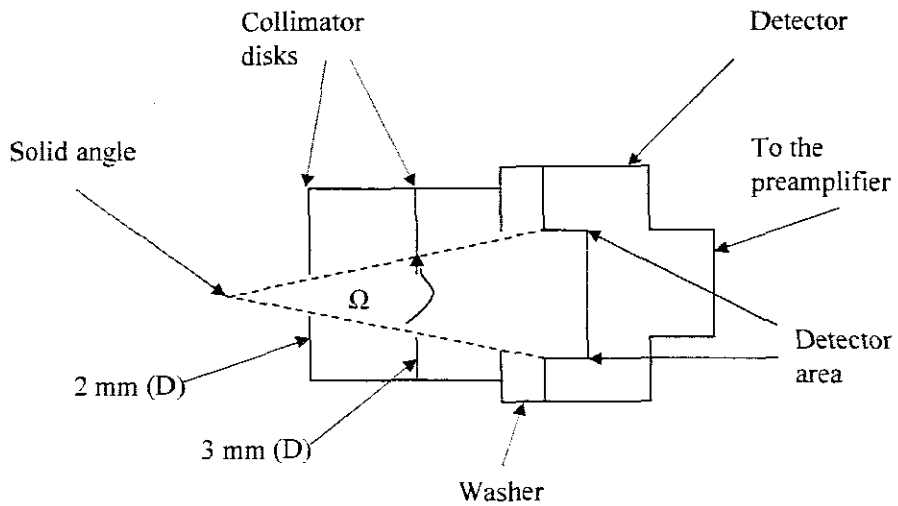

Figure 3.4: A schematic diagram showing how the detector solid angle was attained for current study.

e. Preamplifiers.

Signals collected from the detector are usually so small that they become very difficult to deal with if no immediate amplification has been done, and then in situations like these preamplifiers come into play. Preamplifiers are connected near to the detector outputs with their outputs connected to the other signal processing and analyzing electronics. These devices need to be connected as close as possible to the detector to reduce capacitive loading due to the fact the signal to noise ratio increases with increasing input capacity [Kno79].

These devices are divided into voltage sensitive and charge sensitive types, with the voltage sensitive type being the ones having a configuration providing output pulses with amplitude proportional to the one of the voltage pulse supplied to its input terminals. Charge sensitive preamplifiers are the ones having a configuration output pulses proportional to the total integrated charge in the pulse provided to the input terminals, if the duration of the input pulse is still shorter than the time constant. RC [Kno79].

Charge sensitive preamplifiers are normally used with semiconductor diode detectors i.e. silicon surface barrier, since it is the charge collected that the energy of the detected particle is proportional to [Kno79]. The model used for the detector at an angle of 150° in the current study was EG&G ORTEC 142B, and an EG&G ORTEC 142A for the detector at 135°.

f. Linear Amplifiers.

Linear amplifiers provide two functions, which are: amplitude gain and pulse shaping. They produce linear pulses from pulses of either polarity accepted as inputs. The amplitude gain has two controls: coarse and fine controls through which it is adjustable over a wide range [Kno79].

The gain depends on the application; for instance if the maximum design output amplitude is exceeded by the gain, the amplifier saturates then produces distorted pulses with a flat top at the saturation amplitude. This means linear amplifications is only realized for pulses short of saturation level [Kno79]. The linear amplifier model used for the present study was EG&G ORTEC 577 and an EG&G ORTEC 485.

g. Multi-channel analyzers.

This device is an analog to digital converter that converts a properly adjusted spectroscopy amplifier's output. The heart of the device is the analog to digital converter (ADC). It (ADC) analyzes the maximum amplitude of pulses with a conversion gain ranging from one part in 256 up to one in 8192. The input pulses are used to charge a capacitor until the peak of the pulse is detected. When charging stops a constant current source is turned on and begins to discharge the capacitor linearly. Then when discharging begins a high frequency clock also starts ticking and its ticks are counted until the capacitor is fully discharged. When the capacitor is fully discharged the clock stops counting and the counts are presented as digitized pulses. Figure 1.3 shows a schematic diagram of a multi-channel analyzer [Tes95].

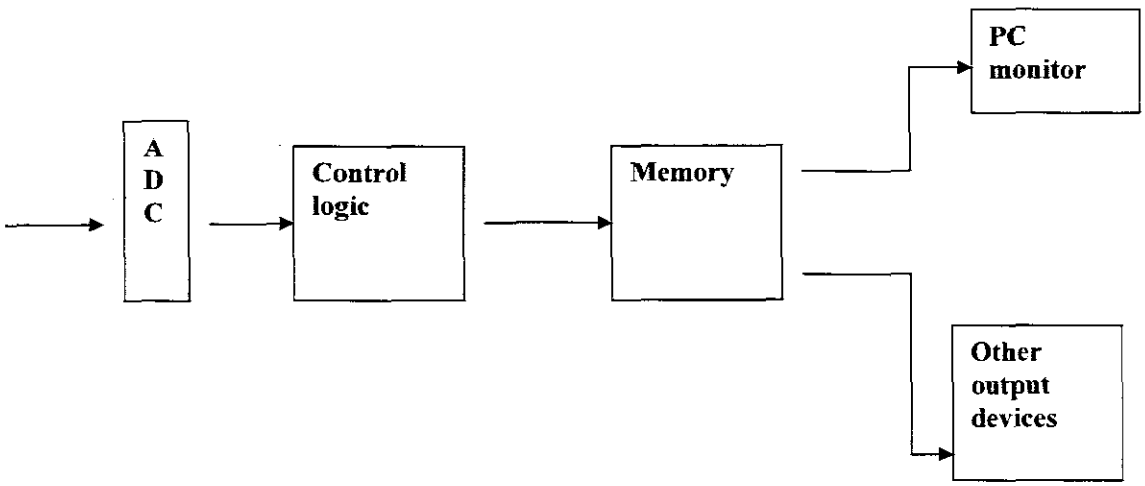

Figure 3.5: A schematic diagram of a multi-channel analyzer [Kno79].

3.2 Experimental procedure

3.2.1 Sample design.

Three targets were used for the current study, which are thin carbon foil of a 20 *ug* cm^{-2} thickness, boric acid (HBO_3) crystal and a foam boron carbide target, while beam particles were interchanged between deuterons and ^3He particles. The foam boron carbide target was composed of SiO_2 and B_4C with the chemical formula $(B_4C)_x$ / $(SiO_2)_y$ with x and y being the composition percentage of B_4C and SiO_2 respectively, with x between 0.3 and 0.5% and y between 0.7 and 0.3%.

3.2.2 Data acquisition and analysis

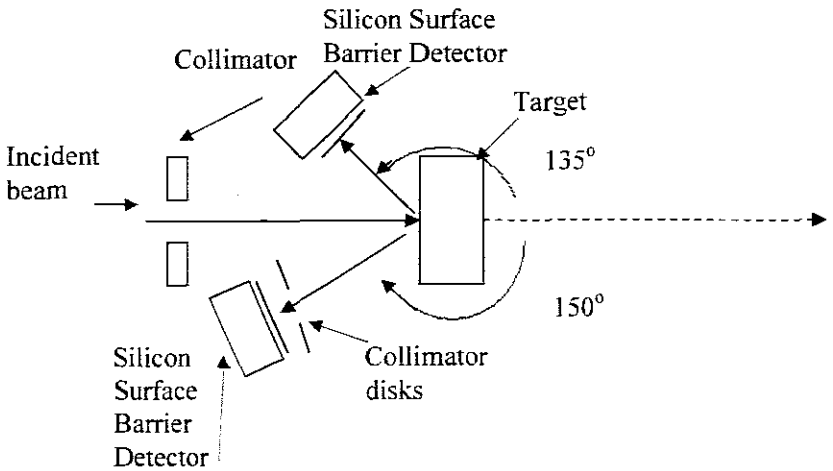

Figure 3.6: An experimental setup that was used for the research.

The set up used for data collection was as shown in Figure 3.6 targets were put inside the target chamber then the pressure inside the chamber was maintained at 10^{-4} torr, while beams of deuterons. ^{3}He and alpha particles were accelerated to energies between 0.8 and 3.0 MeV toward it. Collimators were used to sharpen and steer the beam making sure that it hits the target on the right sport. Two silicon surface barrier detectors were used with another one placed at a scattering angle of 150° and a distance of 8.5 cm from the target subtending a solid angle of 2.03 msr while the other was placed at a scattering angle of 135° at the same 8.5 cm distance from the target subtending a 1.97 msr solid angle. The aim of the 135° detector was for data normalization, since there is more data available for the reactions at this angle in our nuclear data library. To make sure that the detector is able to detect every particle falling within the solid angle, two collimators (2 and 3mm) were used in a conical arrangement to guide scattered particles into the detector sensitive area. No filtering material was put in front of the detectors; this was done to enable the technique to be RBS/NRA.

3.2.3 Measuring of cross sections

Cross sections were calculated using the equation (from equation 1.26):

$$A = \frac{Q\Omega\sigma Nt}{\cos\alpha_{in}},$$

where A is the area under spectrum peak, Q is the number of incident particles, Nt is the atomic density of the target, α_{in} is the angle between the incident beam direction and the sample normal. Since in the case of the current study α_{in} is 0° then the above equation becomes:

$$Q_d = Q\Omega\sigma Nt$$

In taking our measurements, we collected Q from the Faraday cup using a current integrator, while Q_d the number of detected particles or detected charge was taken from spectra, in counts.

According to the above Equation or Equation (1.26), the normalized charge, $\frac{Q_d}{Q}$ is directly proportional to the cross section, σ. Then we could use the relation to compare the normalized charge, which we preferred to call the normalized number of counts, N_c to the cross sections taken from literature. The reason behind this is: in Equation (1.26) the two parameters, solid angle, Ω and the target's atomic density, Nt are constants. Using the above argument we then plotted graphs of normalized number of counts and cross sections vs. incident beam energy on the same set of axis, which were then compared.

3.3 Overview

This chapter was seeking to give clue of what is going to be useful for this study; those are facilities and the way they function and how the problem gets sorted out. Then the next chapter gives details on the data and the results taken from the data collected.

Chapter 4

Results: Presentation and discussions

This chapter presents sample description and characterization, describes and summarizes the main results, which are discussions of the main trends, patterns and connections that have emerged then followed by tables and plots.

4.1 Sample description and characterization

According to NRA theory the layer consisting of nuclei of interest should be sufficiently thin in order for ions energy loss effects to be negligible, this is due to the fact that thicker targets deteriorate energy resolution. While on the other hand thicker layers help with production of good spectra [Jia04].

The thin carbon foil was 50 $ug.cm^{-2}$ in thickness and consists of ^{12}C and ^{13}C isotopes. Where as the Boric acid crystal was about $1mm$ in thickness and consist of ^{1}H, ^{10}B, ^{11}B, ^{16}O, and ^{18}O isotopes.

A thick boron carbide target containing SiO_2 with the chemical formula $(B_4C)_x$ / $(SiO_2)_y$ and the ratio x:y is 30% to 70% was used to measure cross sections of boron and carbon, the reason behind using this target since it consisted of both boron and carbon natural elements. These two natural elements have these isotopic compositions ^{10}B, 19.61% and ^{11}B 80.39% and ^{12}C 98.07% and ^{13}C 1.07% respectively. Boron carbide target makes it easier to get cross sections of the reactions of isotopes of boron and carbon such as ^{10}B, ^{11}B, ^{12}C and ^{13}C using nuclear reaction analysis. This is motivated by the ability of NRA of analyzing multiple elements at the same time [Jia04] and the feature that NRA is isotope specific.

The target, B_4C target enables one to measure reaction cross-sections of the following nuclear reactions: $^{12}C(d, p_0)^{13}C$, $^{12}C(d, p_1)^{13}C$, ^{12}C (d, d)^{12}C, $^{12}C(^3He, p_0)^{14}N$, $^{12}C(^3He,$

$p_1)^{14}N$, $^{12}C(^3He, p_2)^{14}N$, $^{12}C(^3He, ^3He)^{13}C$, $^{13}C(d, p)^{14}C$, $^{10}B(d, \alpha_0)^8Be$, ^{10}B $(d, \alpha_1)^8Be$, $^{11}B(d, p_0)^{12}B$, $^{11}B(d, p_1)^{12}B$ and $^{10}B(^3He, p)^{12}C$.

During the data acquisition, the intensity was kept at 20 *nA* for the deuterium (D^+) beam and at 2 nA for helium-3 ($^3He^+$) beam. The acquisition times ran from 3000 to 7000s, this was due to the target number of counts to be achieved as taken from the current from the current integrator, which was 1×10^6 counts. Thus from this information, the particle flux for deuterium beam could be calculated to run from $1.78\times10^{10}\ particles/s$ to $4.16\times10^{10}\ particles/s$. For the helium-3 beam particle flux could run from $1.78\times10^{9}\ particles/s$ to $4.16\times10^{9}\ particles/s$.

4.2 Main Results

Spectra peaks identification

The peaks on spectra were identified through standard kinematics calculations for the reaction particles, which were calculated theoretically using equation (1.20).

$$E_3 = \left[\frac{\sqrt{m_1 m_3 E_1}\cos\theta}{(m_3+m_4)} \pm \frac{\sqrt{m_1 m_3 E_1 \cos^2\theta + (m_3+m_4)[E_1(m_4-m_1)+m_4 Q_{value}]}}{(m_3+m_4)} \right]^2$$

Where M_1, M_3 and M_4 are masses of the incident particles, scattered particles and the residual nucleus respectively. θ is the lab scattering angle, Q_{value} is the amount of energy released or absorbed by the reaction and E_1 is the energy of the incident particles. This equation's complexity can be reduced by denoting the first term by:
An example of how energies of emitted protons vary with the incident beam energy is shown in the tables below.

E_{in}	Eout 135	Eout150
1.8	**3.579**	**3.503**
1.9	**3.645**	**3.565**
2.0	**3.710**	**3.628**
2.1	**3.775**	**3.690**
2.2	**3.841**	**3.753**
2.3	**3.907**	**3.816**
2.4	**3.972**	**3.879**
2.5	**4.038**	**3.943**
2.6	**4.104**	**4.006**
2.7	**4.170**	**4.069**
2.8	**4.236**	**4.132**

Table 4.1: Kinetic energies of emitted protons for the $^{12}(d, p_0)$ reaction at 135° and 150° respectively, for incident deuteron energy E_{in}. All energies are in MeV.

Data presentation and statistics calculations.

These results are presented in a way that their interpretations distinguished by the target used with both beam types come first then followed by the data tables and plots. On the tables, the column labelled E presents the incident beam energy. Q_{inc} is the number of incident particles in coulombs, Q_d is the number of detected emitted particles as taken from spectra peaks in counts, N_c is the normalized number of counts (Q_d/Q_{inc}) in counts/uC and σ is the experimental error. The error was calculated using: $\sigma = \sqrt{Q_d}$

Therefore, the % error on Q_d was given by: $\sqrt{Q_d}/Q_d \times 100\,\%$

The calculation of statistics radiation events is discussed in more details in appendix A. For the theoretical plots of RBS the cross sections were calculated using the Rutherford backscattering cross section formula Eq. (1.22). In the plots Expntl and Theor refer to the experimental and theoretical measurements of the current study respectively.

4.2.1 Results of the D^+ on Carbon foil.

The following results were obtained by accelerating beams of D^+ and $^3He^+$ particles to 1.8 -2.8 MeV incident energy range in steps of 0.1 MeV toward a 50 μg cm^{-2} carbon foil target. Shown in Fig. 4.1 is a spectrum collected for deuterons on carbon foil at 2.4 MeV and 135°.

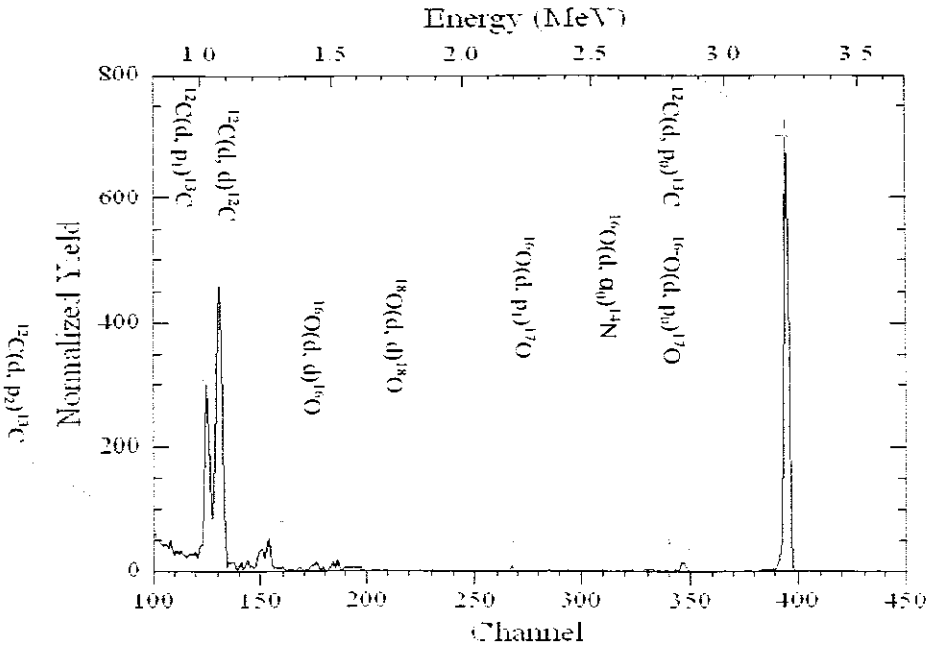

Figure 4.1 Spectrum collected for a 2.4 MeV beam of deuterons detected at 135°

$^{12}C(d, p_0)^{13}C$

In Table 4.2 and Fig. 4.2 a huge variation in the literature and experimental data was observed at 2.4 MeV due to the large errors the resonance at 2.5 MeV could not be resolved. The data to which the experimental data is compared is presented in Appendix B. Table A. Apart from the above-mentioned errors, no huge variations were observed between the plots. Due to the lack data in the nuclear data library the 150 degrees could not be compared. however the trend in the data tends to agree with that seen at 135°.

$^{12}C(d, p_1)^{13}C$

The results presented in Table 4.3 and Fig. 4.3 did not have any data available in the nuclear data library to compare to, they both showed resonance at 2.5 and 2.7 MeV. Any existing variations in these plots may be due to experimental errors.

$^{12}C(d, p_2)^{13}C$

In Table 4.4 and Fig. 4.4 is another plot that did not have a nuclear data within the range available in the nuclear data library. The 150° results also showed to be in a little bit of agreement with Kokkoris et al.'s results below 2.0 MeV with the experimental data normalized to Kokkoris data at 1.8 MeV. Kokkoris data is presented in Appendix B, Table B.

Tables and plots

$E(MeV)$	$C_{inc}(\mu C)$	Q_{d135°	$N_{c135^\circ}(Counts/\mu C)$	σ	Q_{d150°	$N_{c150^\circ}(Counts/\mu C)$	σ
1.8	22	1132	**51.45**	1.53	5561	**252.77**	3.39
1.9	20	928	**46.40**	1.54	4415	**220.75**	3.32
2	22	1049	**47.68**	1.47	3962	**180.09**	2.86
2.1	20	1156	**57.80**	1.70	5544	**277.20**	3.72
2.2	20	1157	**57.85**	1.70	4263	**213.15**	3.26
2.3	20	1008	**50.40**	1.59	3618	**180.90**	3.01
2.4	20	939	**46.95**	1.23	1773	**88.65**	2.11
2.5	20	873	**43.65**	1.48	4292	**214.60**	3.28
2.6	20	686	**34.30**	1.31	2691	**134.55**	2.59
2.7	20	833	**41.65**	1.44	4490	**224.50**	3.35
2.8	20	490	**24.50**	1.11	2281	**114.05**	2.39

Table 4.2: Data collected for the $^{12}C(d, p_0)^{13}C$ reaction at 135° and 150°.

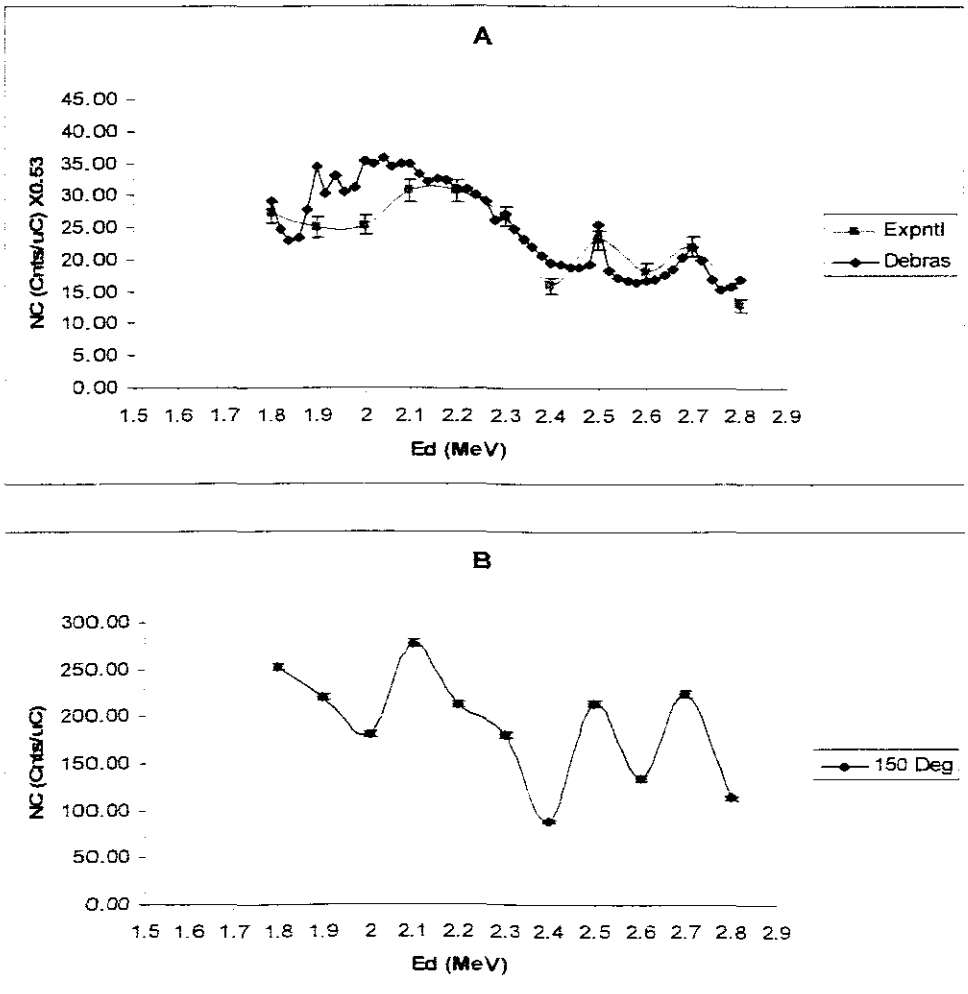

Figure 4.2 In A is a plot of a number of detected protons against the incident beam energy from the $^{12}C(d, p_0)^{13}C$ reaction in the current measurements taken at 135° compared to the cross section data found by Debras et a.l [Deb77]. In B is a plot of number emitted protons for the same reaction at 150°.

$E(MeV)$	$C_{inc}(\mu C)$	Q_{d135^o}	$N_{c135^o}(Counts/\mu C)$	σ	Q_{d150^o}	$N_{c150^o}(Counts/\mu C)$	σ
1.8	22	458	**20.82**	0.97	2426	**110.27**	2.24
1.9	20	228	**11.40**	0.75	503	**25.15**	1.12
2	22	351	**15.95**	0.85	1213	**55.14**	1.58
2.1	20	396	**19.80**	0.99	1682	**84.10**	2.05
2.2	20	409	**20.45**	1.01	1650	**82.50**	2.03
2.3	20	298	**14.90**	0.86	976	**48.80**	1.56
2.4	20	305	**15.25**	0.87	2796	**139.80**	2.64
2.5	20	717	**35.85**	1.34	21274	**1,063.70**	7.29
2.6	20	636	**31.80**	1.26	4367	**218.35**	3.30
2.7	20	2144	**107.20**	2.32	20870	**1,043.50**	7.22
2.8	20	29	**1.45**	0.27	6824	**341.20**	4.13

Table 4.3: Data collected for the $^{12}C(d, p_1)^{13}C$ reaction at 135 and 150°

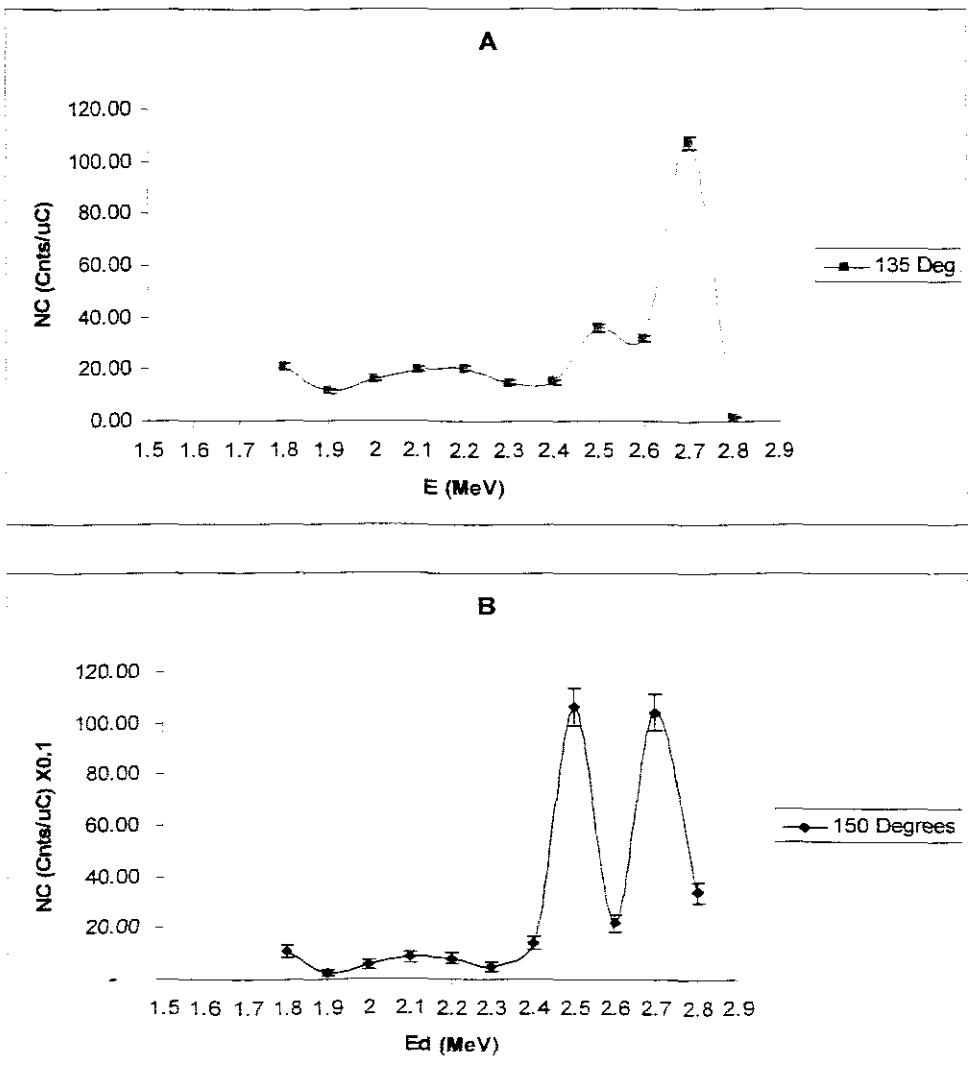

Figure 4.3 In A is plot of counts vs. incident deuteron beam energy for the $^{12}C(d, p_1)^{13}C$ measurements taken at 135° and in B is a plot taken at 150°.

$E(MeV)$	$C_{inc}(\mu C)$	$Q_{d135°}$	$N_{c135°}(Counts/\mu C)$	σ	$Q_{d150°}$	$N_{c150°}(Counts/\mu C)$	σ
1.8	22	623	**28.32**	1.13	1491	**67.77**	1.76
1.9	20	570	**28.50**	1.19	1525	**76.25**	1.95
2	22	597	**27.14**	1.11	894	**40.64**	1.36
2.1	20	433	**21.65**	1.04	539	**26.95**	1.16
2.2	20	329	**16.45**	0.91	427	**21.35**	1.03
2.3	20	57	**2.85**	0.38	463	**23.15**	1.08
2.4	20	47	**2.35**	0.34	315	**15.75**	0.89
2.5	20	325	**16.25**	0.90	808	**40.40**	1.42
2.6	20	47	**10.80**	0.73	698	**34.90**	1.32
2.7	20	46	**13.70**	0.83	731	**36.55**	1.35
2.8	20	41	**9.20**	0.68	429	**21.45**	1.04

Table 4.4: Data collected for the measurements of the $^{12}C(d, p2)^{13}C$ at 135° and 150°

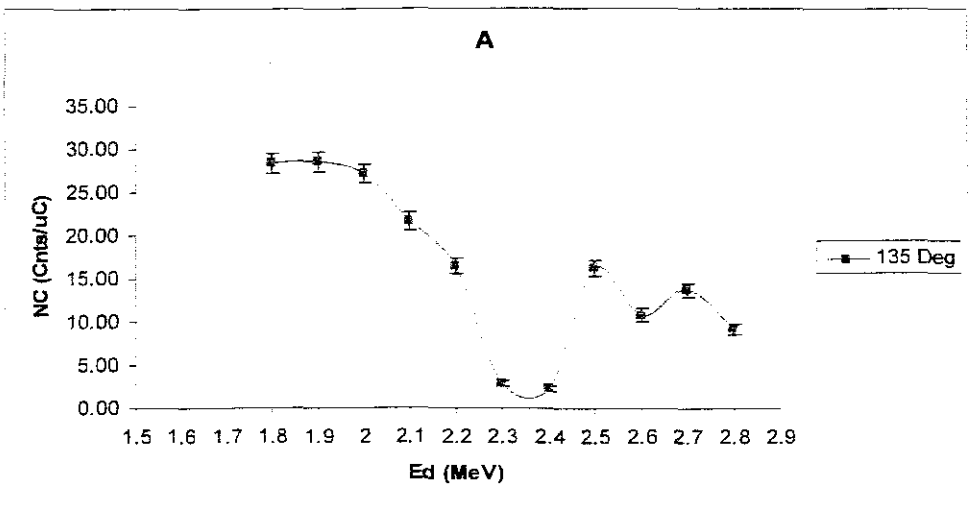

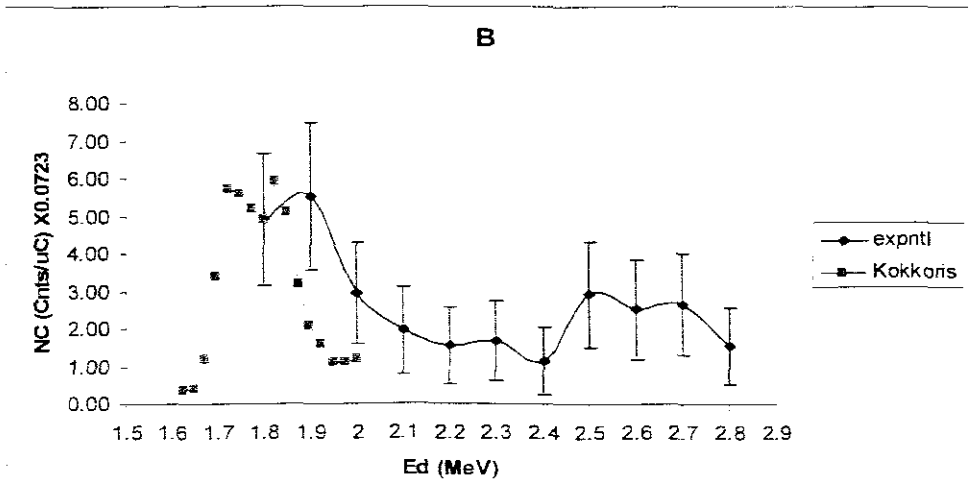

Figure 4.4: In A is a plot of counts vs. beam energy for the $^{12}C(d, p_2)^{13}C$ measurements taken at 135° and in B is a plot for 150° measurements normalized at 1.8 MeV to the cross section data found by Kokkoris et al. [Kok06].

$^{12}C(d, d)^{12}C$

In Table 4.5 and Fig. 4.5, no consistency was observed in the theoretical RBS number of backscattered deuterons and the experimental number of backscattered deuterons. This illustrated the difficulty in reliably extracting the backscattered counts for ^{12}C, which would have included a component of the oxygen surface contamination.

$E(MeV)$	$C_{inc}(\mu C)$	$Q_{d135°}$	$N_{c135°}(Counts/\mu C)$	σ	$Q_{d150°}$	$N_{c150°}(Counts/\mu C)$	σ
1.8	22	535	**24.32**	1.05	2886	**131.18**	2.44
1.9	20	681	**34.05**	1.30	1435	**71.75**	1.89
2	22	310	**14.09**	0.80	1155	**52.50**	1.54
2.1	20	225	**11.25**	0.75	1103	**55.15**	1.66
2.2	20	254	**12.70**	0.24	54	**2.70**	0.37
2.3	20	321	**16.05**	0.21	67	**3.35**	0.41
2.4	20	381	**19.05**	0.34	253	**12.65**	0.80
2.5	20	2010	**100.50**	0.43	105	**5.25**	0.51
2.6	20	474	**23.70**	0.19	62	**3.10**	0.39
2.7	20	10	**32.25**	0.18	43	**2.15**	0.33
2.8	20	1102	**14.40**	0.16	25	**1.25**	0.25

Table 4.5: Data collected for the reaction $^{12}C(d, d)^{12}C$ at 135 and 150° measurements.

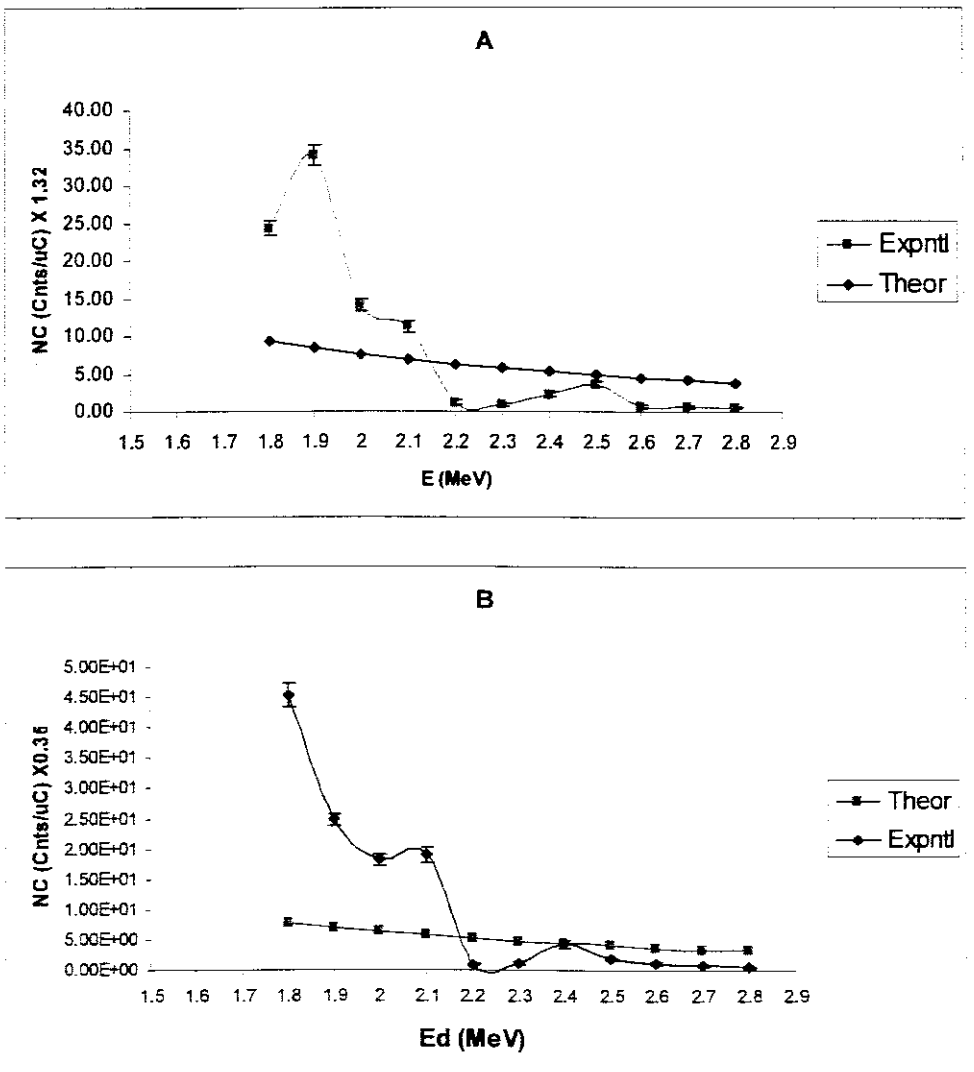

Figure 4.5: Plots of counts vs. beam energy for the $^{12}C(d, d)^{12}C$ measurements taken at 135 and 150° normalized to theoretical RBS plots at 2.5 and 2.4 MeV respectively.

$^{13}C(d, p_i)^{13}C$, $^{13}C(d, \alpha_0)^{11}B$ and $^{13}C(d, d)^{13}C$

Since natural carbon contains only 1.03 % of the ^{13}C isotopes, the reactions of this isotope become very less probable to occur or to be observed especially at low incident energy ranges like 1.8 – 2.8 MeV. Even though some particles emitted due to these reactions were observed in the current study but their statistics was so poor then this resulted in their results being not presented.

$^{16}O(d, p_0)^{17}O$

In Table 4.6 and Fig. 4.6, the results of $^{16}O(d, p_0)^{17}O$ did not show very much variations below 2.2 MeV in the plots. In that plot the experimental measurements and the one from literature had a huge variation at 2.3 MeV where the Debras et al. data plot fell out of error bars, this happened again at energies above 2.4 MeV. Debras et al data is presented in Appendix B, Table C [Deb77].

$^{16}O(d, p_1)^{17}O$

In Fig. 4.7 there were so many variations between the experimental and the literature data with the experimental data having small errors out of which the literature data falls, consistency was only observed at 2.1 – 2.3 MeV. At 2.4 – 2.8 MeV the Debras et al. data started to fall out of the experimental errors. The literature data for this reaction is presented in Appendix B, Table D. The current experimental data is presented in Table 4.7[Deb77].

$E(MeV)$	$C_{inc}(\mu C)$	Q_{d135°	$N_{c135^\circ}(Counts/\mu C)$	σ	Q_{d150°	$N_{c150^\circ}(Counts/\mu C)$	σ
1.8	22	7	**0.32**	0.10	35	**1.59**	0.27
1.9	20	5	**0.50**	0.15	42	**2.10**	0.32
2	22	9	**0.41**	0.14	38	**1.73**	0.28
2.1	20	12	**0.60**	0.17	36	**1.80**	0.30
2.2	20	13	**0.65**	0.18	39	**1.95**	0.31
2.3	20	9	**0.45**	0.15	36	**1.80**	0.30
2.4	20	12	**0.60**	0.17	42	**2.10**	0.32
2.5	20	31	**1.55**	0.28	57	**2.85**	0.38
.6	20	31	**1.55**	0.28	56	**2.80**	0.37
2.7	20	30	**1.50**	0.27	37	**1.85**	0.30
2.8	20	31	**1.55**	0.28	28	**1.40**	0.26

Table 4.6: Data collected at 135 and 150° for the measurements of the $^{16}O(d, p_0)^{17}O$ reaction.

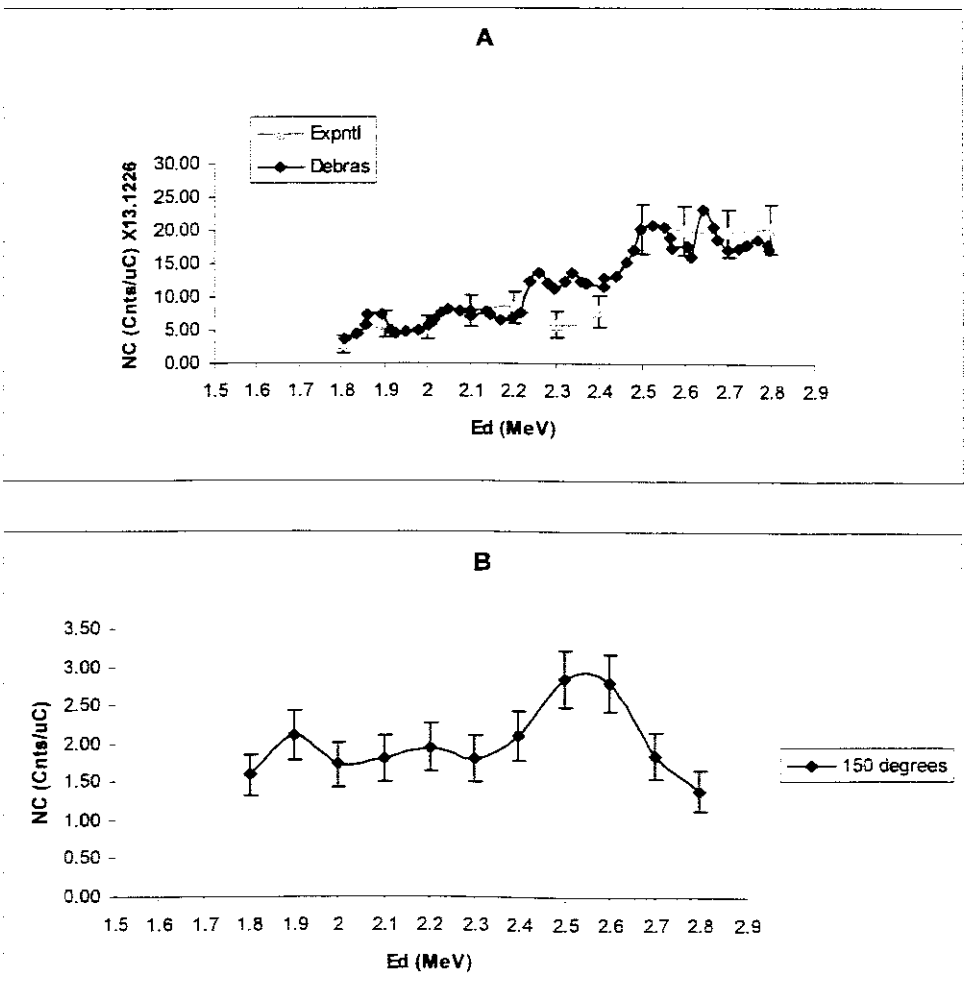

Figure 4.6: Plots of counts vs. beam energy for the $^{16}O(d, p_0)^{17}O$ measurements taken at 135° normalized to the Debras et al. cross section data at 2.5 MeV and the 150° measurements respectively[Deb77].

$E(MeV)$	$C_{inc}(\mu C)$	Q_{d135^o}	$N_{c135^o}(Counts/\mu C)$	σ	Q_{d150^o}	$N_{c150^o}(Counts/\mu C)$	σ
1.8	22	4	**0.18**	0.09	17	**0.77**	0.19
1.9	20	10	**0.50**	0.16	41	**2.05**	0.32
2	22	16	**0.73**	0.18	97	**4.41**	0.45
2.1	20	16	**0.80**	0.20	80	**4.00**	0.45
2.2	20	12	**0.60**	0.17	32	**1.60**	0.28
2.3	20	6	**0.30**	0.12	12	**0.60**	0.17
2.4	20	7	**0.35**	0.13	11	**0.55**	0.17
2.5	20	2	**0.10**	0.07	53	**2.65**	0.36
2.6	20	6	**0.30**	0.12	22	**1.10**	0.23
2.7	20	4	**0.20**	0.10	24	**1.20**	0.24
2.8	20	5	**0.25**	0.11	20	**1.00**	0.22

Table 4.7: Data collected for the measurements of the $^{16}O(d, p_1)^{17}O$ at 135 and 150°.

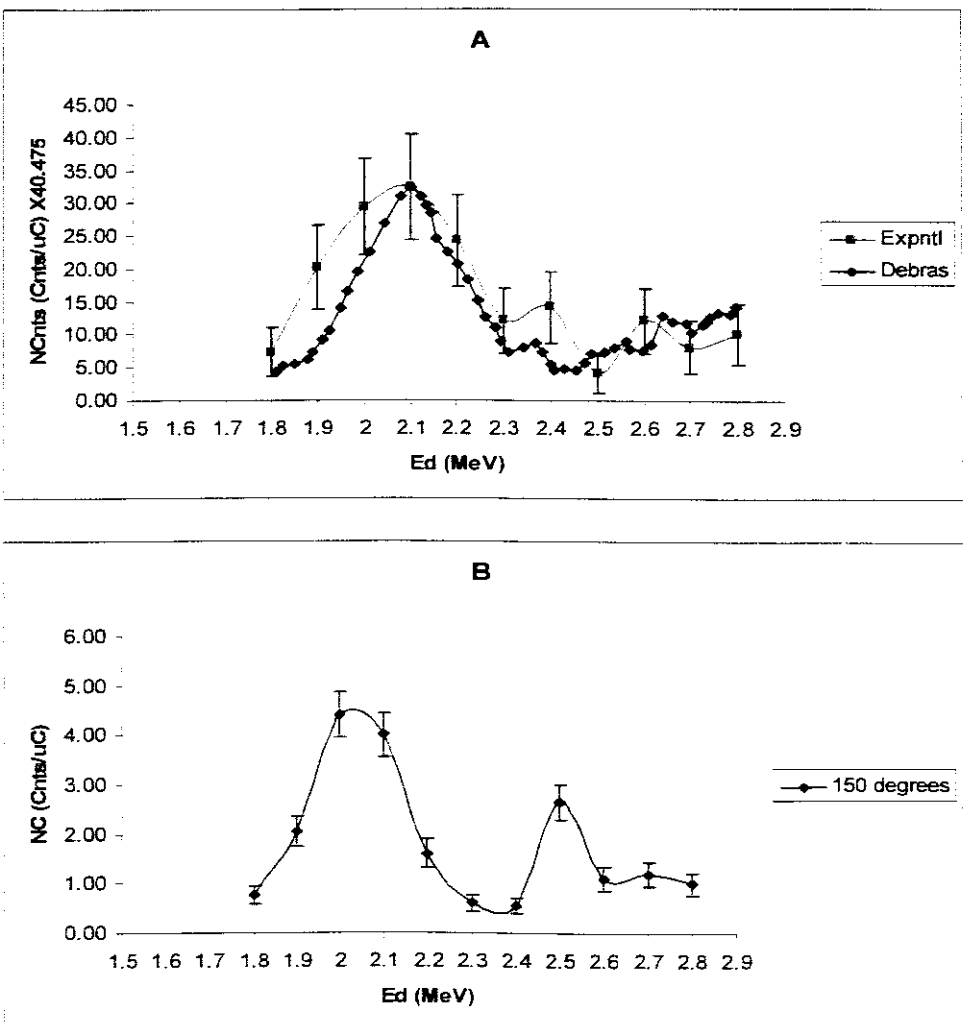

Figure 4.7: Plots of counts vs. beam energy for the $^{16}O(d, p_1)^{17}O$ measurements taken at 135° normalized to the cross sections data found by Debraset al. 2.1 MeV [Deb77]. and a plot of current measurements taken at 150° respectively.

$^{16}O(d, \alpha_0)^{14}N$

This reaction gave very low numbers of counts at both 135° and 150° scattering angles, which resulted in very poor statistics in the measurements then the data and the plots were not included in the current results.

$^{18}O(d, \alpha_i)^{16}N$

The peaks due to these reactions could not be observed on spectra, which means no results for these reactions could be presented under the carbon foil results.

$^{16}O(d, d)^{16}O$

The RBS results are presented in Table 4.8 and Fig. 4.8, whereby they are normalized to the theoretical RBS measurements at 2.3 MeV. The experimental plot seemed to follow trends of the theoretical measurements. However, the measurements for RBS measurements on ^{18}O target cold not be presented due to a very poor statistics.

$E(MeV)$	$C_{inc}(\mu C)$	Q_{d135^o}	$N_{c135^o}(Counts/\mu C)$	σ	Q_{d150^o}	$N_{c150^o}(Counts/\mu C)$	σ
1.8	22	19	**0.86**	0.20	201	**9.14**	2.38
1.9	20	23	**1.15**	0.24	155	**7.75**	2.30
2	22	35	**1.59**	0.27	56	**2.55**	1.26
2.1	20	27	**1.35**	0.26	70	**3.50**	1.55
2.2	20	5	**0.25**	0.11	54	**2.70**	1.36
2.3	20	17	**0.85**	0.21	67	**3.35**	1.51
2.4	20	45	**2.25**	0.34	35	**1.75**	1.09
2.5	20	53	**1.00**	0.22	18	**0.90**	0.78
2.6	20	14	**0.70**	0.19	20	**1.00**	0.83
2.7	20	6	**0.30**	0.12	11	**0.55**	0.61
2.8	20	20	**0.50**	0.16	11	**0.55**	0.61

Table 4.8 Number of counts taken from the spectra of $^{16}O(d, d)^{16}O$ at 135° and 150

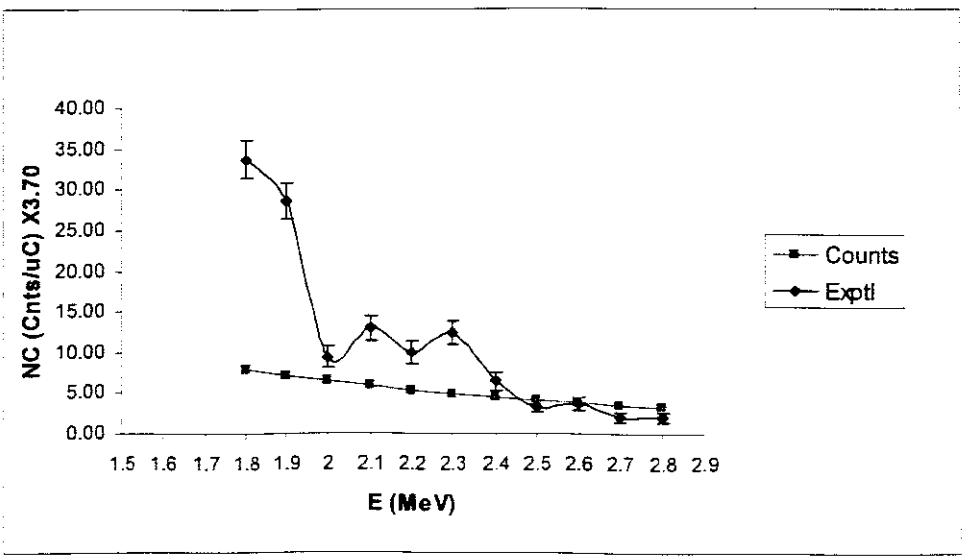

Figure 4.8: Experimental plot of counts vs. incident beam energy for the $^{16}O(d, d)^{16}O$ measurements taken at 150° respectively normalized to the theoretical RBS measurements at 2.3 MeV.

4.2.2 Results of the $^{3}He^{+}$ on the carbon foil target.

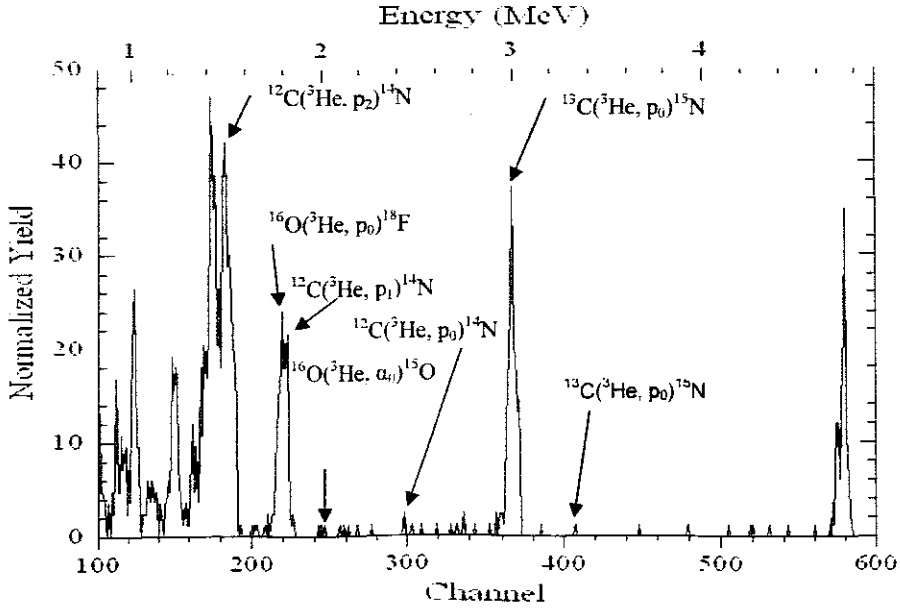

Figure 4.9: A spectrum collected for the 2.6 MeV $^{3}He^{+}$ beam on the carbon foil at 150°.

$^{12}C(^{3}He, p_0)^{14}N$

In Table 4.9 and Fig. 4.10, the results for the $^{12}C(^{3}He, p_0)^{13}C$ reaction taken at 150° showed to be consistent with the results taken from the nuclear data library for a 159.4° scattering angle except at 2.4 MeV. However, the 135° measurements gave a very poor statistics so they were not plotted. The literature data for this reaction is presented in Appendix B, Table E

$^{12}C(^{3}He, p_1)^{14}N$

In Table 4.10 and Fig. 4.11, no particles could be detected for the 135° measurements at energies lower than 2.1 MeV, but above 2.1 MeV there was a bit of consistence between the measurements taken at the two scattering angles. Even though the results seemed in agreement but there is a discrepancy for the 150° results at 2.3 where Kuan et al. 159.4° data falls out of error bars [Kua64], which may be due to energy experimental errors. The literature data for this reaction is presented in Appendix B, Table F.

$^{12}C(^{3}He, p_2)^{14}N$

The data and plots are shown in Table 4.11 and Fig. 4.12 showed an agreement in the experimental and the Kuan et al. 159.4° cross section data with discrepancies only appearing above 2.5 MeV, which still fell within the error bars. The literature data for this reaction is presented in Appendix B, Table G [Kua64].

$E(MeV)$	$C_{inc}(\mu C)$	$Q_{d150°}$	$N_{c150°}(Counts/\mu C)$	σ	$Q_{d135°}$	$N_{c135°}(Counts/\mu C)$	σ
1.8	2.00						
1.9	2.00	2	**0.07**	0.32			
2	2.00	3	**0.08**	0.37	2	**0.09**	0.30
2.1	2.00	2	**0.07**	0.32	1	**0.05**	0.22
2.2	2.00	5	**0.11**	0.50	2	**0.10**	0.32
2.3	2.00	8	**0.14**	0.63	4	**0.20**	0.45
2.4	2.12	7	**0.13**	0.59	4	**0.20**	0.45
2.5	2.00	18	**0.21**	0.95	9	**0.45**	0.67
2.6	2.00	29	**0.27**	1.20	5	**0.25**	0.50
2.7	2.00	32	**0.28**	1.26	7	**0.35**	0.59

Table 4.9: Number of counts taken from spectra for $^{12}C(^{3}He, p_0)^{14}N$ at 135 and 150°.

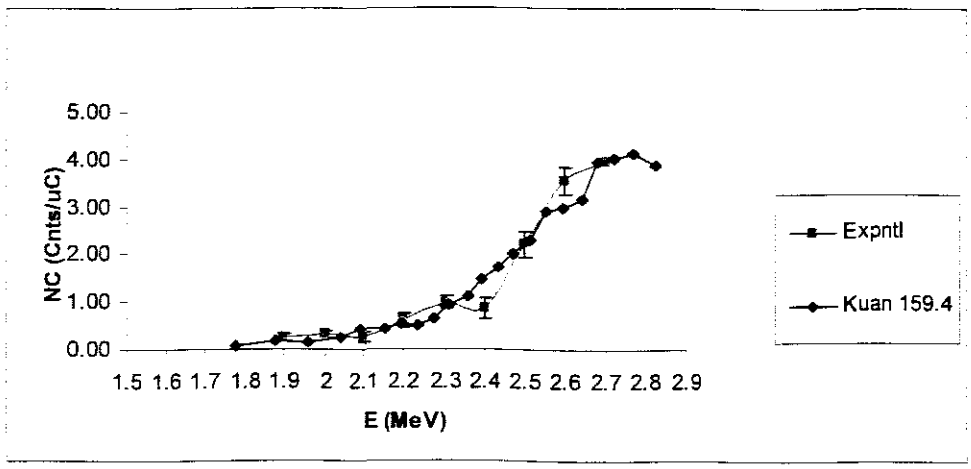

Figure 4.10: In A is a plot of counts vs. beam energy for the $^{12}C(^{3}He, p_0)^{14}N$ measurements taken at 150° normalized to the cross sections data calculated by Kuan et al. at 2.7 MeV and 159.4° [Kua64].

$E(MeV)$	$C_{inc}(\mu C)$	$Q_{d135°}$	$N_{c135°}(Counts/\mu C)$	σ	$Q_{d150°}$	$N_{c150°}(Counts/\mu C)$	σ
1.8	2.00						
1.9	2.00						
2	2.00				5	**2.50**	1.12
2.1	2.00	2	**1.00**	0.71	6	**3.00**	1.22
2.2	2.00	5	**2.50**	1.12	9	**4.50**	1.50
2.3	2.00	5	**2.50**	1.12	22	**11.00**	2.35
2.4	2.12	8	**3.77**	1.33	44	**20.75**	3.13
2.5	2.00	8	**4.00**	1.41	27	**13.50**	2.60
2.6	2.00	5	**2.50**	1.12	31	**15.50**	2.78
2.7	2.00	4	**2.00**	1.00	18	**9.00**	2.12

Table 4.10: Number of counts taken from spectra for $^{12}C(^3He, p_1)^{14}N$ for measurements taken at 135 and 150 degrees

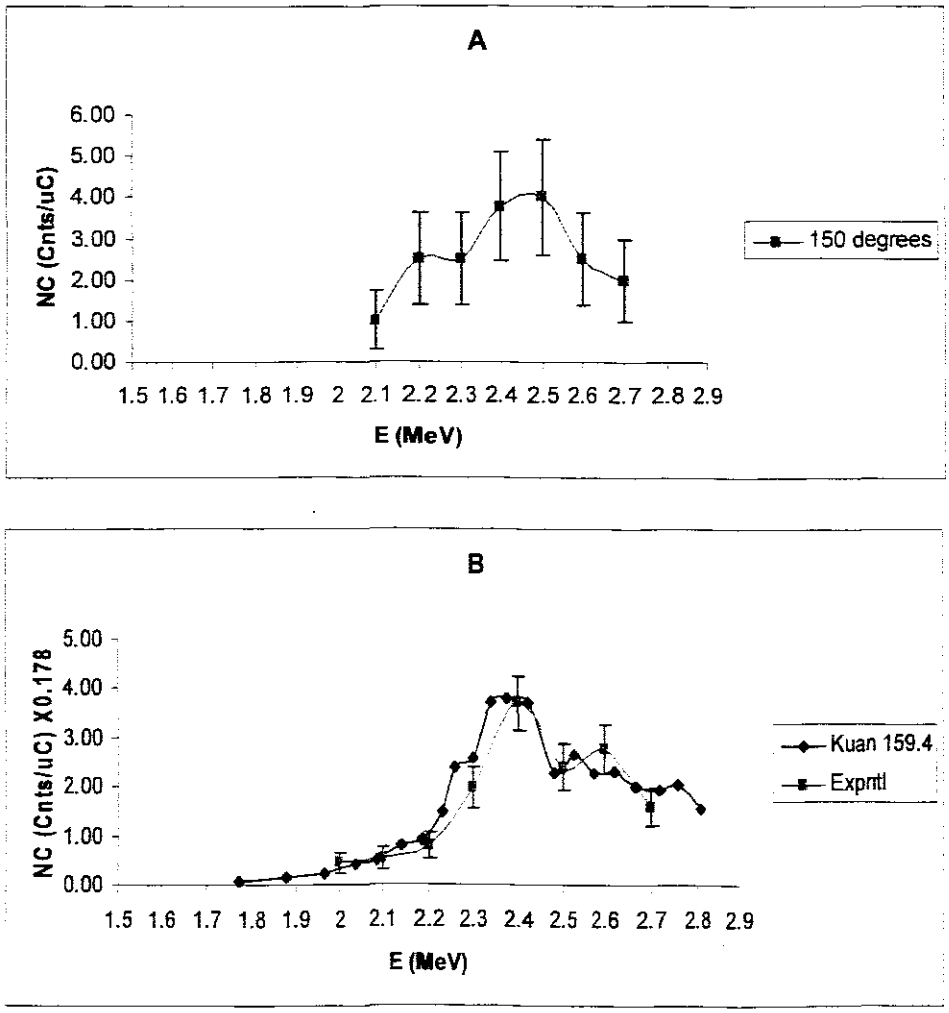

Figure 4.11: A plot of counts vs. incident beam energy for the $^{12}C(^3He, p_1)^{14}N$ measurements taken at 150° normalized to Kuan et al. cross sections data taken at 159.4° at 2.4 MeV [Kua64].

$E(MeV)$	$C_{inc}(\mu C)$	Q_{d135°	$N_{c135^\circ}(Counts/\mu C)$	σ	Q_{d150°	$N_{c150^\circ}(Counts/\mu C)$	σ
1.8	2.00	3	**1.50**	0.87	2	**1.00**	0.71
1.9	2.00	2	**1.00**	0.71	2	**1.00**	0.71
2	2.00	2	**1.00**	0.71	5	**2.50**	1.12
2.1	2.00	1	**0.50**	0.50	7	**3.50**	1.32
2.2	2.00	3	**1.50**	0.87	8	**4.00**	1.41
2.3	2.00	6	**3.00**	1.22	22	**11.00**	2.35
2.4	2.12	5	**2.36**	1.05	30	**14.15**	2.58
2.5	2.00	6	**3.00**	1.22	22	**11.00**	2.35
2.6	2.00	6	**3.00**	1.22	20	**10.00**	2.24
2.7	2.00	4	**2.00**	1.00	15	**7.50**	1.94

Table 4.11: Number of counts taken from spectra for $^{12}C(^3He, p_2)^{14}N$ for measurements taken at 135 and 150°.

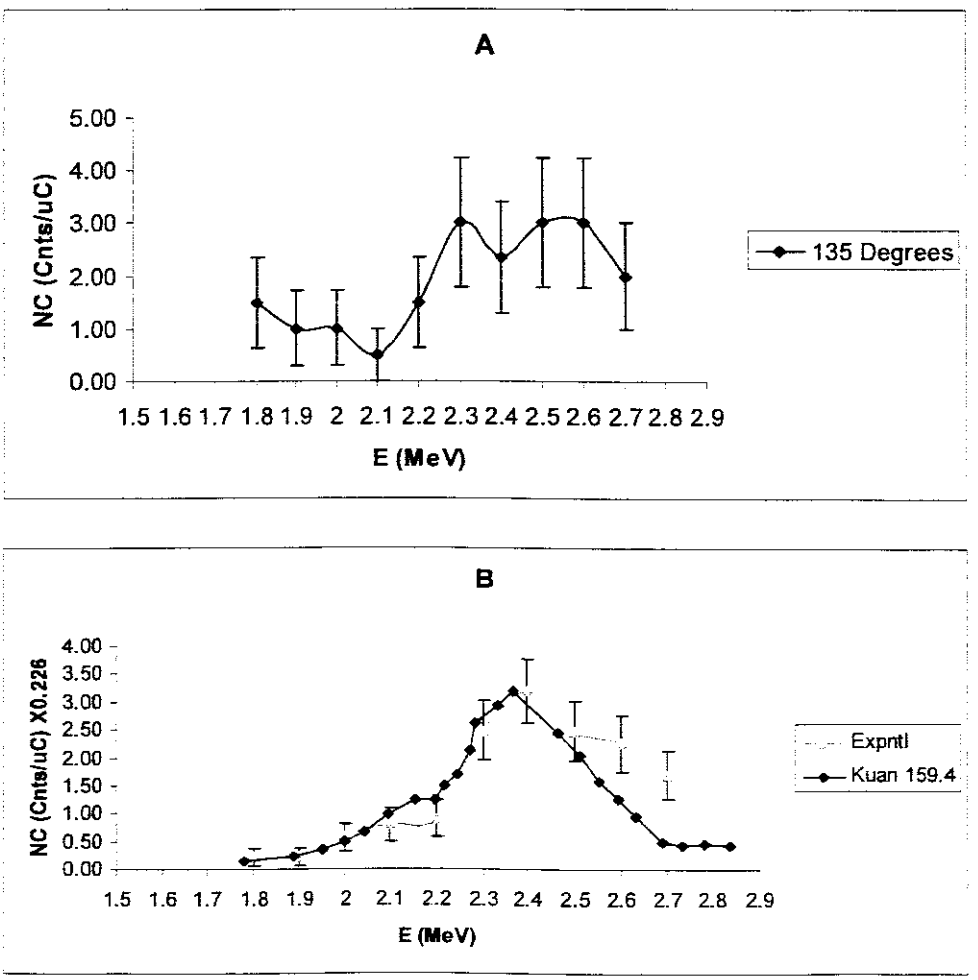

Figure 4.12: A plot of counts vs. incident beam energy for the $^{12}C(^3He, p_2)^{14}N$ measurements taken at 150° normalized to Kuan et al. cross sections data taken at 159.4° at 2.4 MeV [Kua64], in A is a plot of 135°

$^{12}C(^{3}He, ^{3}He)^{12}C$

Table 4.12 presents the data collected for the experimental measurements for this backscattering experiment. In Fig. 4.13 the 135° experimental plot could be plotted but it never followed the trends of the RBS theoretical plot and since they could not be compared to any other measurements obtained from the literature.

$E(MeV)$	$C_{inc}(\mu C)$	Q_{d135°	$N_{c135^\circ}(Counts/\mu C)$	σ	Q_{d150°	$N_{c150^\circ}(Counts/\mu C)$	σ
1.8	2.00	13	**6.50**	1.80	37	**18.50**	3.04
1.9	2.00	8	**4.00**	1.41	19	**9.50**	2.18
2	2.00	15	**7.50**	1.94	53	**26.50**	3.64
2.1	2.00	12	**6.00**	1.73	22	**11.00**	2.35
2.2	2.00	13	**6.50**	1.80	28	**14.00**	2.65
2.3	2.00	10	**5.00**	1.58	48	**24.00**	3.46
2.4	2.12	7	**3.30**	1.25	23	**10.85**	2.26
2.5	2.00	6	**3.00**	1.22	21	**10.50**	2.29
2.6	2.00	8	**4.00**	1.41	23	**11.50**	2.40
2.7	2.00	9	**4.50**	1.50	27	**13.50**	2.60

Table 4.12: Number of counts taken from spectra for $^{12}C(^{3}He, 3He)^{12}C$ for measurements taken at 135 and 150 degrees

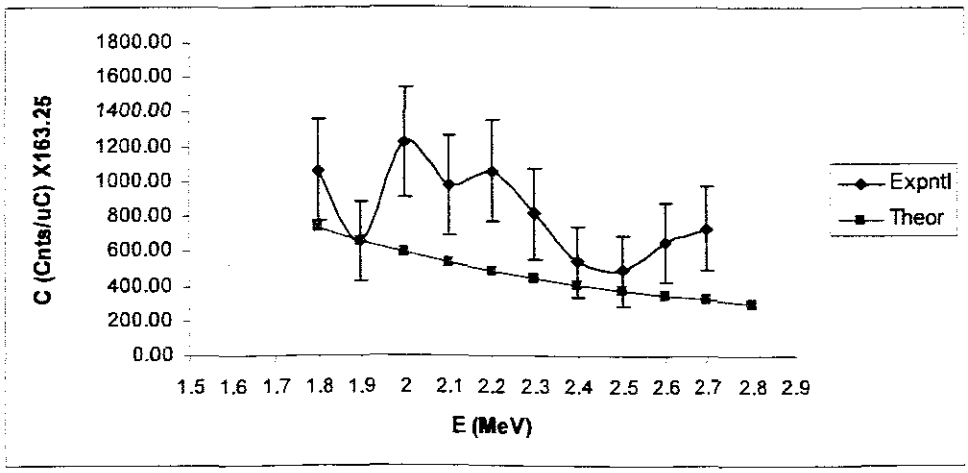

Figure 4.13: An experimental plot of counts vs. incident beam energy for the $^{12}C(^{3}He,^{3}He)^{12}C$ measurements taken at 135° normalized to the RBS theoretical plot at 1.9 MeV.

$^{13}C(^{3}He, ^{3}He)^{13}C$

Due to the very low percentage of ^{13}C (1.03 %) in natural carbon, this reaction results could not give a good statistics so its data and plots had to be eliminated.

4.2.4 Results of the D^+ on Boric acid (HBO_3) crystal.

To find Q_{values} for the reaction, energy level scheme diagrams showing excitation energies of the required residual nuclei had to be used. This was done by subtracting the excitation energies of the residual nuclei from the energy released by the reaction, which is the Q_{value} given by: $$Q_{value} = (M_1 + M_2)\cdot c^2 - (M_4 + M_3)\cdot c^2$$

The energy level schemes diagrams for ^{11}B are shown in Fig. 1 in appendix C, which enabled us to find the Q_{values} of the reactions emitting protons leaving ^{11}B on the ground and for excited states with angular momentums, $3/2^-, 1/2^-, 5/2^-, 3/2^-, 7/2^-$ with the emitted protons being p_0, p_1, p_2, p_3 and p_4. The Q_{values} were then used to calculate energies of the emitted particles using the same equation as in the case of carbon foil target results. The energy level scheme diagram used for the calculation of $^{11}B(d, \alpha_i)^9Be$ is shown in Fig. 2 and the one used for $^{10}B(d, \alpha_i)^8Be$ reactions was taken from [AJZ88].

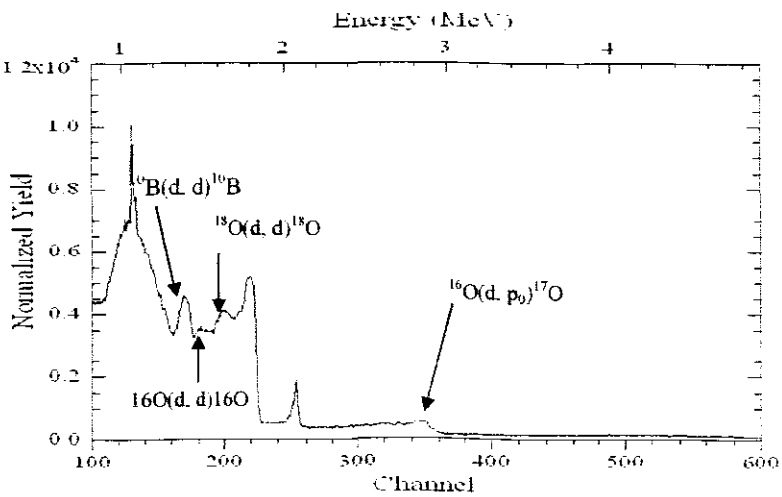

Figure 4.14: Un-calibrated spectrum for2.6 MeV D^+ on boric acid at 150°

$^{10}B(d, p_0)^{11}B$

The variability of cross sections with the angles of scattering sometimes makes counts for the same reactions, at the same incident beam energies not to be observed at some other scattering angles. This was the case for the above reaction when a very few counts leading to poor statistics were observed for the reaction at 135°, while enough counts were observed for the same reaction at the same incident beam energy range at 150°. These results are presented in Table 4.13 and plotted in Fig. 4.15. due to the lack of data in the literature for the (d, p_i) reactions on boron these results were not compared to anything.

$^{10}B(d, p_1)^{11}B$

A very low number of counts was observed for this reaction at 135°, which then gave a very poor statistics in a way that the plot could not be presented, this is presented in Table 4.14. For this reaction the maximum number of counts was observed at 2.7 MeV incident beam energy as shown in Fig. 4.16, which means that is where the maximum cross section for this reaction at 150° could be found.

$^{10}B(d, p_2)^{11}B$

A low number of emitted protons leading to a poor statistics was observed again for this reaction at 135° presented on Table 4.15, then only the 150° plot could be presented in Fig. 4.17.

$^{10}B(d, p3)^{11}B$

The results for this reaction's measurements are presented in Table 4.16 and Fig. 4.18. However the results for the 135° measurements still had poor statistics, this is shown by the number of normalized counts (in counts/uC) that could be found between 0.1 - 2.28 at 1.8 MeV on the plot. For the 150° the maximum number of normalized counts was observed at 2.7 MeV.

$^{10}B(d, p_4)^{11}B$

Like in the above mentioned reaction, the number of detected protons for this reaction at 135° was still low, these results are presented in Table 4.17 and Fig. 4.19. The results were better for the 150° measurements. This showed a better probability of detecting emitted protons for the same reaction at 150° than at 135°.

$E(MeV)$	$C_{inc}(\mu C)$	$Q_{d135°}$	$N_{c135°}(Counts/\mu C)$	σ	$Q_{d150°}$	$N_{c150°}(Counts/\mu C)$	σ
1.8	20.2	9	**0.45**	0.15	35.00	**1.73**	0.29
1.9	20	7	**0.35**	0.13	47.00	**2.35**	0.34
2	26	9	**0.35**	0.12	36.00	**1.38**	0.23
2.1	20	4	**0.20**	0.10	70.00	**3.50**	0.42
2.2	20	8	**0.40**	0.14	60.00	**3.00**	0.39
2.3	20	5	**0.25**	0.11	48.00	**2.40**	0.35
2.4	20	9	**0.45**	0.15	52.00	**2.60**	0.36
2.5	20	5	**0.25**	0.11	74.00	**3.70**	0.43
2.6	20	10	**0.50**	0.16	92.00	**4.60**	0.48
2.7	20	5	**0.25**	0.11	68.00	**3.40**	0.41
2.8	20	4	**0.20**	0.10	58.00	**2.90**	0.38

Table 4.13: Number of counts taken from spectra for $^{10}B(d, p_0)^{11}B$ collected at 135° and 150°.

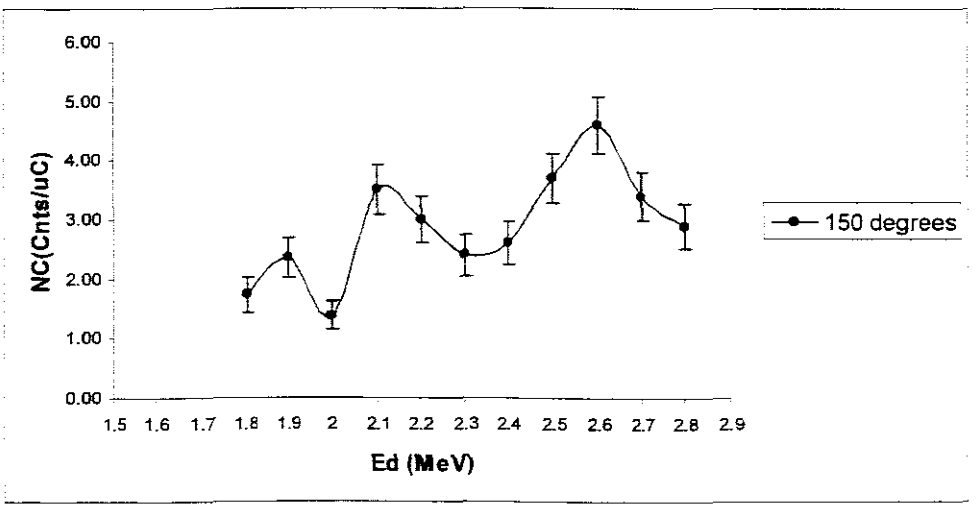

Figure 4.15: Experimental plots of counts vs. incident beam energy for the $^{10}B(d, p_0)^{11}B$ measurements taken at 150°.

$E(MeV)$	$C_{inc}(\mu C)$	Q_{d135^o}	$N_{c135^o}(Counts/\mu C)$	σ	Q_{d150^o}	$N_{c150^o}(Counts/\mu C)$	σ
1.8	20.2	7	**0.35**	0.13	25	**1.24**	0.25
1.9	20	6	**0.30**	0.12	33	**1.65**	0.29
2	26	8	**0.31**	0.11	31	**1.19**	0.21
2.1	20	14	**0.70**	0.19	51	**2.55**	0.36
2.2	20	7	**0.35**	0.13	60	**3.00**	0.39
2.3	20	11	**0.55**	0.17	48	**2.40**	0.35
2.4	20	17	**0.85**	0.21	49	**2.45**	0.35
2.5	20	21	**1.05**	0.23	81	**4.05**	0.45
2.6	20	22	**1.10**	0.23	93	**4.65**	0.48
2.7	20	13	**0.65**	0.18	111	**5.55**	0.53
2.8	20	19	**0.95**	0.22	70	**3.50**	0.42

Table 4.14 Number of counts taken from spectra for $^{10}B(d, p_1)^{11}B$ collected at 135° and 150°.

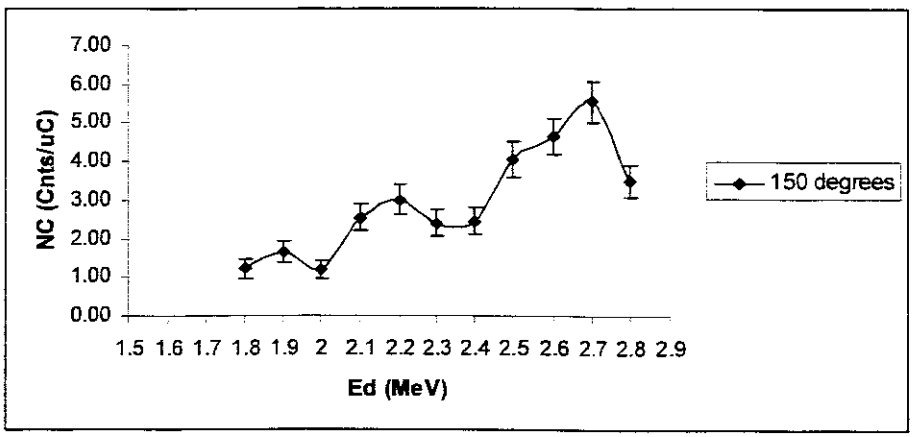

Figure 4.16: Experimental plots of counts vs. incident beam energy for the $^{10}B(d, p_1)^{11}B$ measurements taken at 150°.

$E(MeV)$	$C_{inc}(\mu C)$	Q_{d135^o}	$N_{c135^o}(Counts/\mu C)$	σ	Q_{d150^o}	$N_{c150^o}(Counts/\mu C)$	σ
1.8	20.2	24	**1.19**	0.24	126	**6.24**	0.56
1.9	20	25	**1.25**	0.25	132	**6.60**	0.57
2	26	15	**0.58**	0.15	143	**5.50**	0.46
2.1	20	18	**1.35**	0.32	214	**10.70**	0.73
2.2	20	27	**0.50**	0.10	172	**8.60**	0.66
2.3	20	10	**1.40**	0.44	174	**8.70**	0.66
2.4	20	28	**1.25**	0.24	187	**9.35**	0.68
2.5	20	25	**1.60**	0.32	235	**11.75**	0.77
2.6	20	32	**1.35**	0.24	305	**15.25**	0.87
2.7	20	27	**2.05**	0.39	300	**15.00**	0.87
2.8	20	41	**2.05**	0.32	230	**11.50**	0.76

Table 4.15: Number of counts taken from spectra for $^{10}B(d, p_2)^{11}B$ collected at 135° and 150°.

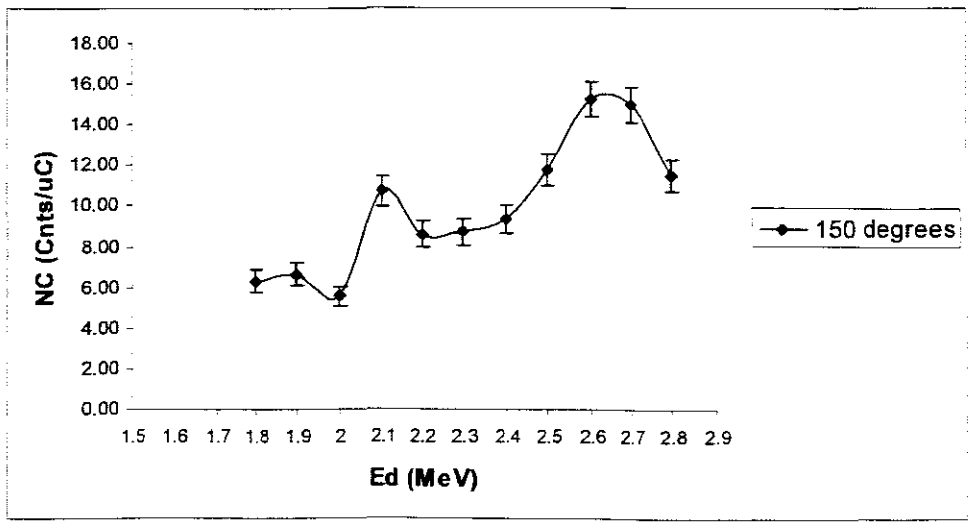

Figure 4.17: Experimental plot of counts vs. incident beam energy for the $^{10}B(d, p_2)^{11}B$ measurements taken at 150°.

$E(MeV)$	$C_{inc}(\mu C)$	Q_{d135^o}	$N_{c135^o}(Counts/\mu C)$	σ	Q_{d150^o}	$N_{c150^o}(Counts/\mu C)$	σ
1.8	20.2	24	**1.19**	0.24	132	**6.53**	0.57
1.9	20	27	**1.35**	0.26	130	**6.50**	0.57
2	26	29	**1.12**	0.21	156	**6.00**	0.48
2.1	20	38	**1.90**	0.31	179	**8.95**	0.67
2.2	20	24	**1.20**	0.24	193	**9.65**	0.69
2.3	20	23	**1.15**	0.24	156	**7.80**	0.62
2.4	20	27	**1.35**	0.26	157	**7.85**	0.63
2.5	20	28	**1.40**	0.26	208	**10.40**	0.72
2.6	20	35	**1.75**	0.30	310	**15.50**	0.88
2.7	20	33	**1.65**	0.29	268	**13.40**	0.82
2.8	20	46	**2.30**	0.34	241	**12.05**	0.78

Table 4.16: Number of counts taken from a spectra of $^{10}B(d, p_3)^{11}B$ collected at 135° and 150°.

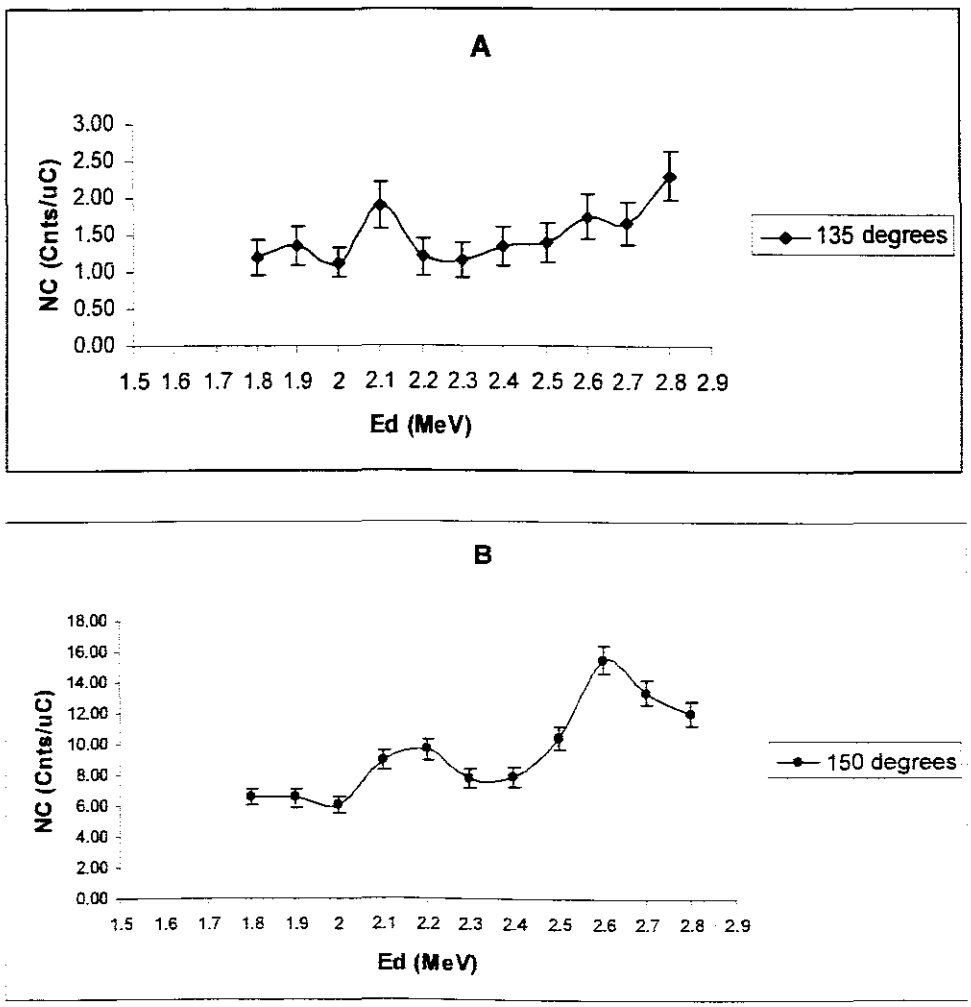

Figure 4.18: Experimental plot of counts vs. incident beam energy for the $^{10}B(d, p_3)^{11}B$ measurements taken at 135 and 150° respectively.

$E(MeV)$	$C_{inc}(\mu C)$	Q_{d135^o}	$N_{c135^o}(Counts/\mu C)$	σ	Q_{d150^o}	$N_{c150^o}(Counts/\mu C)$	σ
1.8	20.2	31	**1.53**	0.28	926	**45.84**	1.51
1.9	20	34	**1.70**	0.29	685	**34.25**	1.31
2	26	68	**2.62**	0.32	1385	**53.27**	1.43
2.1	20	55	**2.75**	0.37	1844	**92.20**	2.15
2.2	20	51	**2.55**	0.36	1316	**65.80**	1.81
2.3	20	69	**3.45**	0.42	1562	**78.10**	1.98
2.4	20	76	**3.80**	0.44	1588	**79.40**	1.99
2.5	20	63	**3.15**	0.40	1647	**82.35**	2.03
2.6	20	75	**3.75**	0.43	1599	**79.95**	2.00
2.7	20	63	**3.15**	0.40	2914	**145.70**	2.70
2.8	20	53	**2.65**	0.36	2889	**144.45**	2.69

Table 4.17: Number of counts taken from a spectra of $^{10}B(d, p_4)^{11}B$ collected at 135° and 150°.

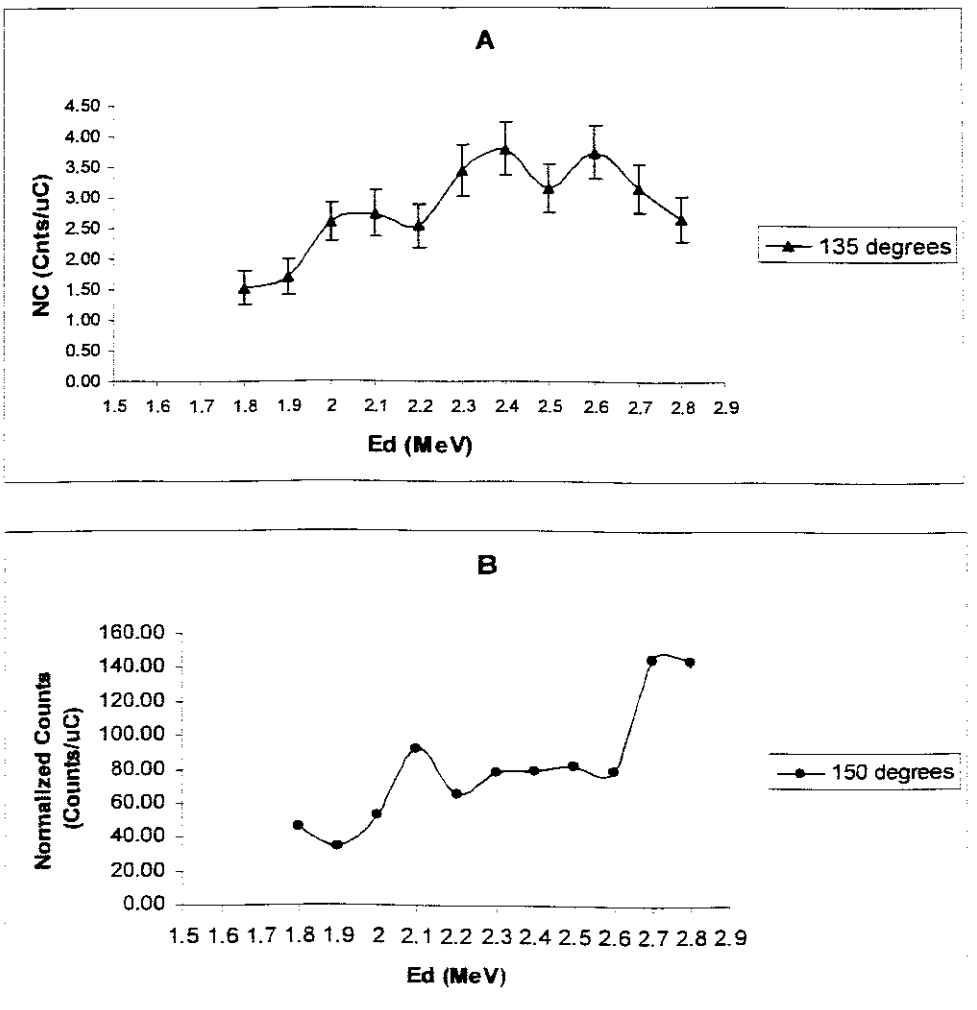

Figure 4.19: Experimental plot of counts vs. incident beam energy for the $^{10}B(d, p_4)^{11}B$ measurements taken at 135 and 150° respectively.

$^{11}B(d, p_0)^{12}B$

The results for the measurements of this reaction are presented in Table 4.18 and Fig. 4.20 and they are not normalized to any cross sections data. The plots for the results of measurements taken at the two scattering angles showed to be not consistence, where as consistency is always expected for the plots of the same incident beam type and energy, this may have been caused by experimental errors.

$E(MeV)$	$C_{inc}(\mu C)$	Q_{d135^o}	$N_{c135^o}(Counts/\mu C)$	σ	Q_{d150^o}	$N_{c150^o}(Counts/\mu C)$	σ
1.8	20.2	119	**5.89**	0.54	1334	**66.04**	1.81
1.9	20	183	**9.15**	0.68	1193	**59.65**	1.73
2	26	258	**9.92**	0.62	2087	**80.27**	1.76
2.1	20	243	**12.15**	0.78	3772	**188.60**	3.07
2.2	20	213	**10.65**	0.73	3888	**194.40**	3.12
2.3	20	207	**10.35**	0.72	3666	**183.30**	3.03
2.4	20	246	**12.30**	0.78	2535	**126.75**	2.52
2.5	20	292	**14.60**	0.85	1834	**91.70**	2.14
2.6	20	362	**18.10**	0.95	2850	**142.50**	2.67
2.7	20	471	**23.55**	1.09	2646	**132.30**	2.57
2.8	20	561	**28.05**	1.18	2888	**144.40**	2.69

Table 4.18: Number of counts taken from a spectra of $^{11}B(d, p_0)^{12}B$ collected at 135° and 150°.

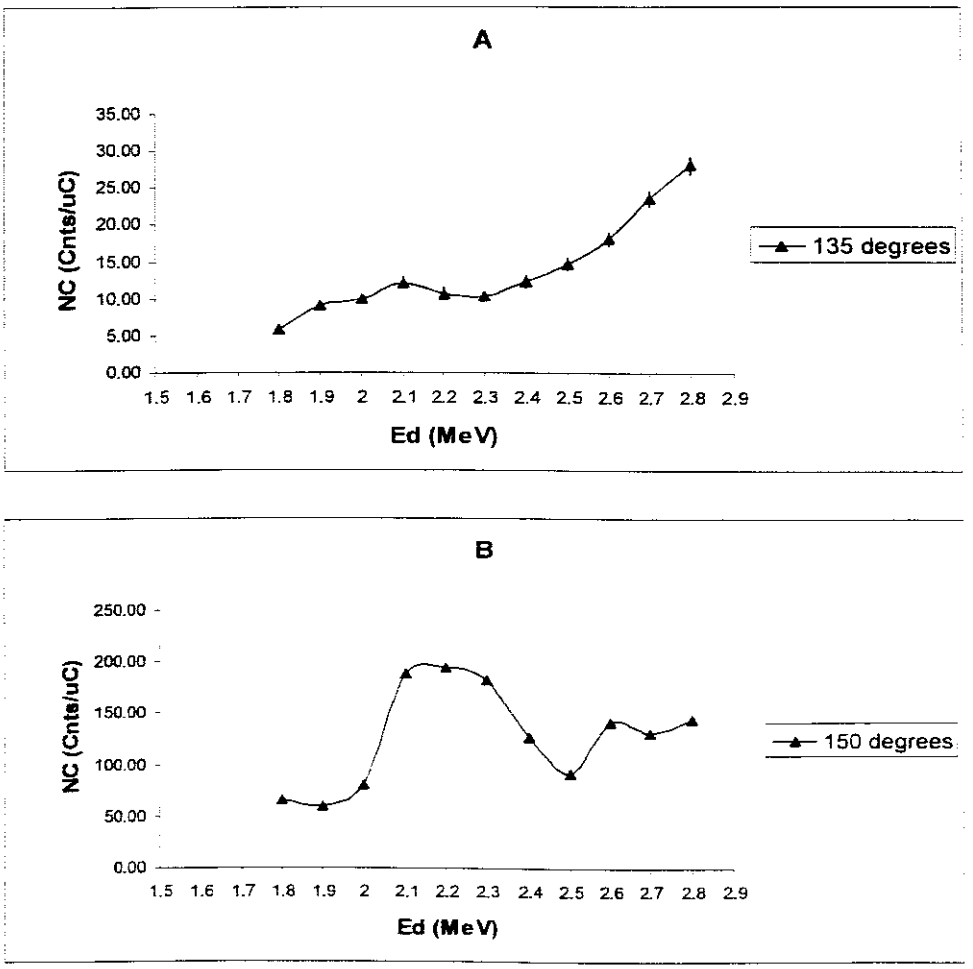

Figure 4.20: Experimental plot of counts vs. incident beam energy for the $^{11}B(d, p_0)^{12}B$ measurements taken at 135 and 150° respectively.

$^{10}B(d, \alpha_0)^8Be$

No counts were observed for this reaction at 135°, even though some counts were observed at 150° but the statistics showed to be of a very low quality. This showed this reaction to be a weak reaction. These results are presented in Table 4.19 and Fig. 4.21.

$^{10}B(d, \alpha_1)^8Be$

Even though this reaction leaves the ^8Be residual nucleus in the excited state but it seems weak still, since its measurements taken at 135° gave a very poor statistics. The data for the measurements is presented in Table 4.20. The plot that could be plotted was the one for the 150° measurements shown in Fig. 4.22, which did not give a good statistics either.

$^{10}B(d, \alpha_2)^8Be$

From this excited state of ^8Be some protons emitted from the reaction could be detected at 135°, however with poor statistics. The 150° measurement showed a better statistics. The data and plots for both 135 and 150° measurements are presented in Table 4.21 and Fig. 4.23 respectively.

$^{10}B(d, \alpha_3)^8Be$

This reaction gave better statistics for both 135° and 150° as more number of emitted alpha particles were detected. Even though the results were not compared to any nuclear data library but the confidence is better on them. These data and plots are presented in Table 4.22 and Fig. 4.24 respectively.

$E(MeV)$	$C_{inc}(\mu C)$	Q_{d150^o}	$N_{c150^o}(Counts/\mu C)$	σ
1.8	20.2	28	**1.39**	0.26
1.9	20	30	**1.50**	0.27
2	26	32	**1.23**	0.22
2.1	20	55	**2.75**	0.37
2.2	20	39	**1.95**	0.31
2.3	20	33	**1.65**	0.29
2.4	20	38	**1.90**	0.31
2.5	20	51	**2.55**	0.36
2.6	20	44	**2.20**	0.33
2.7	20	51	**2.55**	0.36
2.8	20	52	**2.60**	0.36

Table 4.19: Number of counts taken from a spectrum of $^{10}B(d, \alpha_0)^8Be$ collected at 150°.

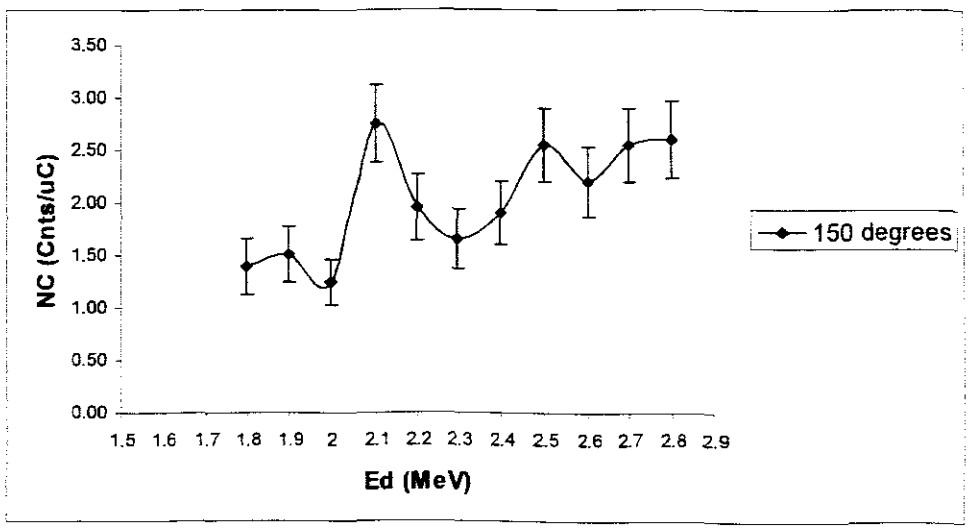

Figure 4.21: Experimental plot of counts vs. incident beam energy for the $^{10}B(d, \alpha_0)^8Be$ measurements taken at 150° .

$E(MeV)$	$C_{inc}(\mu C)$	$Q_{d135°}$	$N_{c135°}(Counts/\mu C)$	σ	$Q_{d150°}$	$N_{c150°}(Counts/\mu C)$	σ
1.8	20.2	6	**0.30**	0.12	36	**1.78**	0.30
1.9	20	8	**0.40**	0.14	41	**2.05**	0.32
2	26	5	**0.19**	0.09	62	**2.38**	0.30
2.1	20	7	**0.35**	0.13	57	**2.85**	0.38
2.2	20	8	**0.40**	0.14	61	**3.05**	0.39
2.3	20	6	**0.30**	0.12	46	**2.30**	0.34
2.4	20	11	**0.55**	0.17	59	**2.95**	0.38
2.5	20	9	**0.45**	0.15	68	**3.40**	0.41
2.6	20	10	**0.50**	0.16	94	**4.70**	0.48
2.7	20	9	**0.45**	0.15	85	**4.25**	0.46
2.8	20	7	**0.35**	0.13	76	**3.80**	0.44

Table 4.20: Number of counts taken from a spectra of $^{10}B(d, \alpha_1)^8Be$ reaction both at 135 and 150° respectively.

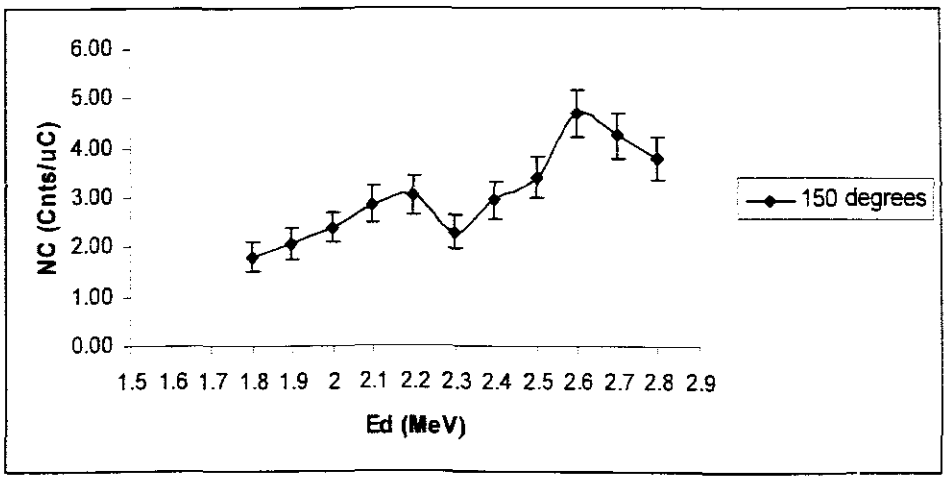

Figure 4.22: Experimental plot of counts vs. incident beam energy for the $^{10}B(d, \alpha_1)^8Be$ measurements taken at 150°.

$E(MeV)$	$C_{inc}(\mu C)$	Q_{d135^o}	$N_{c135^o}(Counts/\mu C)$	σ	Q_{d150^o}	$N_{c150^o}(Counts/\mu C)$	σ
1.8	20.2	25	**1.24**	0.25	158	**7.82**	0.62
1.9	20	22	**1.10**	0.23	214	**10.70**	0.73
2	26	30	**1.15**	0.21	210	**8.08**	0.56
2.1	20	28	**1.40**	0.26	256	**12.80**	0.80
2.2	20	30	**1.50**	0.27	215	**10.75**	0.73
2.3	20	19	**0.95**	0.22	187	**9.35**	0.68
2.4	20	32	**1.60**	0.28	204	**10.20**	0.71
2.5	20	41	**2.05**	0.32	220	**11.00**	0.74
2.6	20	40	**2.00**	0.32	276	**13.80**	0.83
2.7	20	45	**2.25**	0.34	232	**11.60**	0.76
2.8	20	32	**1.60**	0.28	265	**13.25**	0.81

Table 4.21: Number of counts taken from a spectra of $^{10}B(d, a_2)^8Be$ reaction collected at 135 and 150°.

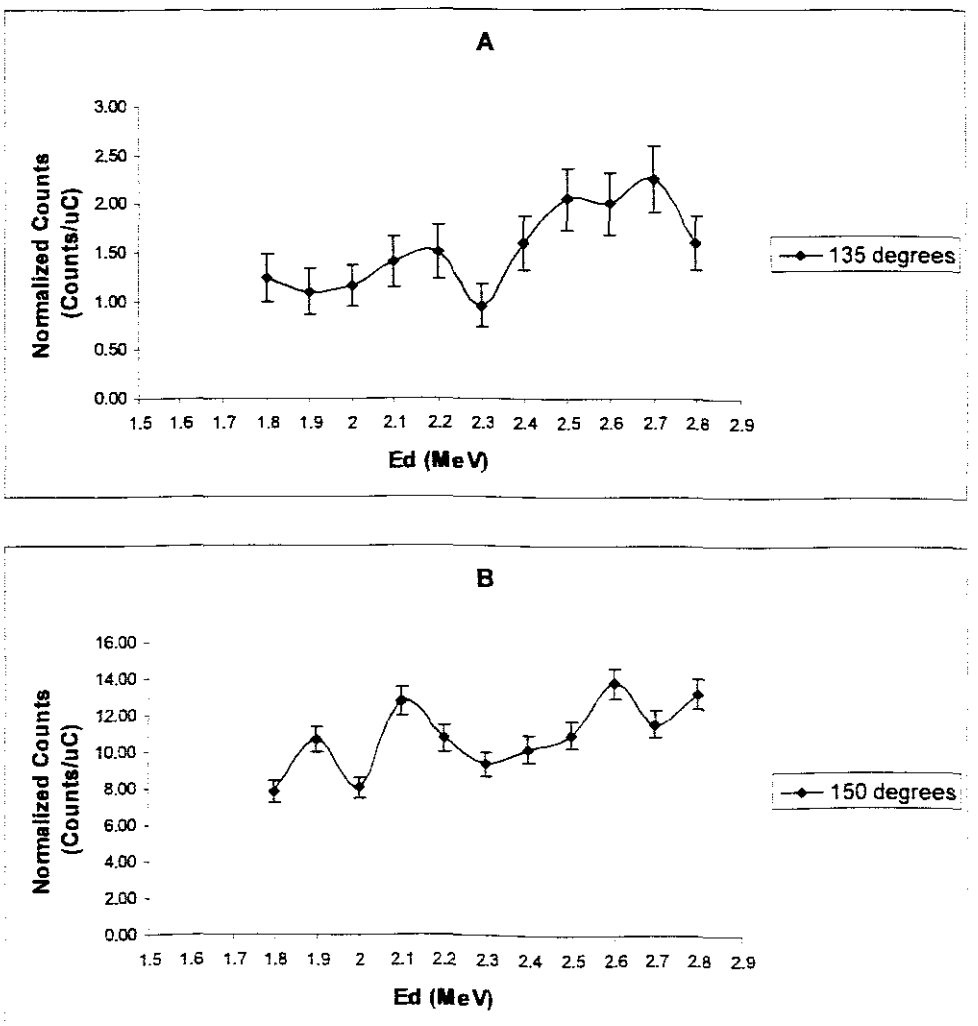

Figure 4.23: Experimental plots of counts vs. incident beam energy for the $^{10}B(d, \alpha_2)^8OBe$ measurements taken at 135 and 150° respectively.

$E(MeV)$	$C_{inc}(\mu C)$	Q_{d135°	$N_{c135^\circ}(Counts/\mu C)$	σ	Q_{d150°	$N_{c150^\circ}(Counts/\mu C)$	σ
1.8	20.2	324	**16.04**	0.89	1078	**53.37**	1.63
1.9	20	307	**15.35**	0.88	1193	**59.65**	1.73
2	26	370	**14.23**	0.74	1794	**69.00**	1.63
2.1	20	330	**16.50**	0.91	2156	**107.80**	2.32
2.2	20	361	**18.05**	0.95	1986	**99.30**	2.23
2.3	20	325	**16.25**	0.90	2891	**144.55**	2.69
2.4	20	439	**21.95**	1.05	2015	**100.75**	2.24
2.5	20	971	**48.55**	1.56	2249	**112.45**	2.37
2.6	20	962	**48.10**	1.55	3572	**178.60**	2.99
2.7	20	884	**44.20**	1.49	3913	**195.65**	3.13
2.8	20	866	**43.30**	1.47	3426	**171.30**	2.93

Table 4.22: Number of counts taken from spectra of $^{10}B(d,\alpha_3)^8Be$ reaction at 135 and 150° .

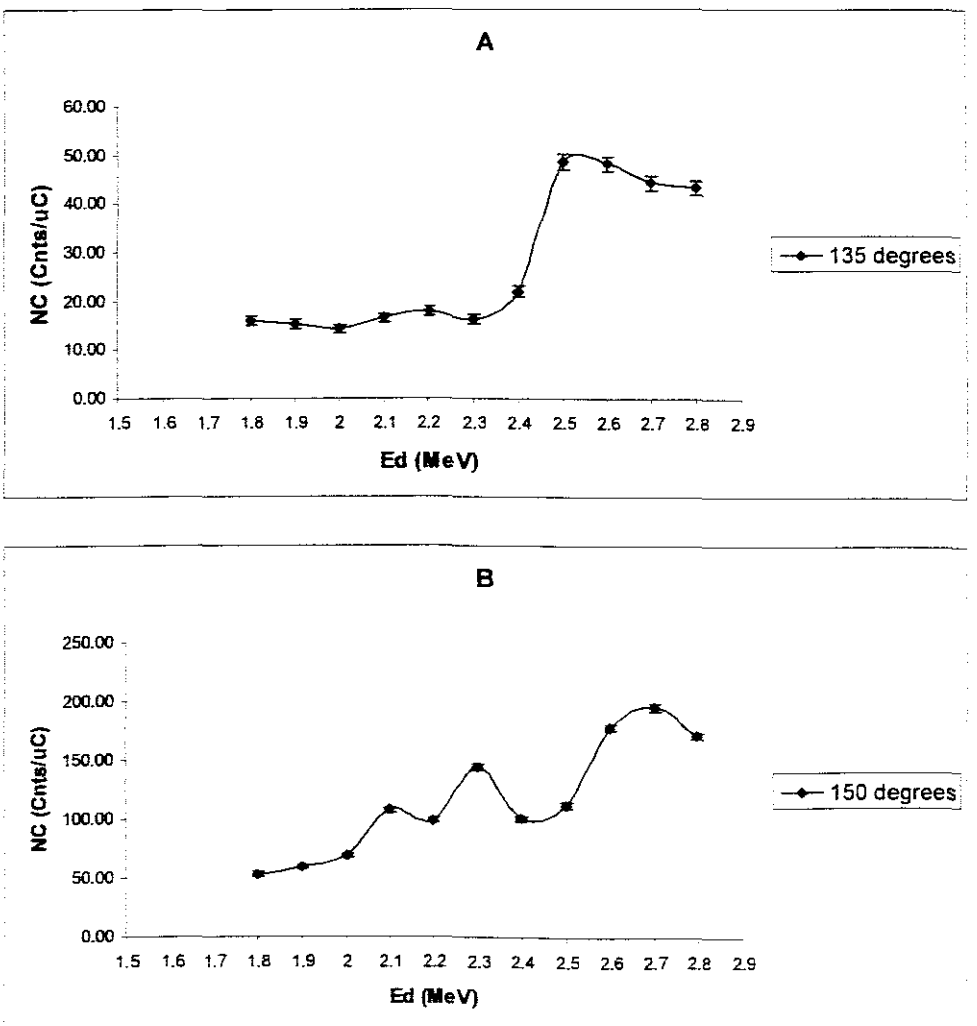

Figure 4.24: Experimental plots of counts vs. incident beam energy for the $^{10}B(d,\alpha_3)^8Be$ measurements taken at 135 and 150° respectively .

$^{16}O(d, p_0)^{17}O$

The 150° results for this reaction's measurements followed the trends of the trends of the Debras et al. data calculated at 135° but the ones for 135° never followed these trends. The normalization factor used to normalize the experimental data to Debras et al. data was very small here about 100 times the one used for this reaction under carbon foil measurements [Deb77]. This is due to the larger amount of oxygen in the boric acid compared to the one on the carbon foil surface. The data and plots for these measurements are presented in Table 4.23 and Fig. 4.25.

$^{16}O(d, p_1)^{17}O$

None of the plots of these measurements followed the trends of the Debras et al. data or the carbon foil data [Deb77], the experimental errors or the piling up of peaks, which was seen in the spectra of boric acid, must have caused this. The data and plots for these measurements are in Table 4.24 and Fig. 4.26.

$E(MeV)$	$C_{inc}(\mu C)$	$Q_{d135°}$	$N_{c135°}(Counts/\mu C)$	σ	$Q_{d150°}$	$N_{c150°}(Counts/\mu C)$	σ
1.8	20.2	38	**1.88**	0.31	705	**34.90**	1.31
1.9	20	31	**1.55**	0.28	1073	**53.65**	1.64
2	26	27	**1.04**	0.20	1671	**64.27**	1.57
2.1	20	54	**2.70**	0.37	1580	**79.00**	1.99
2.2	20	135	**6.75**	0.58	1748	**87.40**	2.09
2.3	20	61	**3.05**	0.39	1581	**79.05**	1.99
2.4	20	62	**3.10**	0.39	1750	**87.50**	2.09
2.5	20	61	**3.05**	0.39	1477	**73.85**	1.92
2.6	20	60	**3.00**	0.39	3178	**158.90**	2.82
2.7	20	59	**2.95**	0.38	2914	**145.70**	2.70
2.8	20	61	**3.05**	0.39	2889	**144.45**	2.69

Table 4.23: Number of counts taken from spectra of $^{16}O(d,p_0)^{17}O$ reaction at 135 and 150°.

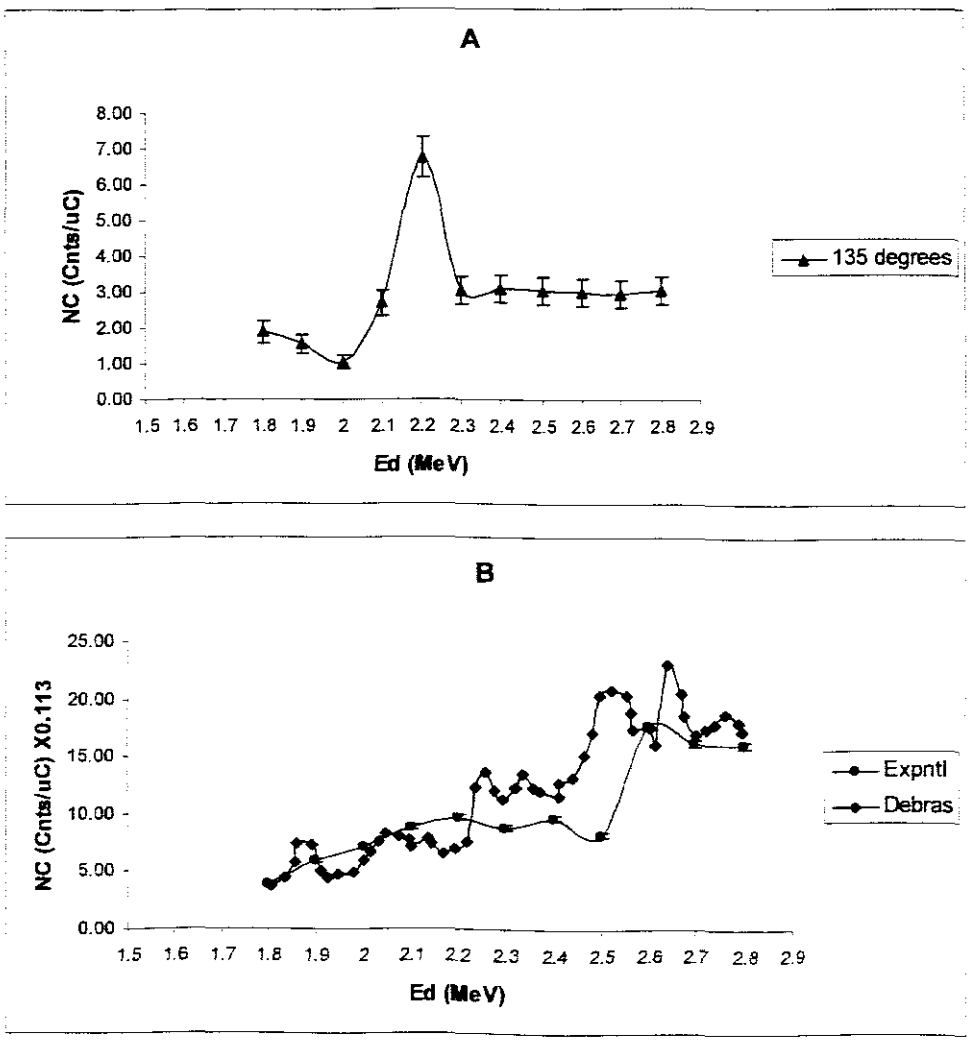

Figure 4.25: In A, a 135° experimental plot of counts vs. incident beam energy for the $^{16}O(d, p_0)^{17}O$, in B is a 150° experimental plot normalized to the 135° Debras et al. data at 2.6 MeV [Deb77].

$E(MeV)$	$C_{inc}(\mu C)$	Q_{d135^o}	$N_{c135^o}(Counts/\mu C)$	σ	Q_{d150^o}	$N_{c150^o}(Counts/\mu C)$	σ
1.8	20.2	185	**9.16**	0.67	2002	**99.11**	0.22
1.9	20	192	**9.60**	0.69	912	**45.60**	0.15
2	26	215	**8.27**	0.56	2423	**93.19**	0.19
2.1	20	216	**10.80**	0.73	1344	**67.20**	0.18
2.2	20	214	**10.70**	0.73	1348	**67.40**	0.18
2.3	20	218	**10.90**	0.74	1673	**83.65**	0.20
2.4	20	223	**11.15**	0.75	1489	**74.45**	0.19
2.5	20	265	**13.25**	0.81	1670	**83.50**	0.20
2.6	20	240	**12.00**	0.77	2819	**140.95**	0.27
2.7	20	327	**16.35**	0.90	1991	**99.55**	0.22
2.8	20	321	**16.05**	0.90	2619	**130.95**	0.26

Table 4.24: Number of counts taken from spectra of $^{16}O(d, p_1)^{17}O$ reaction at 135° and 150°.

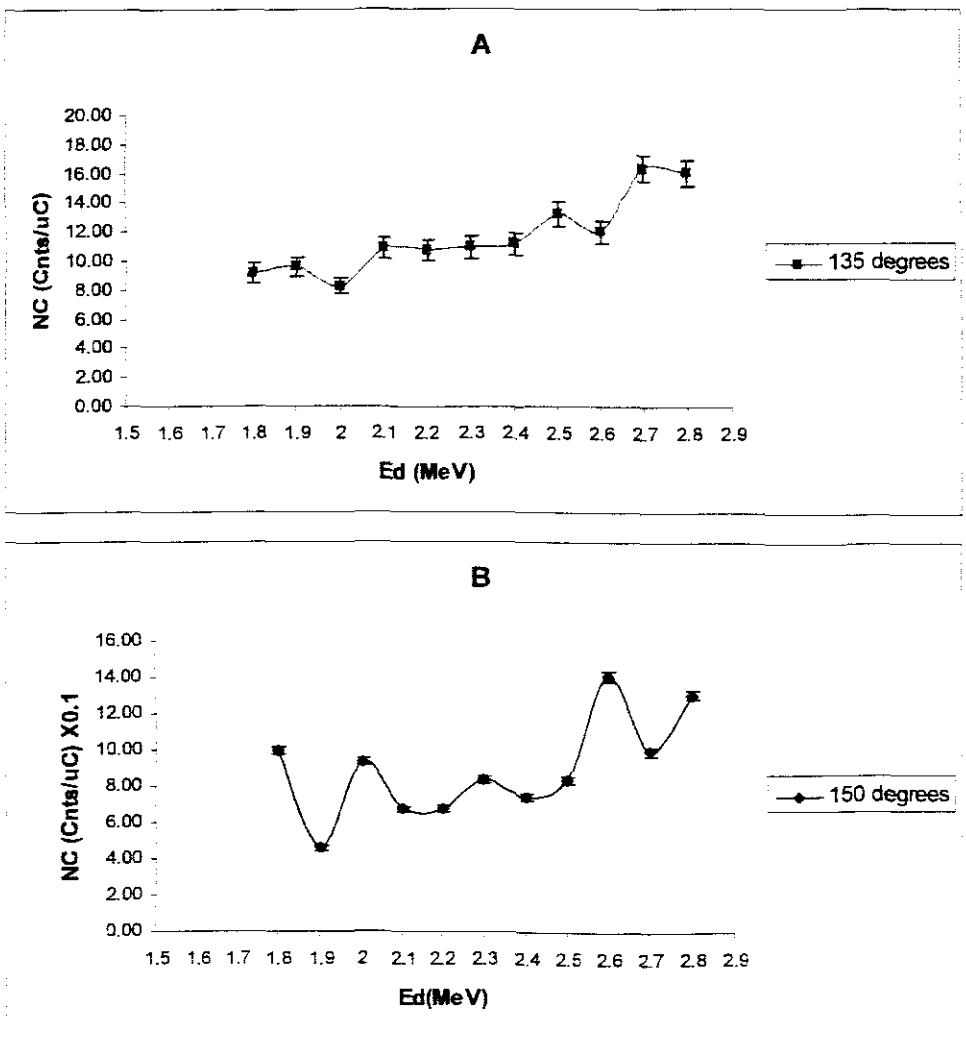

Figure 4.26: Experimental plots of counts vs. incident beam energy for the $^{16}O(d, p_1)^{17}O$ for the 135° and 150° respectively.

$^{18}O(d, \alpha_1)^{16}N$

The peak due to the emitted alpha particles in this reaction could not be found for the 135° measurements so in Table 4.25 and Fig. 4.27 only the number of counts taken from the 150° measurements could be presented. The plot for this measurement could also be not compared to any literature data, due to the lack of cross sections data in the literature.

$^{18}O(d, \alpha_2)^{16}N$

The plots for the results at 135° and 150° showed a little bit of consistence by following the same trends, with the 135° having a poor quality statistics. These plots were not compared to any literature data, the plots are shown in Fig. 4.28 with their data in Table 4.26.

$E(MeV)$	$C_{inc}(\mu C)$	Q_{d135^o}	$N_{c135^o}(Counts/\mu C)$	σ	Q_{d150^o}	$N_{c150^o}(Counts/\mu C)$	σ
1.8	20.2	26	**1.29**	0.25	152	**7.52**	0.61
1.9	20	16	**0.80**	0.20	146	**7.30**	0.60
2	26	30	**1.15**	0.21	165	**6.35**	0.49
2.1	20	37	**1.85**	0.30	239	**11.95**	0.77
2.2	20	28	**1.40**	0.26	180	**9.00**	0.67
2.3	20	22	**1.10**	0.23	143	**7.15**	0.60
2.4	20	31	**1.55**	0.28	190	**9.50**	0.69
2.5	20	34	**1.70**	0.29	228	**11.40**	0.75
2.6	20	42	**2.10**	0.32	333	**16.65**	0.91
2.7	20	51	**2.55**	0.36	272	**13.60**	0.82
2.8	20	34	**1.70**	0.29	259	**12.95**	0.80

Table 4.25: Data collected for the measurements of the $^{18}O(d, \alpha_1)^{16}N$ at 135° and 150°.

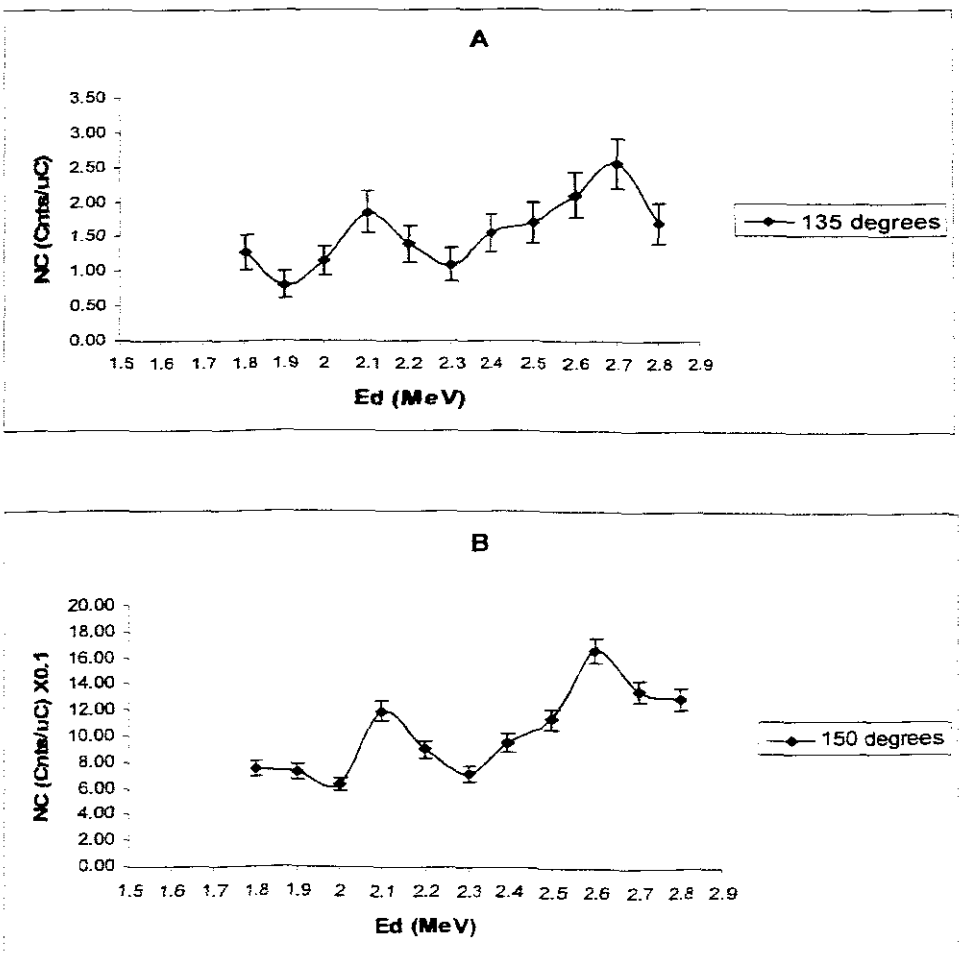

Figure 4.27: Plots of counts vs. beam energy for the $^{18}O(d, \alpha_1)^{16}N$ measurements taken at 135° and 150° respectively.

$E(MeV)$	$C_{inc}(\mu C)$	Q_{d135°	$N_{c135^\circ}(Counts/\mu C)$	σ	Q_{d150°	$N_{c150^\circ}(Counts/\mu C)$	σ
1.8	20.2	18	**0.89**	0.25	121	**5.99**	0.54
1.9	20	25	**1.25**	0.23	142	**7.10**	0.60
2	26	14	**0.54**	0.21	154	**5.92**	0.48
2.1	20	26	**1.30**	0.26	212	**10.60**	0.73
2.2	20	23	**1.15**	0.27	177	**8.85**	0.67
2.3	20	25	**1.25**	0.22	133	**6.65**	0.58
2.4	20	30	**1.50**	0.28	179	**8.95**	0.67
2.5	20	32	**1.60**	0.32	197	**9.85**	0.70
2.6	20	47	**2.35**	0.32	309	**15.45**	0.88
2.7	20	44	**2.20**	0.34	304	**15.20**	0.87
2.8	20	29	**1.45**	0.28	220	**11.00**	0.74

Table 4.26: Data collected for the measurements of the $^{18}O(d, \alpha_3)^{16}N$ at 135 and 150°.

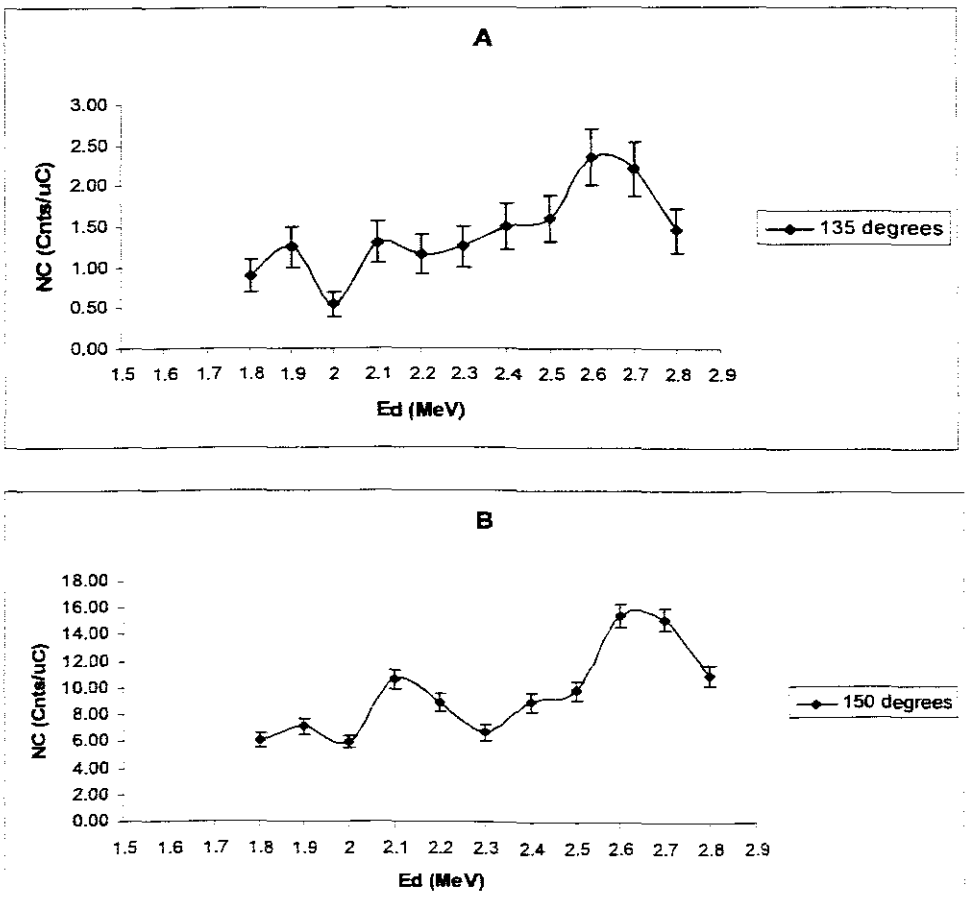

Figure 4.27 Plots of counts vs. beam energy for the $^{18}O(d, \alpha_3)^{16}N$ measurements taken at 135° and 150° respectively.

4.2.5 Results of the $^3He^+$ on boric acid (HBO_3) crystal.

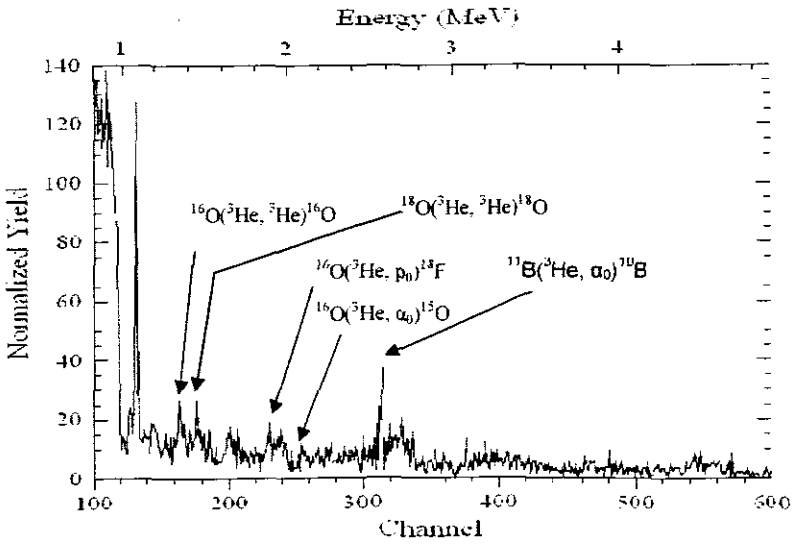

Figure: 4.28: A spectrum collected for $^3He^+$ on boric acid at 2.6 MeV and 150°

$^{11}B(^3He, \alpha_i)^{10}B$

These reactions showed to be very weak at low incident beam energies; their lower residual nuclei states emitted particles could not be detected especially by the 135° detector at the 1.8 – 2.8 MeV incident energy range. However, the reaction showed strength only for i = 0 when its emitted alpha particles were even detected by the 135° detector. Although the emitted alpha particles could be detected but the statistics for these measurements was not very good, and the 135 and 150° plot did not seem following the same trends. This could be caused by experimental errors. The table and plot of the reaction for i = 0 is presented in Table 4.25 and Fig. 4.29.

The data For i = 1 for these reactions is presented in Table 4.28. however no plots were included due to poor statistics.

$E(MeV)$	$C_{inc}(\mu C)$	Q_{d135^o}	$N_{c135^o}(Counts/\mu C)$	σ	Q_{d150^o}	$N_{c150^o}(Counts/\mu C)$	σ
1.8	2				3	**1.50**	0.87
1.9	2				2	**1.00**	0.71
2	2	2	**1.00**	0.71	6	**3.00**	1.22
2.1	2	2	**1.00**	0.71	3	**1.50**	0.87
2.2	2	3	**1.50**	0.87	5	**2.50**	1.12
2.3	2	2	**1.00**	0.71	8	**4.00**	1.41
2.4	2	4	**2.00**	1.00	5	**2.50**	1.12
2.5	2	3	**1.50**	0.87	7	**3.50**	1.32
2.6	2	3	**1.50**	0.87	5	**2.50**	1.12
2.7	2	3	**1.50**	0.87	11	**5.50**	1.66
2.8	2	4	**2.00**	1.00	9	**4.50**	1.50

Table 4.27: Data collected for the $^{11}B(^3He, \alpha_0)^{10}B$ reaction measurements taken at 135° and 150°.

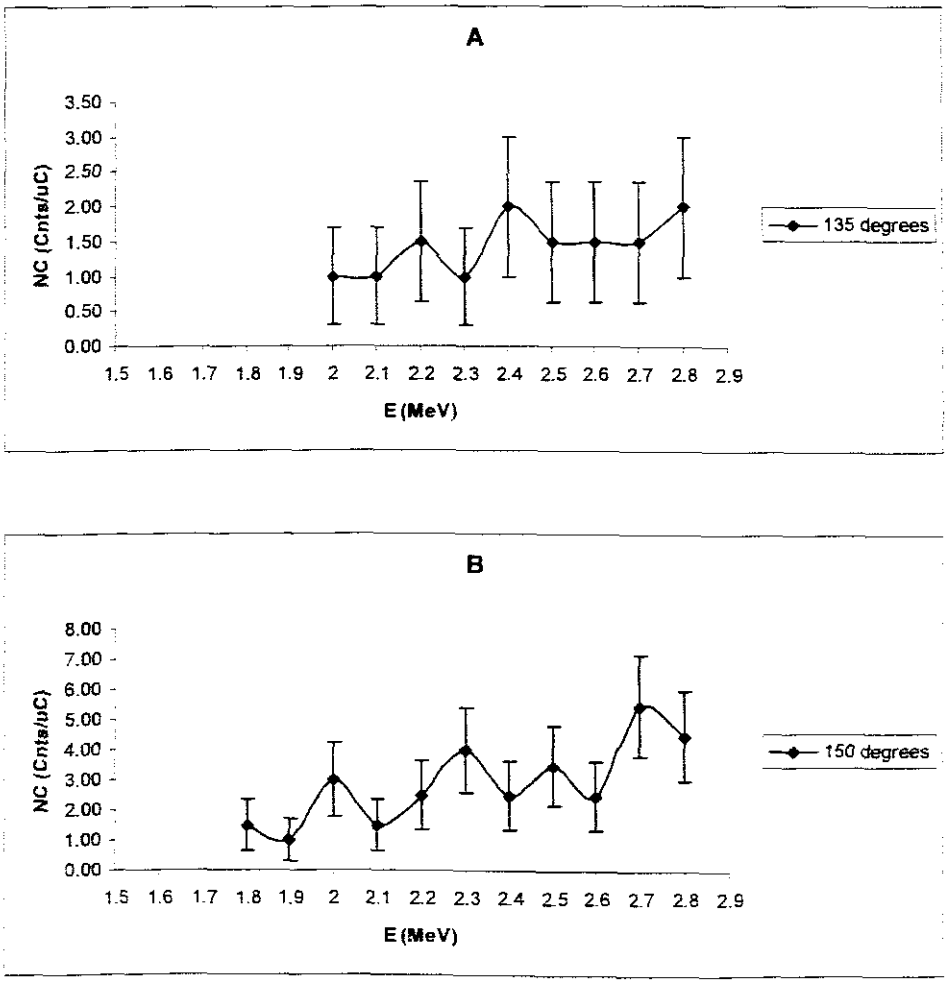

Figure 4.29: Experimental plots of counts vs. incident beam energy for the $^{11}B(3He, \alpha_0)^{10}B$ measurements taken at 135° and 150° respectively.

$E(MeV)$	$C_{inc}(\mu C)$	$Q_{d150^{o}}$	$N_{c150^{o}}(Counts/\mu C)$	σ
1.8	2	2	**1.00**	0.71
1.9	2	1	**0.50**	0.50
2	2	2	**1.00**	0.71
2.1	2	1	**0.50**	0.50
2.2	2	2	**1.00**	0.71
2.3	2	2	**1.00**	0.71
2.4	2	4	**2.00**	1.00
2.5	2	2	**1.00**	0.71
2.6	2	3	**1.50**	0.87
2.7	2	2	**1.00**	0.71
2.8	2	3	**1.50**	0.87

Table 4.28: Data collected for the $^{11}B(^{3}He, \alpha_1)^{10}B$ reaction measurements taken at 150°.

$^{10}B(^{3}He, p_i)^{12}C$

For this reaction no peaks were observed on the spectra for all i's less than 5, which means no protons could be detected. Even for i = 5 the 135° detector could not any emitted protons still. So the results presented in Table 4.29 and Fig. 4.30 are only for the 150° measurements and they gave a very poor statistics at incident energies below 2.3 MeV.

For the $^{10}B(^{3}He, p_6)^{12}C$ reaction at 150°, the results are presented in Table 4.30 and Fig 4.31 and its statistics was a bit better compared to the one for i = 5

$E(MeV)$	$C_{inc.}(\mu C)$	$Q_{d150°}$	$N_{c150°}(Counts/\mu C)$	σ
1.8	2	2	**1.00**	0.71
1.9	2	1	**0.50**	0.50
2	2	3	**1.50**	0.87
2.1	2	2	**1.00**	0.71
2.2	2	1	**0.50**	0.50
2.3	2	2	**1.00**	0.71
2.4	2	4	**2.00**	1.00
2.5	2	9	**4.50**	1.50
2.6	2	21	**10.50**	2.29
2.7	2	16	**8.00**	2.00
2.8	2	9	**4.50**	1.50

Table 4.29: Data collected for the $^{10}B(^{3}He, p_5)^{12}C$ reaction measurements taken at 150°.

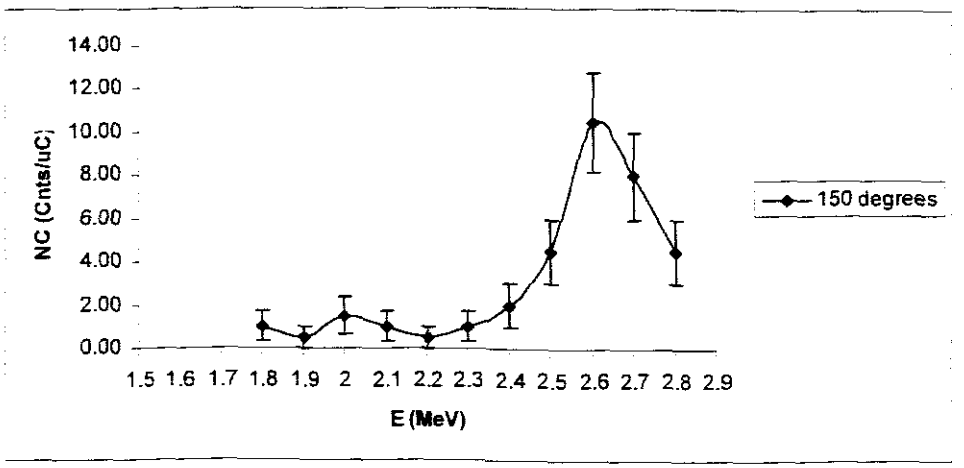

Figure 4.30: Experimental plot of counts vs. incident beam energy for the $^{10}B(^{3}He, p_5)^{12}C$ measurements taken at 150°.

$E(MeV)$	$C_{inc}(\mu C)$	Q_{d150^o}	$N_{c150^o}(Counts/\mu C)$	σ
1.8	2	3	**1.50**	0.87
1.9	2	2	**1.00**	0.71
2	2	2	**1.00**	0.71
2.1	2	2	**1.00**	0.71
2.2	2	3	**1.50**	0.87
2.3	2	6	**3.00**	1.22
2.4	2	3	**1.50**	0.87
2.5	2	5	**2.50**	1.12
2.6	2	3	**1.50**	0.87
2.7	2	13	**6.50**	1.80
2.8	2	10	**5.00**	1.58

Table 4.30: Data collected for the $^{10}B(^3He, p_0)^{12}C$ reaction measurements taken at 150°.

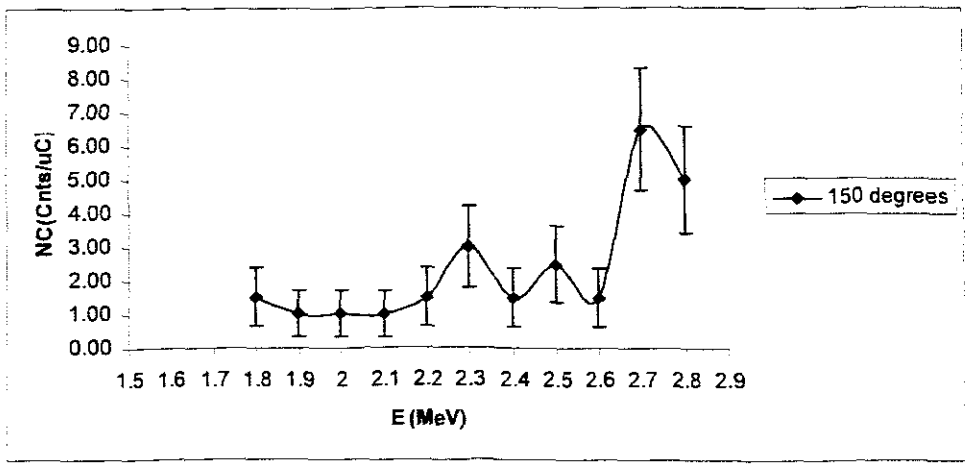

Figure 4.31: Experimental plot of counts vs. incident beam energy for the $^{10}B(^3He, p_0)^{12}B$ measurements taken at 150°.

$^{11}B(^{3}He, d_i)^{12}C$

This reaction's emitted deuterons could only be detected by the 150° detector at $i = 2$ and 3. This is presented in Table 4.31 and Fig. 4.32; this is the only reaction that showed a better statistics in the helium three induced reactions on boron targets. However, since there was no literature data for this reaction it could not be compared to see if it followed the expected trends. For i= 3 the data is presented in Table 4.32 and Fig. 4.33

$E(MeV)$	$C_{inc}(\mu C)$	$Q_{d150°}$	$N_{c150°}(Counts/\mu C)$	σ
1.8	2	3	**1.50**	0.87
1.9	2	4	**2.00**	1.00
2	2	7	**3.50**	1.32
2.1	2	4	**2.00**	1.00
2.2	2	3	**1.50**	0.87
2.3	2	5	**2.50**	1.12
2.4	2	3	**1.50**	0.87
2.5	2	10	**5.00**	1.58
2.6	2	5	**2.50**	1.12
2.7	2	10	**5.00**	1.58
2.8	2	5	**2.50**	1.12

Table 4.31: Data collected for the $^{11}B(^{3}He, d_2)^{12}C$ reaction measurements taken at 150°.

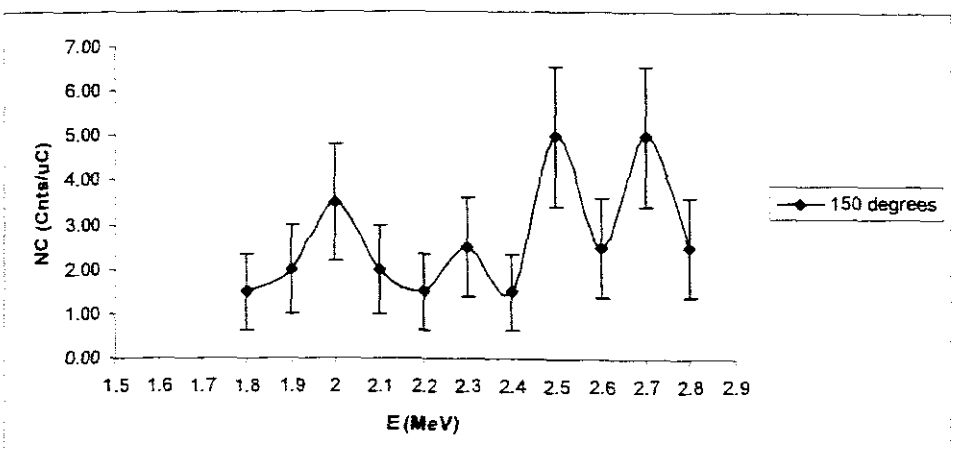

Figure 4.32: Experimental plot of counts vs. incident beam energy for the $^{11}B(^{3}He, d_2)^{12}C$ measurements taken at 150°.

$E(MeV)$	$C_{inc}(\mu C)$	Q_{d150^o}	$N_{c150^o}(Counts/\mu C)$	σ
1.8	2	5	**2.50**	1.12
1.9	2	4	**2.00**	1.00
2	2	3	**1.50**	0.87
2.1	2	2	**1.00**	0.71
2.2	2	5	**2.50**	1.12
2.3	2	9	**4.50**	1.50
2.4	2	10	**5.00**	1.58
2.5	2	14	**7.00**	1.87
2.6	2	12	**6.00**	1.73
2.7	2	7	**3.50**	1.32
2.8	2	19	**9.50**	2.18

Table 4.32: Data collected for the $^{11}B(^3He, d_3)^{12}C$ reaction measurements taken at 150°.

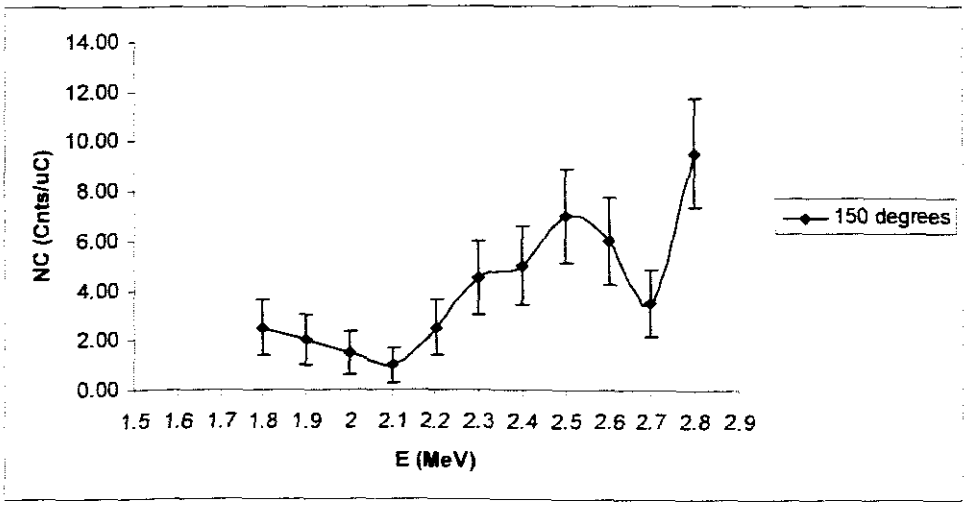

Figure 4.33: Experimental plot of counts vs. incident beam energy for the $^{11}B(^3He, d_3)^{12}C$ measurements taken at 150°.

4.2.6 Results of the D^+ on Boron carbide ($B4C/SiO_2$).

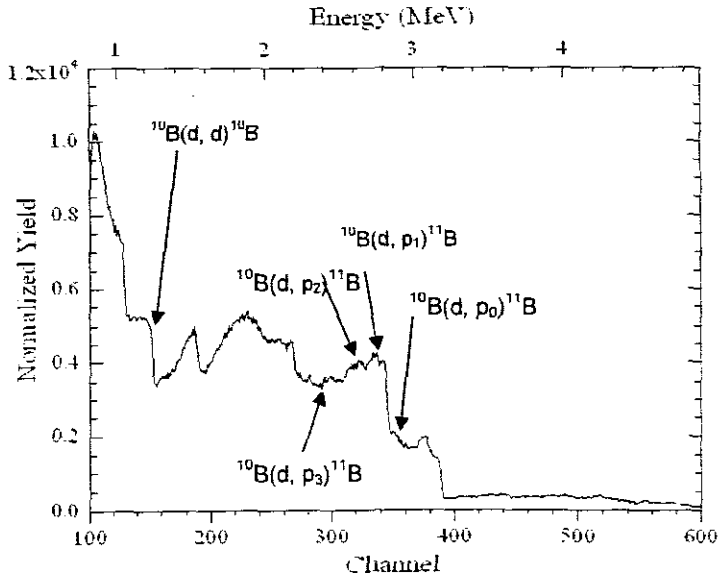

Figure 4.34: A spectrum collected for deuterons on B_4C/SiO_2 at 2.6 MeV.

$^{10}B(d, p_i)^{11}B$

These reactions for i = 0 to 4 are presented in tables 4.33 to 4.37 and figures 4.35 to 4.39.

For *i* = 0, the results never looked the way they were expected to be since the measurements for the same reaction had been taken for the boric acid target, however the results showed to follow the same trends with some deviations at some points which are suspected to be due to experimental errors. For both targets, the measurements at 135° gave a very poor statistics then the 135° measurements were not included but they do appear in Table 4.33. The plot for these results is presented in Fig. 4.35 as well.

For i = 1, again a very poor quality statistics for the 135° was observed in a way that these results could not be plotted, however, the data is included in Table 4.34. The results gotten using the boric acid and boron carbide targets varied with bigger margins at 2.8 MeV. Fig. 4.36 presents the plot of the 150° measurements.

In the i = 2 measurements, the 150° boron carbide measurements seemed more following the 135° boric acid measurements trend than the 150°, where as the 150° boron carbide plot never followed the trends. The data and plots are presented in Table 4.35 and Fig. 4.37.

For i = 3, both the 135 and 150° measurements gave a better statistics with the 135° boron carbide measurements deviating from the boric acid measurements at 2.1 and 2.6 MeV. The data for these measurements is presented in Table 4.36 and Fig. 4.38.

For i = 4, the data is presented in Table 4.37. The plots of the results did not show to be in agreement with the ones taken with the boric acid target. The plot for 135° in Fig. 4.39 A would have been expected to start from the low numbers of counts increase then reach its maximum number of detected counts at 2.4 MeV like so did the one for the boric acid measurements. Instead of following this trend the plot had its maximum number of detected counts at 2.8 MeV. The 150° measurements plot happened to be an opposite of the 150° boric acid measurements, having its maximum at 1.8 MeV while for boric acid it was found at 2.8 MeV. This must have been caused by experimental errors.

$E(MeV)$	$C_{inc}(\mu C)$	Q_{d135^o}	$N_{c135^o}(Counts/\mu C)$	σ	Q_{d150^o}	$N_{c150^o}(Counts/\mu C)$	σ
1.8	20	12	**0.60**	0.77	38	**1.90**	0.31
1.9	20	13	**0.65**	0.81	31	**1.55**	0.28
2	20	11	**0.55**	0.74	39	**1.95**	0.31
2.1	20	6	**0.30**	0.55	37	**1.85**	0.30
2.2	20.2	13	**0.64**	0.80	49	**2.43**	0.35
2.3	20	15	**0.75**	0.87	42	**2.10**	0.32
2.4	20	12	**0.60**	0.77	48	**2.40**	0.35
2.5	20	10	**0.50**	0.71	73	**3.65**	0.43
2.6	20	17	**0.85**	0.92	68	**3.40**	0.41
2.7	20	9	**0.45**	0.67	65	**3.25**	0.40
2.8	25.2	10	**0.40**	0.63	70	**2.78**	0.33

Table 4.33: Data collected for the $^{10}B(d, p_0)^{11}B$ reaction measurements taken at 135° and 150°.

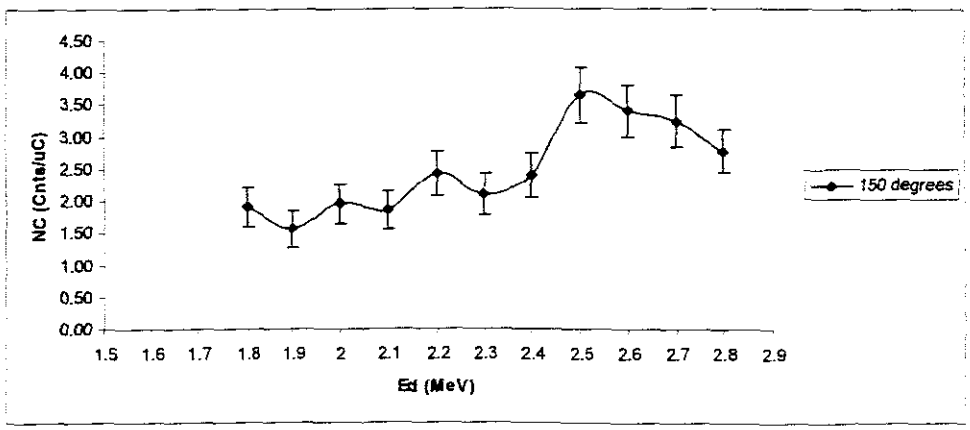

Figure 4.35: Experimental plot of counts vs. incident beam energy for the $^{10}B(d, p_0)^{11}B$ measurements taken at 150°.

$E(MeV)$	$C_{inc}(\mu C)$	Q_{d135^o}	$N_{c135^o}(Counts/\mu C)$	σ	Q_{d150^o}	$N_{c150^o}(Counts/\mu C)$	σ
1.8	20	9	**0.45**	0.15	32	**1.60**	0.28
1.9	20	11	**0.55**	0.17	27	**1.35**	0.26
2	20	12	**0.60**	0.17	38	**1.90**	0.31
2.1	20	38	**1.90**	0.31	50	**2.50**	0.35
2.2	20.2	9	**0.45**	0.15	57	**2.82**	0.37
2.3	20	22	**1.10**	0.23	59	**2.95**	0.38
2.4	20	17	**0.85**	0.21	67	**3.35**	0.41
2.5	20	40	**2.00**	0.32	58	**2.90**	0.38
2.6	20	38	**1.90**	0.31	78	**3.90**	0.44
2.7	20	19	**0.95**	0.22	88	**4.40**	0.47
2.8	25.2	16	**0.63**	0.16	125	**4.96**	0.44

Table 4.34: Data collected for the $^{10}B(d, p_1)^{11}B$ reaction measurements taken at 135° and 150°.

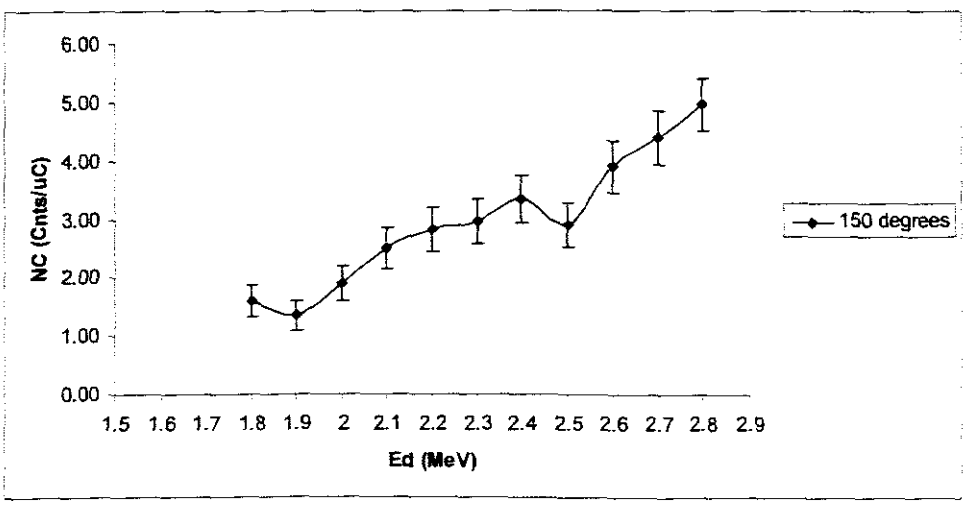

Figure 4.36: Experimental plot of counts vs. incident beam energy for the $^{10}B(d, p_1)^{11}B$ measurements taken at 150°.

$E(MeV)$	$C_{inc}(\mu C)$	$Q_{d135°}$	$N_{c135°}(Counts/\mu C)$	σ	$Q_{d150°}$	$N_{c150°}(Counts/\mu C)$	σ
1.8	20	17	**0.85**	0.21	123	**6.15**	0.55
1.9	20	26	**1.30**	0.25	153	**7.65**	0.62
2	20	20	**1.00**	0.22	177	**8.85**	0.67
2.1	20	21	**1.05**	0.23	206	**10.30**	0.72
2.2	20.2	25	**1.24**	0.25	219	**10.84**	0.73
2.3	20	30	**1.50**	0.27	223	**11.15**	0.75
2.4	20	39	**1.95**	0.31	261	**13.05**	0.81
2.5	20	50	**2.50**	0.35	272	**13.60**	0.82
2.6	20	48	**2.40**	0.35	280	**14.00**	0.84
2.7	20	50	**2.50**	0.35	299	**14.95**	0.86
2.8	25.2	26	**1.03**	0.20	522	**20.71**	0.91

Table 4.35: Data collected for the $^{10}B(d, p_2)^{11}B$ reaction measurements taken at 135° and 150°.

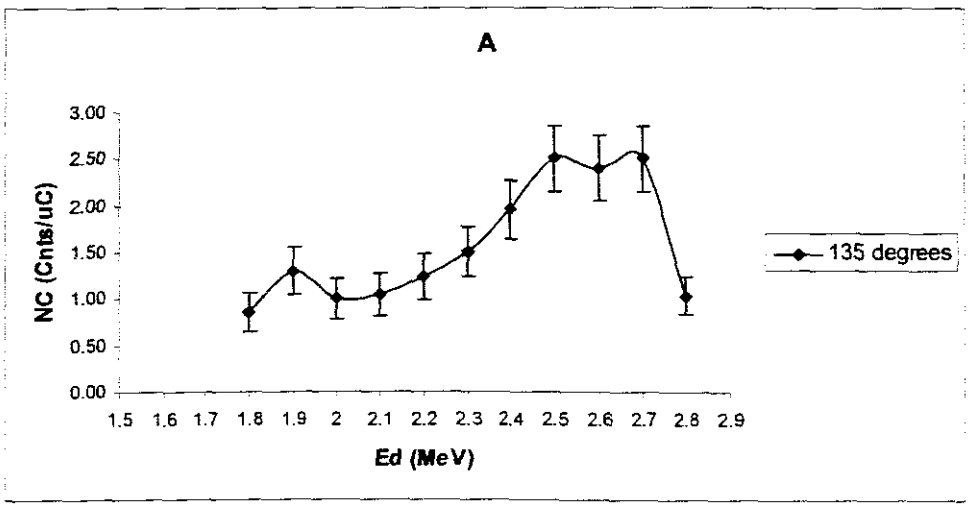

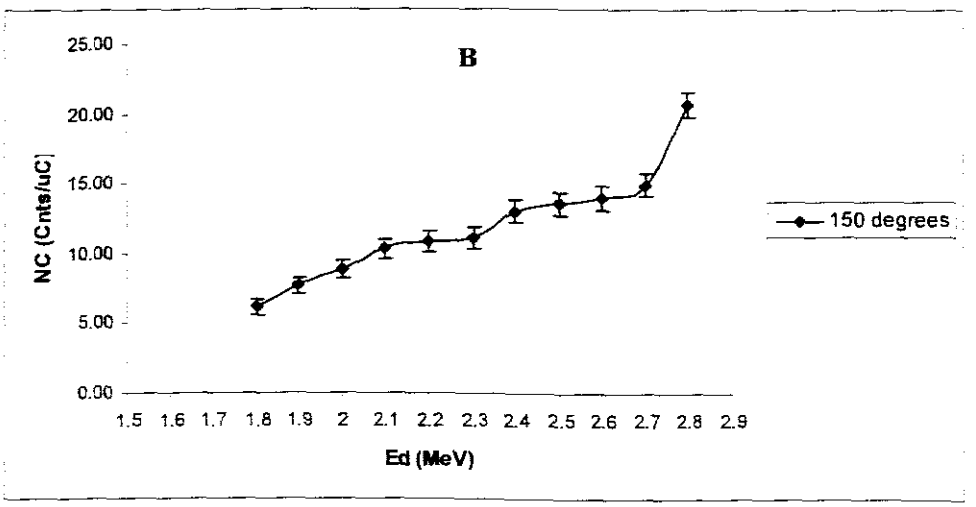

$E(MeV)$	$C_{inc}(\mu C)$	Q_{d135^o}	$N_{c135^o}(Counts/\mu C)$	σ	Q_{d150^o}	$N_{c150^o}(Counts/\mu C)$	σ
1.8	20	20	**1.00**	0.22	109	**5.45**	0.52
1.9	20	35	**1.75**	0.30	134	**6.70**	0.58
2	20	40	**2.00**	0.32	148	**7.40**	0.61
2.1	20	30	**1.50**	0.27	185	**9.25**	0.68
2.2	20.2	38	**1.88**	0.31	209	**10.35**	0.72
2.3	20	48	**2.40**	0.35	205	**10.25**	0.72
2.4	20	45	**2.25**	0.34	218	**10.90**	0.74
2.5	20	60	**3.00**	0.39	272	**13.60**	0.82
2.6	20	45	**2.25**	0.34	305	**15.25**	0.87
2.7	20	59	**2.95**	0.38	354	**17.70**	0.94
2.8	25.2	78	**3.10**	0.35	521	**20.67**	0.91

Table 4.36: Data collected for the $^{10}B(d, p_3)^{11}B$ reaction measurements taken at 135° and 150°.

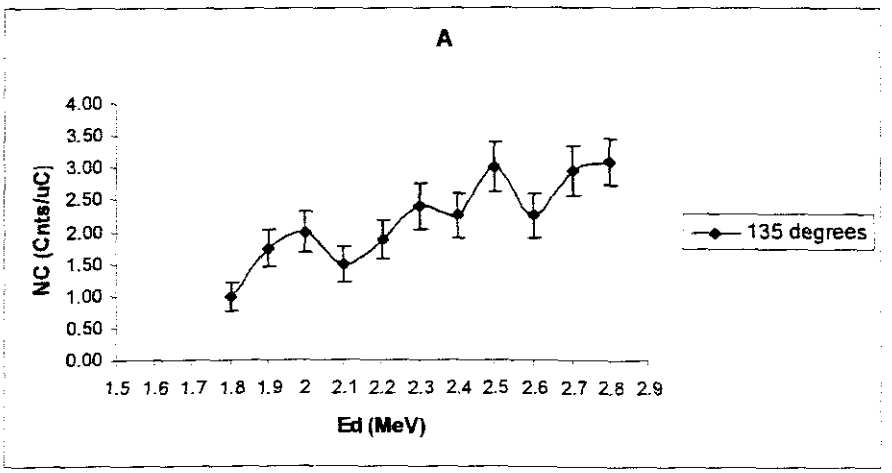

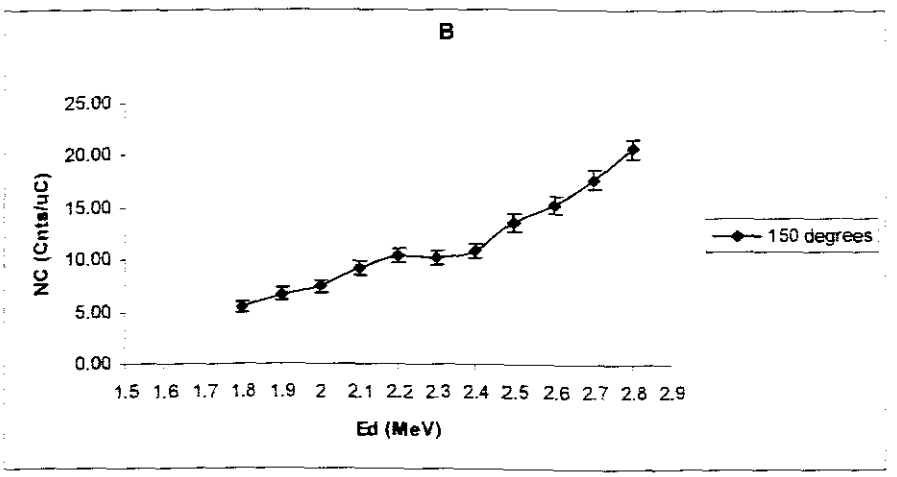

B

Figure 4.38: Experimental plot of counts vs. incident beam energy for the $^{10}B(d, p_3)^{11}B$ measurements taken at 135° and 150° respectively.

$E(MeV)$	$C_{inc}(\mu C)$	Q_{d135^o}	$N_{c135^o}(Counts/\mu C)$	σ	Q_{d150^o}	$N_{c150^o}(Counts/\mu C)$	σ
1.8	20	551	**27.55**	1.17	5116	**255.80**	3.58
1.9	20	369	**18.45**	0.96	5006	**250.30**	3.54
2	20	498	**24.90**	1.12	3300	**165.00**	2.87
2.1	20	433	**21.65**	1.04	2957	**147.85**	2.72
2.2	20.2	386	**19.11**	0.97	2572	**127.33**	2.51
2.3	20	517	**25.85**	1.14	2728	**136.40**	2.61
2.4	20	418	**20.90**	1.02	2687	**134.35**	2.59
2.5	20	473	**23.65**	1.09	2894	**144.70**	2.69
2.6	20	566	**28.30**	1.19	3281	**164.05**	2.86
2.7	20	578	**28.90**	1.20	3253	**162.65**	2.85
2.8	25.2	728	**28.89**	1.07	4425	**175.60**	2.64

Table 4.37: Data collected for the $^{10}B(d, p_4)^{11}B$ reaction measurements taken at 135° and 150°.

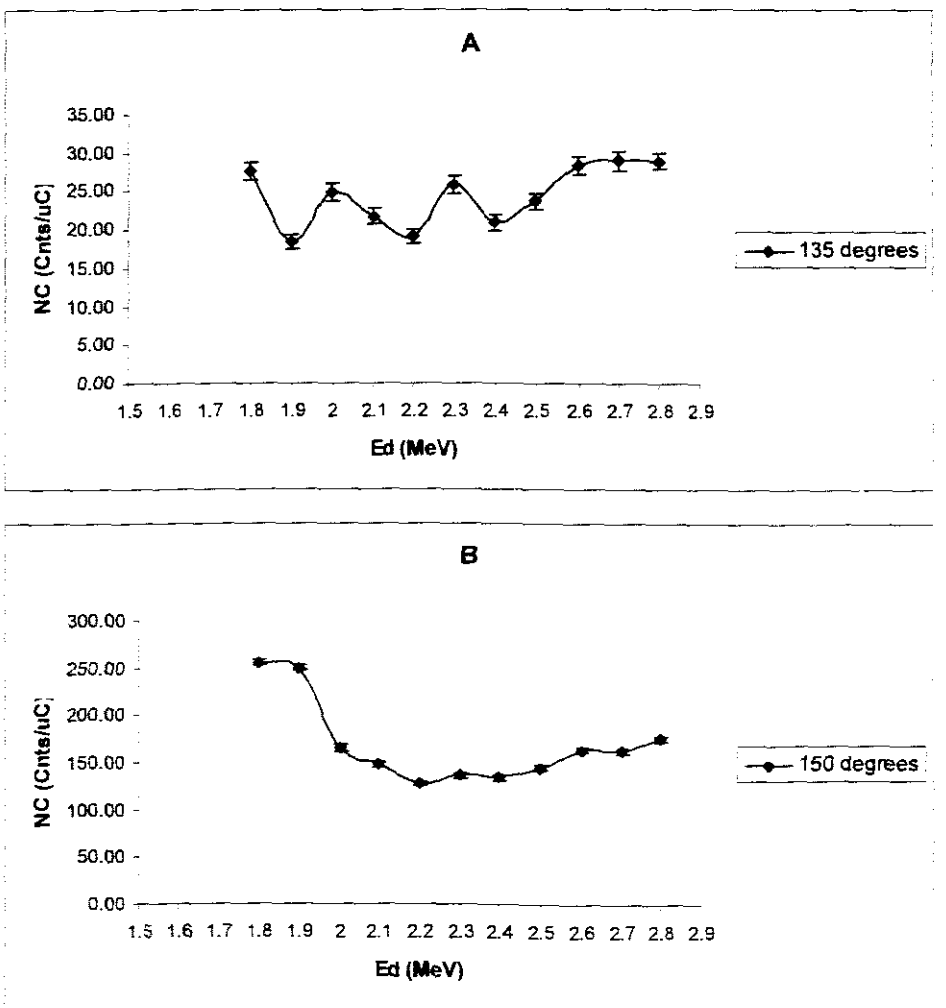

Figure 4.39: Experimental plot of counts vs. incident beam energy for the $^{10}B(d, p_4)^{11}B$ measurements taken at 135° and 150° respectively.

$^{11}B(d, p_0)^{12}B$

The results presented in Table 4.38 and Fig. 4.40 showed to follow the same trends, both 135 and 150° they resembled the plot of 150° boric acid measurements with only one deviation at 2.5 MeV.

$E(MeV)$	$C_{inc}(\mu C)$	$Q_{d135°}$	$N_{c135°}(Counts/\mu C)$	σ	$Q_{d150°}$	$N_{c150°}(Counts/\mu C)$	σ
1.8	20	191	**9.55**	0.69	928	**46.40**	1.52
1.9	20	210	**10.50**	0.72	890	**44.50**	1.49
2	20	195	**9.75**	0.70	1262	**63.10**	1.78
2.1	20	594	**29.70**	1.22	2212	**110.60**	2.35
2.2	20.2	681	**33.71**	1.29	3119	**154.41**	2.76
2.3	20	646	**32.30**	1.27	3987	**199.35**	3.16
2.4	20	714	**35.70**	1.34	3589	**179.45**	3.00
2.5	20	672	**33.60**	1.30	4122	**206.10**	3.21
2.6	20	639	**31.95**	1.26	4472	**223.60**	3.34
2.7	20	546	**27.30**	1.17	4010	**200.50**	3.17
2.8	25.2	713	**28.29**	1.06	4854	**192.62**	2.76

Table 4.38: Data collected for the $^{11}B(d, p_0)^{12}B$ reaction measurements taken at 135° and 150°.

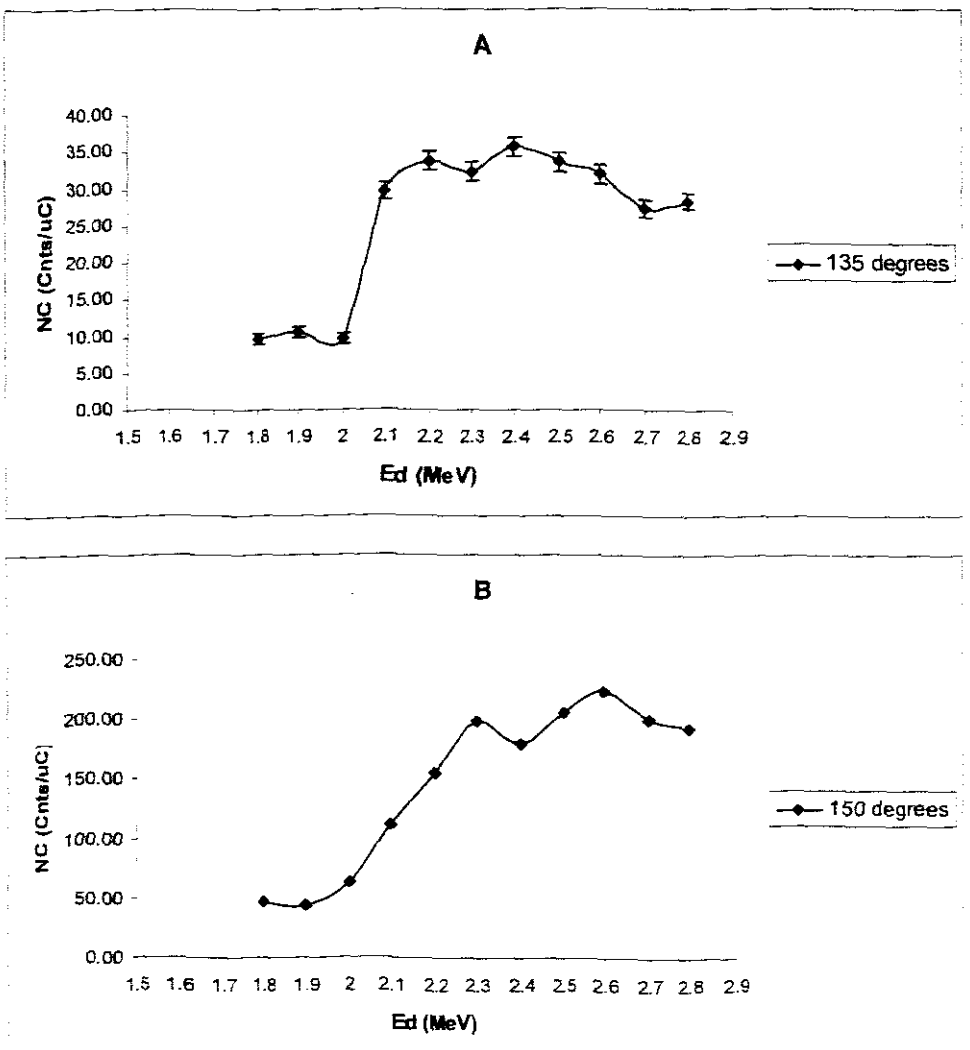

Figure 4.40: Experimental plot of counts vs. incident beam energy for the $^{11}B(d, p_0)^{12}B$ measurements taken at 135° and 150°.

$^{10}B(d, a_0)^8Be$

All the plots of this reaction results had a statistics of poor quality so they were never plotted even the data was neither presented.

$^{10}B(d, a_1)^8Be$

Table 4.39 and Fig. 4.41 presents the data and a plot for this reaction measurements, poor statistics was observed for the 135° measurements so their plots could not be plotted. The 150° plot for these measurements showed to be in agreement with the plot of the 150° boric acid measurements, which increases the level of confidence on these results.

$E(MeV)$	$C_{uc}(\mu C)$	$Q_{d135°}$	$N_{c135°}(Counts/\mu C)$	σ	$Q_{d150°}$	$N_{c150°}(Counts/\mu C)$	σ
1.8	20	5	**0.25**	0.11	25	**1.25**	0.25
1.9	20	10	**0.50**	0.16	28	**1.40**	0.26
2	20	11	**0.55**	0.17	43	**2.15**	0.33
2.1	20	16	**0.80**	0.20	55	**2.75**	0.37
2.2	20.2	13	**0.64**	0.18	61	**3.02**	0.39
2.3	20	16	**0.80**	0.20	40	**2.00**	0.32
2.4	20	17	**0.85**	0.21	49	**2.45**	0.35
2.5	20	20	**1.00**	0.22	55	**2.75**	0.37
2.6	20	8	**0.40**	0.14	69	**3.45**	0.42
2.7	20	10	**0.50**	0.16	68	**3.40**	0.41
2.8	25.2	16	**0.63**	0.16	88	**3.49**	0.37

Table 4.39: Data collected for the $^{10}B(d, a_1)^8Be$ reaction measurements taken at 135 and 150°.

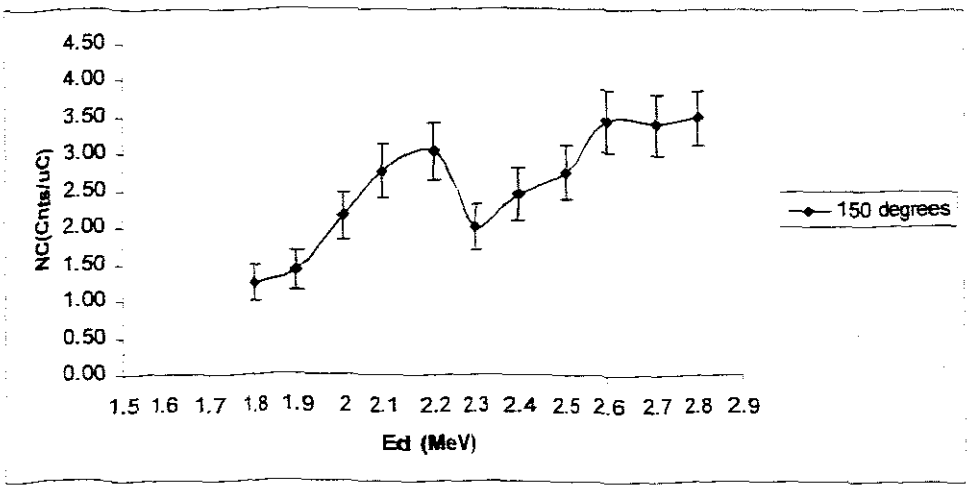

Figure 4.41: Experimental plot of counts vs. incident beam energy for the $^{10}B(d, a_1)^{11}B$ measurements taken at 150°.

$^{12}C(d, p_0)^{13}C$

In Table 4.40 and Fig. 4.42, the 150° results of the measurements of this reaction showed to be good in a way that they were normalized at 2.5 MeV to the Debras et al. literature cross sections data collected at 135° [Deb77]. However, the results never followed trends of the literature plot especially at points between 2.2 and 2.7 MeV, where the experimental plot falls out of error bars.

$^{12}C(d, p_1)^{13}C$

Both the 135° and 150° plot of this reaction did not show any consistence with the results from the carbon foil. The plots behaved awkwardly, however the 135° and the 150° plot followed the trends of one another. Table 4.41 and Fig. 4.43 show data and the plots of these results.

$^{12}C(d, p_2)^{13}C$

Very poor results were observed for this reaction, which had very huge variations from Kokoris et al. [Kok06] cross section data to which they normalized at 1.8 MeV. This is suspected to be caused by the thick target used.These results are presented in Table 4.42 and Fig 4.44.

$E(MeV)$	$C_{inc}(\mu C)$	Q_{d135^o}	$N_{c135^o}(Counts/\mu C)$	σ	Q_{d150^o}	$N_{c150^o}(Counts/\mu C)$	σ
1.8	20	321	**16.05**	0.90	1957	**97.85**	2.21
1.9	20	333	**16.65**	0.91	1842	**92.10**	2.15
2	20	331	**16.55**	0.91	1586	**79.30**	1.99
2.1	20	346	**17.30**	0.93	1619	**80.95**	2.01
2.2	20.2	379	**18.76**	0.96	2043	**101.14**	2.24
2.3	20	352	**17.60**	0.94	1987	**99.35**	2.23
2.4	20	508	**25.40**	1.13	2088	**104.40**	2.28
2.5	20	369	**18.45**	0.96	1984	**99.20**	2.23
2.6	20	587	**29.35**	1.21	1694	**84.70**	2.06
2.7	20	381	**19.05**	0.98	1440	**72.00**	1.90
2.8	25.2	647	**25.67**	1.01	1951	**77.42**	1.75

Table 4.40: Data collected for the $^{12}C(d, p_0)^{13}C$ reaction measurements taken at 135 and 150°.

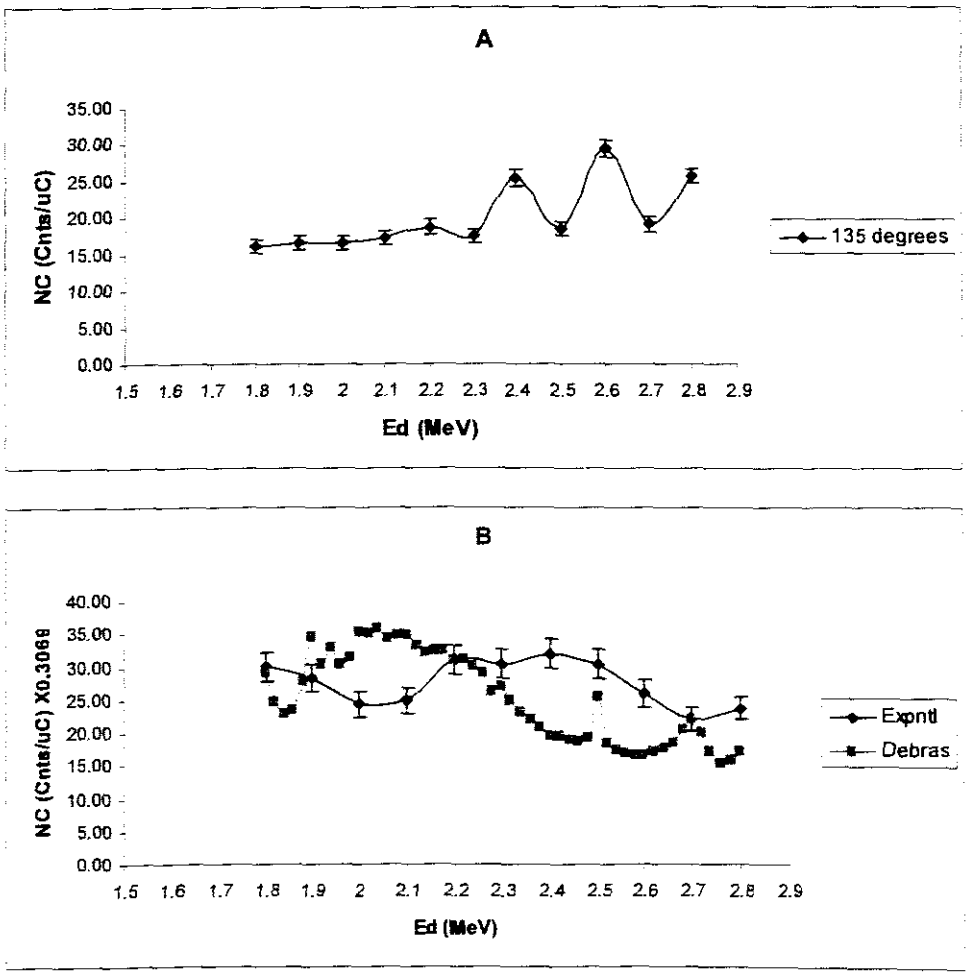

Figure 4.42: In A, Experimental plot of counts vs. incident beam energy for the $^{12}C(d, p_0)^{13}C$ measurements taken at 135° in B a 150° plot normalized at 2.2 MeV to the cross sections data found by Debras et al. at 135°[Deb77].

$E(MeV)$	$C_{inc}(\mu C)$	$Q_{d135°}$	$N_{c135°}(Counts/\mu C)$	σ	$Q_{d150°}$	$N_{c150°}(Counts/\mu C)$	σ
1.8	20	889	**44.45**	1.49	4927	**246.35**	0.35
1.9	20	845	**42.25**	1.45	4616	**230.80**	0.34
2	20	977	**48.85**	1.56	3344	**167.20**	0.29
2.1	20	657	**32.85**	1.28	3354	**167.70**	0.29
2.2	20.2	628	**31.09**	1.24	3394	**168.02**	0.29
2.3	20	658	**32.90**	1.28	3423	**171.15**	0.29
2.4	20	778	**38.90**	1.39	4404	**220.20**	0.33
2.5	20	1281	**64.05**	1.79	9299	**464.95**	0.48
2.6	20	1078	**53.90**	1.64	5980	**299.00**	0.39
2.7	20	1147	**57.35**	1.69	7663	**383.15**	0.44
2.8	25.2	1625	**64.48**	1.60	7603	**301.71**	0.35

Table 4.41: Data collected for the $^{12}C(d, p_1)^{13}C$ reaction measurements taken at 135 and 150°.

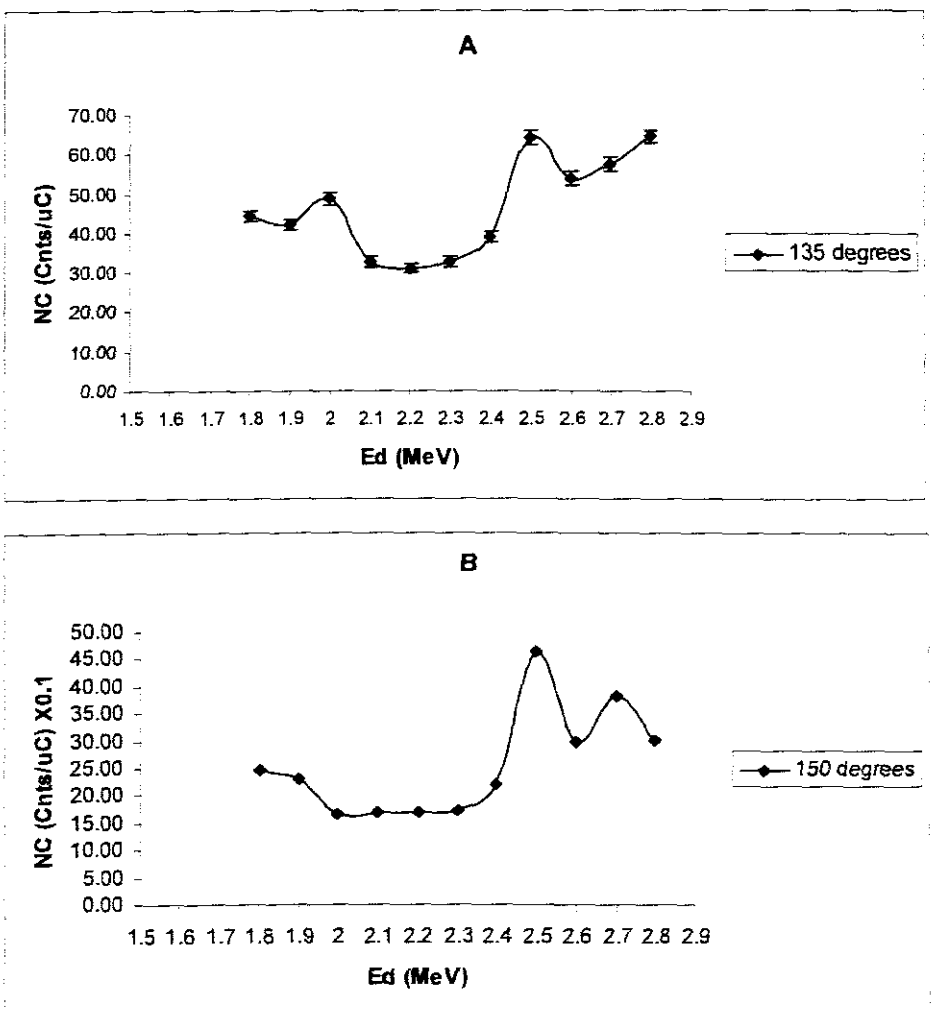

Figure 4.43: Experimental plot of counts vs. incident beam energy for the $^{12}C(d, p_1)^{13}C$ measurements taken at 135 and 150° respectively

$E(MeV)$	$C_{inc}(\mu C)$	$Q_{d135°}$	$N_{c135°}(Counts/\mu C)$	σ	$Q_{d150°}$	$N_{c150°}(Counts/\mu C)$	σ
1.8	20	1070	**53.50**	1.64	4546	**227.30**	3.37
1.9	20	1160	**58.00**	1.70	5131	**256.55**	3.58
2	20	2072	**103.60**	2.28	5287	**264.35**	3.64
2.1	20	962	**48.10**	1.55	4238	**211.90**	3.25
2.2	20.2	919	**45.50**	1.50	3720	**184.16**	3.02
2.3	20	952	**47.60**	1.54	3865	**193.25**	3.11
2.4	20	948	**47.40**	1.54	3725	**186.25**	3.05
2.5	20	960	**48.00**	1.55	4134	**206.70**	3.21
2.6	20	1085	**54.25**	1.65	5083	**254.15**	3.56
2.7	20	1049	**52.45**	1.62	6951	**347.55**	4.17
2.8	25.2	1463	**58.06**	1.52	6899	**273.77**	3.30

Table 4.42: Data collected for the $^{12}C(d, p_2)^{13}C$ reaction measurements taken at 135 and 150°.

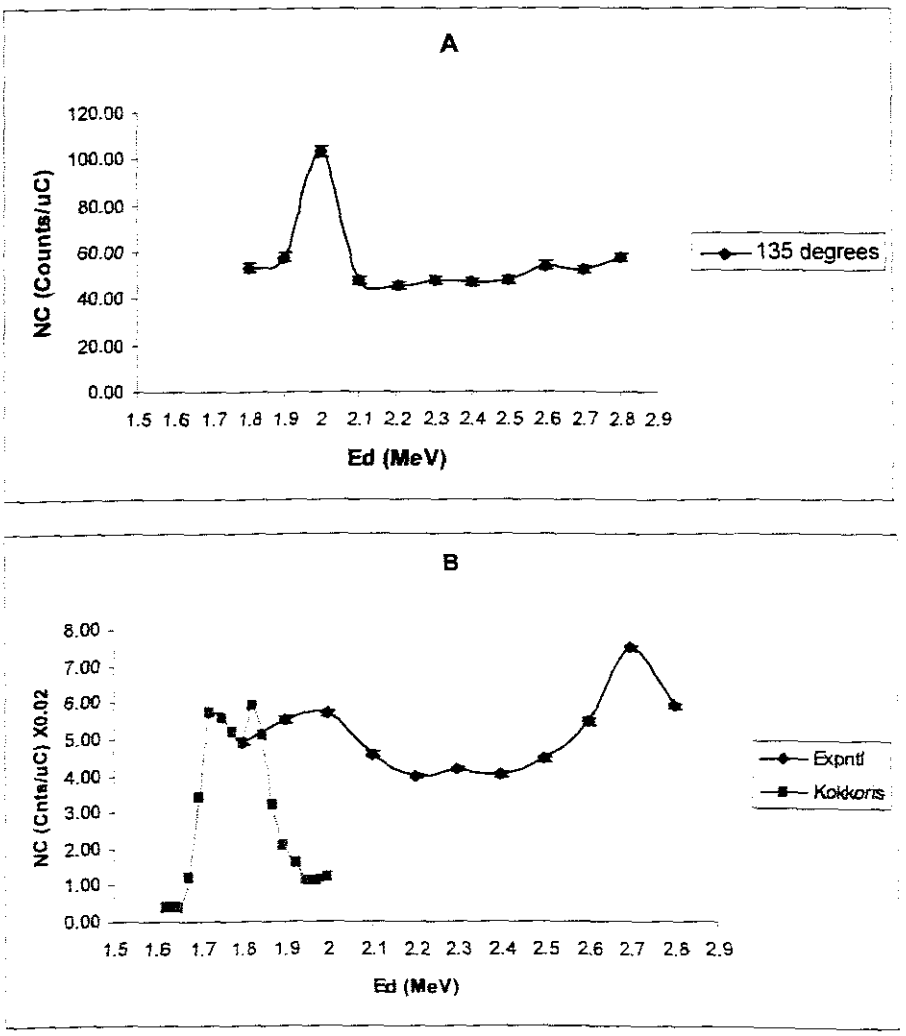

Figure 4.44: Experimental plots of counts vs. incident beam energy for the $^{12}C(d, p_2)^{13}C$ measurements taken at 135° and a 150° plot normalized to Kokkoris et al. cross section data at 1.8 MeV measured at 150° [Kok06].

$^{13}C(d, p_0)^{14}C$

This reaction was not observed during the carbon foil measurements due to the way the amplifier settings. Even though this reaction could be observed during the boron carbide silicate measurements, it's 135° counts were still very low. This led to poor statistics. These results were eventually not included in this presentation. The data and plot are presented in Table 4.43 and Fig. 4.45.

$E(MeV)$	$C_{inc}(\mu C)$	$Q_{d135°}$	$N_{c135°}(Counts/\mu C)$	σ	$Q_{d150°}$	$N_{c150°}(Counts/\mu C)$	σ
1.8	20	12	**0.60**	0.17	22	**1.10**	0.23
1.9	20	11	**0.55**	0.17	55	**2.75**	0.37
2	20	16	**0.80**	0.20	51	**2.55**	0.36
2.1	20	21	**1.05**	0.23	78	**3.90**	0.44
2.2	20.2	14	**0.69**	0.19	70	**3.47**	0.41
2.3	20	22	**1.10**	0.23	81	**4.05**	0.45
2.4	20	37	**1.85**	0.30	82	**4.10**	0.45
2.5	20	31	**1.55**	0.28	79	**3.95**	0.44
2.6	20	40	**2.00**	0.32	70	**3.50**	0.42
2.7	20	55	**2.75**	0.37	87	**4.35**	0.47
2.8	25.2	73	**2.90**	0.34	113	**4.48**	0.42

Table 4.43: Data collected for the $^{13}C(d, p_0)^{14}C$ reaction measurements taken at 135 and 150°.

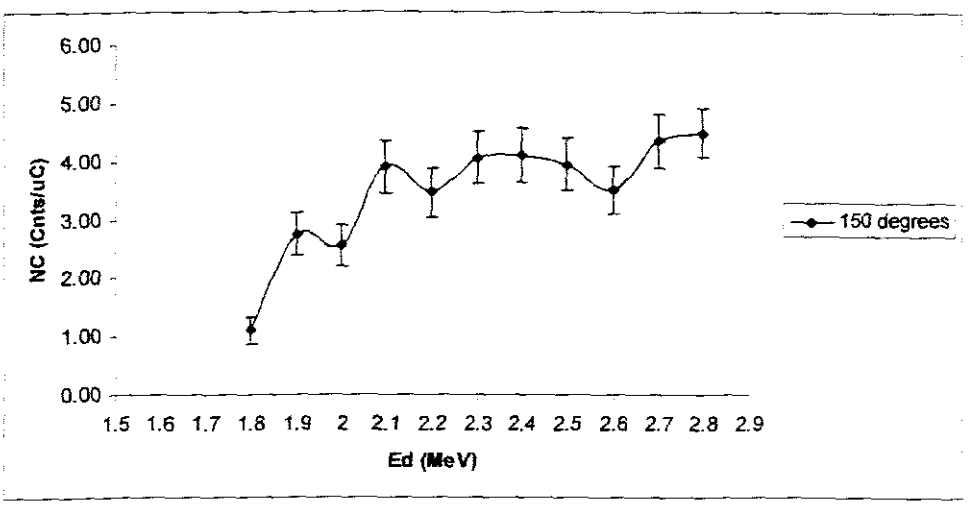

Figure 4.45: Experimental plot of counts vs. incident beam energy for the $^{13}C(d, p_0)^{14}C$ measurements taken at 150°.

$^{16}O(d, p_0)^{17}O$

The results of this reaction for boron carbide silicate measurements never followed the trends of the results of the same reaction found in carbon foil and boric acid measurements. This is suspected to be caused by experimental errors and the thickness of the target these results are presented in Table 4.44 and Fig. 4.46.

$^{16}O(d, p_1)^{17}O$

The plot of these results at 135° seemed to follow the trends observed on the results for carbon foil at incident energies less than 2.0 MeV, however, it started deviating at all energies greater than 2.0MeV. Table 4.45 and Fig. 4.47 present these results.

$E(MeV)$	$C_{inc}(\mu C)$	$Q_{d135°}$	$N_{c135°}(Counts/\mu C)$	σ	$Q_{d150°}$	$N_{c150°}(Counts/\mu C)$	σ
1.8	20	665	**33.25**	1.29	3453	**172.65**	0.29
1.9	20	507	**25.35**	1.13	4565	**228.25**	0.34
2	20	603	**30.15**	1.23	3581	**179.05**	0.30
2.1	20	420	**21.00**	1.02	2995	**149.75**	0.27
2.2	20.2	420	**20.79**	1.01	2873	**142.23**	0.27
2.3	20	470	**23.50**	1.08	2781	**139.05**	0.26
2.4	20	425	**21.25**	1.03	2509	**125.45**	0.25
2.5	20	479	**23.95**	1.09	2824	**141.20**	0.27
2.6	20	520	**26.00**	1.14	3181	**159.05**	0.28
2.7	20	585	**29.25**	1.21	3253	**162.65**	0.29
2.8	25.2	662	**26.27**	1.02	4583	**181.87**	0.27

Table 4.44: Data collected for the $^{16}O(d, p_0)^{17}O$ reaction measurements taken at 135 and 150°.

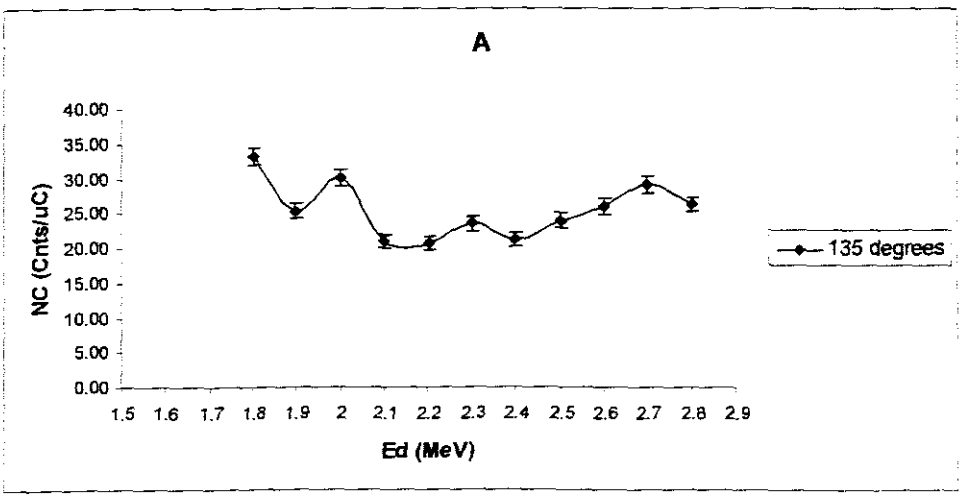

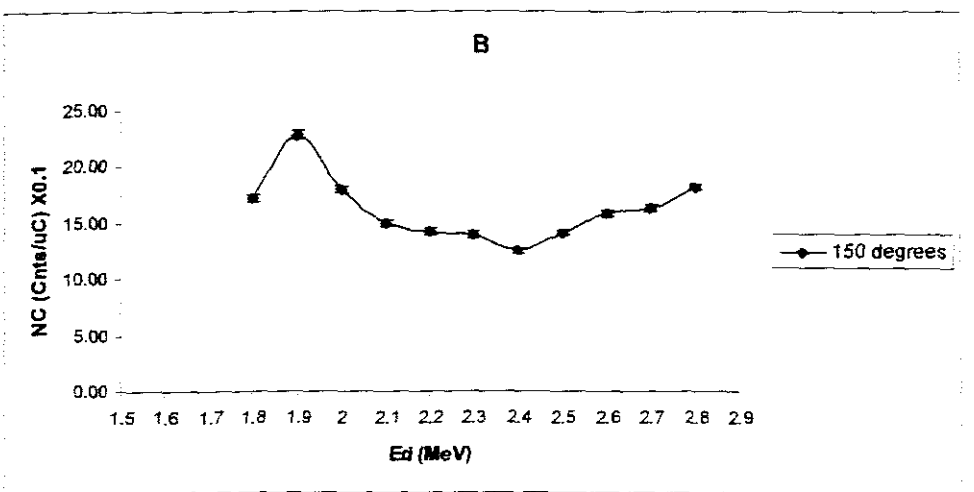

Figure 4.46: Experimental plot of counts vs. incident beam energy for the $^{16}O(d, p_0)^{17}O$ measurements taken at 135° and 150° respectively.

$E(MeV)$	$C_{inc}(\mu C)$	Q_{d135°	$N_{c135^\circ}(Counts/\mu C)$	σ	Q_{d150°	$N_{c150^\circ}(Counts/\mu C)$	σ
1.8	20	140	**7.00**	0.59	713	**35.65**	0.13
1.9	20	342	**17.10**	0.92	1375	**68.75**	0.19
2	20	217	**10.85**	0.74	2144	**107.20**	0.23
2.1	20	693	**34.65**	1.32	3519	**175.95**	0.30
2.2	20.2	733	**36.29**	1.34	3929	**194.50**	0.31
2.3	20	773	**38.65**	1.39	4768	**238.40**	0.35
2.4	20	718	**35.90**	1.34	4501	**225.05**	0.34
2.5	20	580	**29.00**	1.20	4384	**219.20**	0.33
2.6	20	530	**26.50**	1.15	3819	**190.95**	0.31
2.7	20	569	**28.45**	1.19	3733	**186.65**	0.31
2.8	25.2	704	**27.94**	1.05	4598	**182.46**	0.27

Table 4.45: Data collected for the $^{16}O(d, p_1)^{17}O$ reaction measurements taken at 135 and 150°.

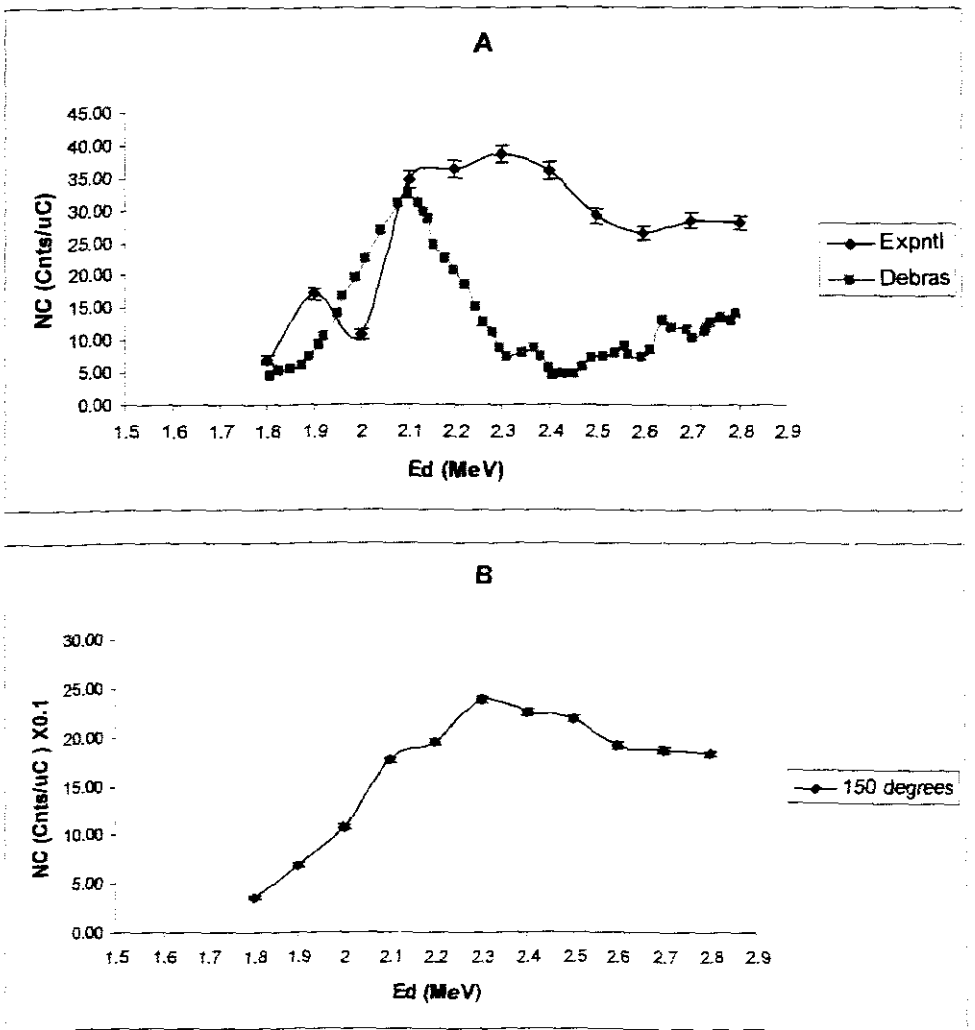

Figure 4.47: Experimental plot of counts vs. incident beam energy for the $^{16}O(d, p_1)^{17}O$ measurements taken at 135° normalized to Debras et al cross sections measurements at 2.1MeV and 150° respectively[Deb77].

$^{16}O(d, \alpha_0)^{14}O$

This reaction gave the same measurements as it did when the boric acid target was used. Both the 135° and 150° plot followed the trends of the same reaction on boric acid. These plots are presented in Table 4.46 and Fig. 4.48.

$E(MeV)$	$C_{in.}(\mu C)$	$Q_{d135°}$	$N_{c135°}(Counts/\mu C)$	σ	$Q_{d150°}$	$N_{c150°}(Counts/\mu C)$	σ
1.8	20	673	**33.65**	1.30	92	**4.60**	0.36
1.9	20	485	**24.25**	1.10	126	**6.30**	0.35
2	20	603	**30.15**	1.23	185	**9.25**	0.33
2.1	20	409	**20.45**	1.01	181	**9.05**	0.30
2.2	20.2	374	**18.51**	0.96	206	**10.20**	0.28
2.3	20	431	**21.55**	1.04	192	**9.60**	0.28
2.4	20	424	**21.20**	1.03	290	**14.50**	0.28
2.5	20	418	**20.90**	1.02	287	**14.35**	0.27
2.6	20	484	**24.20**	1.10	332	**16.60**	0.27
2.7	20	486	**24.30**	1.10	307	**15.35**	0.27
2.8	25.2	638	**25.32**	1.00	502	**19.92**	0.24

Table 4.46: Data collected for the $^{16}O(d, \alpha_0)^{14}N$ reaction measurements taken at 135 and 150°.

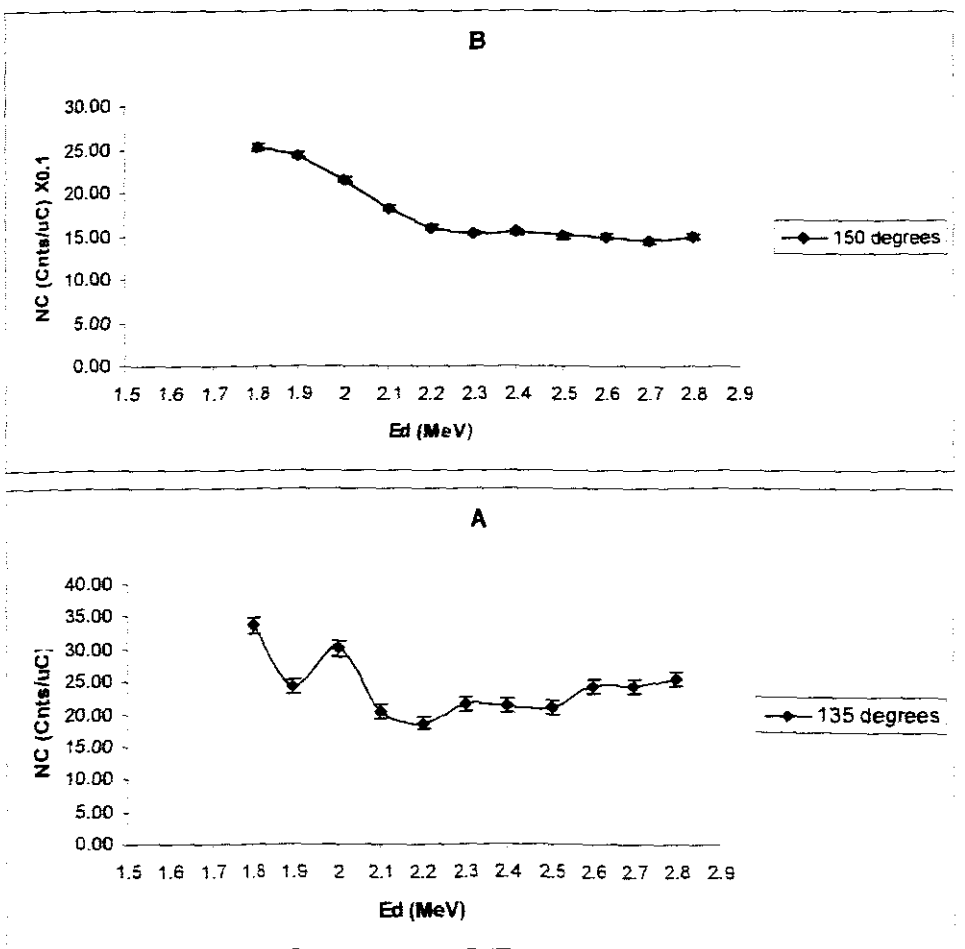

Figure 4.48: Experimental plot of counts vs. incident beam energy for the $^{16}O(d, \alpha_0)^{14}N$ measurements taken at 135 and 150° respectively.

4.2.7 Results of the $^3He^+$ on B_4C/SiO_2.

These results were not presented here, however it is believed that they would have behaved the same as the ones for D^+ on B_4C/SiO_2. The results of the D^+ on B_4C/SiO_2, especially the ones of deuterons on boron targets seemed to be the same as the ones of deuterons on boron nuclei in boric acid. Thus this would have been like the repetition of the $^3He^+$ on the carbon foil and boric acid, so they were not included.

Chapter 5
Conclusion and discussions

The aim of this study was to measure nuclear reaction cross sections of light ions (specifically deuterons and helium-3 particles) on boron and carbon isotopes in the 1.8 – 2.8 MeV incident energy range at 135^o and 150^o scattering angles. This was partially achieved by calculating the number of detected counts for the above mentioned nuclear reactions at the above mentioned incident energy range and scattering angles.

The way used to solve this problem was to backscatter some deuterons from the surface of an oxygen surface contaminated carbon foil at the required incident energy range and scattering angles. However the method failed due to some peak pile-ups (since no filtering method was used), which created uncertainties in the number of counts gotten for the backscattered deuterons. The uncertainties brought about variations in the correct factor used to normalize the theoretical RBS work and the experimental one. The correction factor was expected to be the same for the deuterons and $^3He^+$ backscattered from ^{12}C and ^{16}O on the surface, however different factors were obtained. This factor was then going to be used to multiply the collected data of normalized counts to give nuclear reaction cross sections data.

The other method that could have been tried was calculating the mass fractions of elements on the target sample. Since the normalized counts data would have been normalized to some literature cross sections data, then the mass fractions would be used to divide the normalization factors. This would to give one correction factor to be used to calculate cross sections for all the reactions measurements. This method was rendered by the composition of the surface of the oxygen surface contaminated carbon foil, which was not known.

Measuring of number of detected counts or cross sections in larger incident energy steps makes it a bit difficult to have confidence in the results. This is caused by the

smaller incident energy steps of the available cross sections data, which bring about uncertainties of the missing data between the energy steps.
It is recommended that a gas cell ΔE proportional counter is used for particle identification. Another technique that would be very useful for distinguishing emitted particles is pulse shape analysis.

The second method of finding the composition of the target could not be implemented since the composition of the oxygen surface contaminated carbon foil is not known.

To avoid missing some data in the number of detected counts or cross sections measurements at some data points, smaller incident energy steps should be considered.

This study has shown that larger scattering angles can give better cross sections or detected counts at lower incident energies. This was seen when very low numbers of detected counts were observed at 135° compared to at 150° in most reactions. And this led to some of the 135° measurements exclusion because of their poor statistics.

Appendix A

Statistics of radiation events.

Since there are always uncertainties associated with experimental measurements, it becomes very important to do statistical calculations for reduction of uncertainties and to have confidence in the measurements.

According to statistics of radiation events, the standard deviation in number of detected counts is calculated using:

$$\sigma_s = \sqrt{Q_d}$$

Where Q_d is the number of detected particles.

Then the error is calculated from the standard deviation depending on the level of confidence used. For instance for 68.0% level of confidence, error = σ, for 95.0% level of confidence error =2σ and for 99.7% level of confidence error =3σ.

% error is then calculated by: $\frac{\sqrt{Q_d}}{Q_d} \times 100\%$ [htt04].

Appendix B

$E(MeV)$	$\sigma(mb)$
1.8	29.2
1.82	24.8
1.84	22.9
1.86	23.5
1.88	27.7
1.9	34.5
1.92	30.4
1.94	33
1.96	30.5
1.98	31.3
2	35.4
2.02	35
2.04	35.8
2.06	34.4
2.08	34.9
2.1	34.9
2.12	33.3
2.14	32.1
2.16	32.5
2.18	32.4
2.2	31
2.22	31.1
2.24	30.1
2.26	29.2
2.28	26.2
2.3	27
2.32	24.9
2.34	23.2
2.36	22.1
2.38	20.7
2.4	19.6
2.42	19.4
2.44	18.9
2.46	18.8
2.48	19.3
2.5	25.4
2.52	18.4
2.54	17.3
2.56	16.8
2.58	16.5
2.6	16.7
2.62	17.1
2.64	17.7
2.66	18.5
2.68	20.5
2.7	22.1
2.72	19.9
2.74	17.1
2.76	15.4
2.78	15.8
2.8	17.1

A

E(MeV)	$\sigma(mb)$
1.624	0.37
1.648	0.4
1.673	1.2
1.698	3.4
1.723	5.7
1.749	5.6
1.773	5.2
1.799	4.9
1.824	5.9
1.849	5.1
1.874	3.2
1.899	2.1
1.924	1.6
1.949	1.1
1.974	1.1
1.999	1.2

B

Table A and B data collected by Debras for the $^{12}C(d, p_0)^{13}C$ reaction at 135°[Deb77]. B data found by Kokkoris for the $^{12}C(d, p_2)^{13}C$ [Kok06] resepectively

$E(MeV)$	$\sigma(mb)$
1.808	1.61
1.831	1.68
1.853	1.58
1.879	1.74
1.9	1.7
1.947	1.8
1.989	1.73
2.038	1.81
2.079	1.83
2.106	1.95
2.127	2.12
2.144	2.23
2.165	2.5
2.19	2.51
2.209	2.73
2.23	2.81
2.256	2.73
2.279	2.4
2.302	2.12
2.279	2
2.322	1.74
2.35	1.74
2.399	1.49
2.442	1.74
2.486	2.03
2.531	2.18
2.578	2.28
2.623	2.1
2.673	2.1
2.721	1.81
2.768	1.77
2.813	1.84

C

$E(MeV)$	$\sigma(mb)$
1.808	4.463
1.825	5.385
1.849	5.593
1.877	6.109
1.89	7.337
1.911	9.178
1.924	10.51
1.951	13.98
1.964	16.64
1.987	19.5
2.011	22.57
2.044	26.86
2.081	30.95
2.102	32.38
2.123	31.06
2.133	29.63
2.144	28.51
2.155	24.64
2.18	22.6
2.201	20.56
2.222	18.42
2.244	15.16
2.258	12.72
2.282	10.99
2.293	8.845
2.311	7.318
2.342	8.039
2.366	8.758
2.383	7.435
2.401	5.601
2.408	4.582
2.429	4.79
2.453	4.693
2.47	5.819
2.487	7.149
2.514	7.461
2.538	7.976
2.562	9.001
2.569	7.742
2.597	7.477
2.617	8.4
2.64	12.9
2.661	11.88
2.692	11.68
2.703	10.25
2.727	11.48
2.734	12
2.74	12.71
2.761	13.43
2.785	13.03
2.795	14.15

D

Table C and D cross section data collected by Debras for the $^{16}O(d, p_0)^{17}O$ and $^{16}O(d, p_1)^{17}O$ reaction at 135° respectively [Deb77].

$E(MeV)$	$\sigma(mb)$
1.774	0.06
1.878	0.17
1.957	0.15
2.039	0.25
2.088	0.43
2.152	0.43
2.194	0.55
2.232	0.49
2.272	0.63
2.31	0.92
2.356	1.13
2.393	1.49
2.432	1.74
2.473	2.02
2.513	2.31
2.551	2.9
2.596	2.97
2.641	3.16
2.681	3.94
2.721	4.04
2.769	4.13
2.823	3.87

E

$E(MeV)$	$\sigma(mb)$
1.772	0.062
1.879	0.144
1.963	0.217
2.037	0.414
2.088	0.474
2.142	0.798
2.187	0.914
2.227	1.475
2.255	2.37
2.298	2.575
2.34	3.706
2.376	3.787
2.423	3.696
2.481	2.28
2.525	2.642
2.573	2.282
2.619	2.322
2.665	1.999
2.715	1.927
2.755	2.035
2.809	1.54

F

$E(MeV)$	$\sigma(mb)$
1.777	0.14
1.886	0.24
1.951	0.34
2	0.48
2.045	0.65
2.096	0.98
2.155	1.25
2.198	1.25
2.216	1.49
2.245	1.71
2.274	2.14
2.285	2.61
2.331	2.93
2.368	3.2
2.466	2.46
2.509	2.03
2.55	1.57
2.593	1.26
2.631	0.94
2.692	0.5
2.733	0.43

G

Table E, F and G cross section data collected by Kuan et al. for the $^{12}C(^3He, p_0)^{13}C$, $^{12}C(^3He, p_1)^{13}C$ and $^{12}C(^3He, p_2)^{13}C$ reaction at 135° respectively [Kua64].

Appendix C

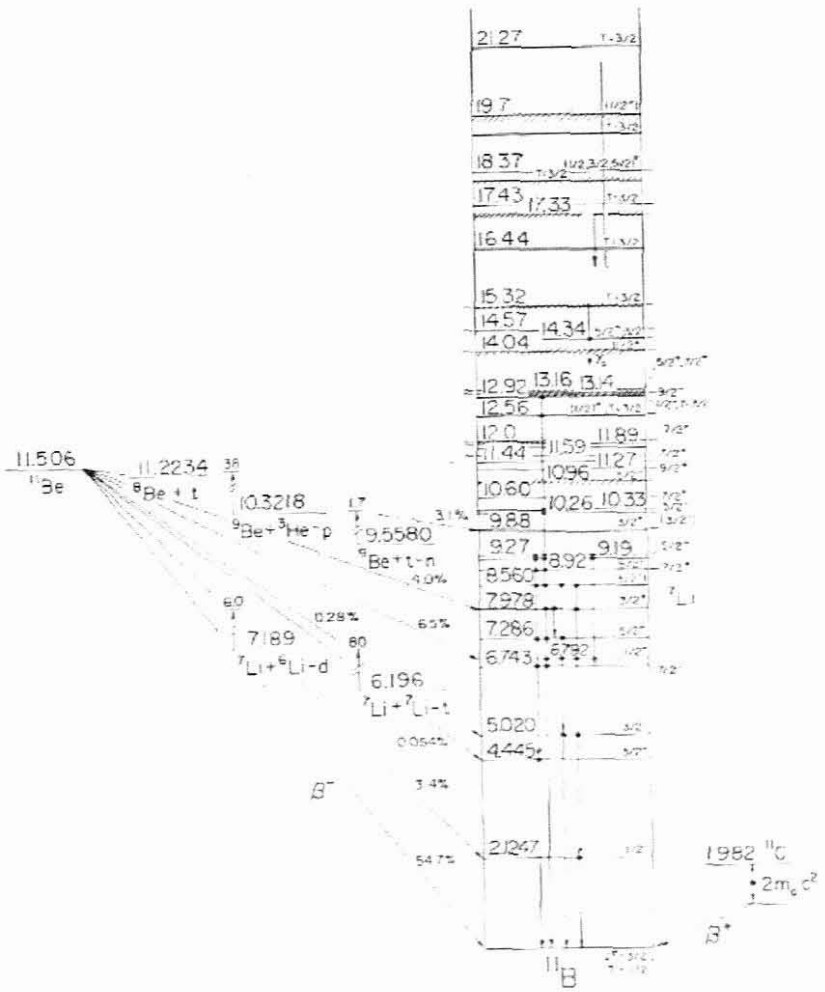

Figure 1: Energy level schemes diagram of ^{11}B [AJZ88].

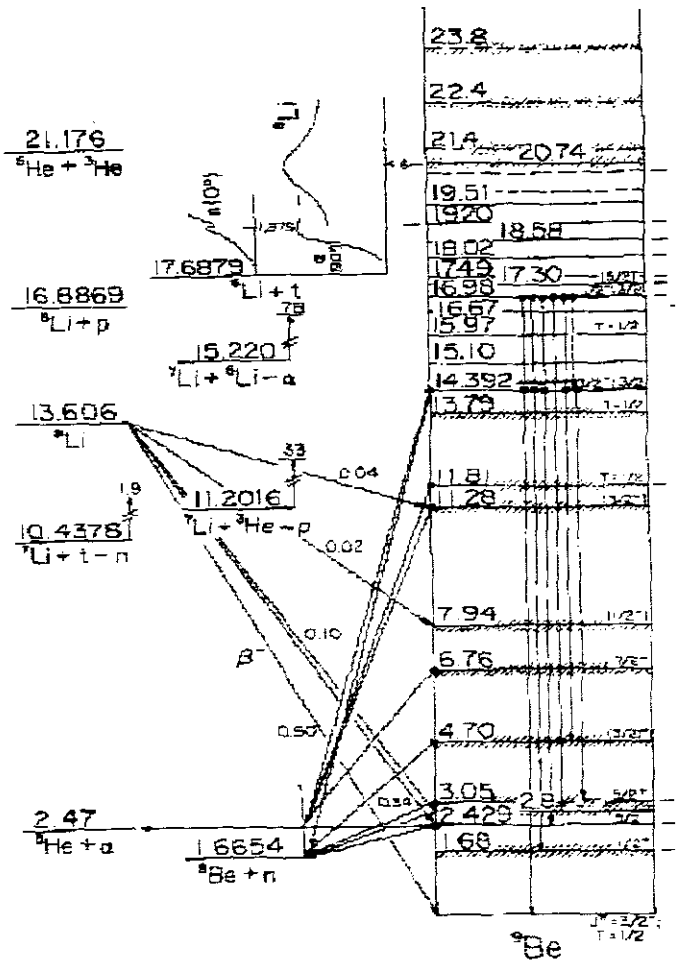

Figure 2: Energy level schemes diagram of ^{9}Be [AJZ88].

References.

[AJZ88] F. Ajzenberg-selove, in: Nucl. Phys. A490 (1988) 110

[AJZ90] F. Ajzenberg-selove, Nucl. Phys. A506 (1990) 8

[Bir89] J.R.Bird, in: Ion Beams for Materials Analysis, eds. J.R. Bird and J.S. Williams, Academic Press, San Diego, (1989)

[Chu78] Wei-Kan Chu, in: Backscattering Spectrometry, eds. Wei-Kan Chu, James W. Mayer and Marc-A, Academic Press, San Francisco, (1978)

[Deb77] G. Debras, G. Deconnick, J. Rad. Chem. 38 (1977) 193

[Del05] G. Della Mea, A. Patella, S Restello, V. Rigato and A. Vomiero, Nucl. Instr. And Meth. B240 (2005) 804

[htt01] http://education.jlab.org/itselemental/ele005.html taken on 06/06/06

[htt02] http://education.jlab.org/itselemental/ele006.html taken on 06/06/06

[htt03] http://education.jlab.org/itselemental/ele008.html taken on 06/06/06

[htt04] http://www.sprawls.org/ppmi2/STATS/index.html taken on 23/08/07

[Jia02] Jiarui Lui, Xinming Lu, Xuemei wang and Wei-Kan Chu, Nucl. Instr. and Meth. B 190 (2002) 107.

[Jia04] W Jiang, V. Shutthandan, S. Thevuthasan, D. E. McCready and W.J. Weber Nucl. Instr. and Meth. B 222 (2004) 538

[Jul05] Julien L. Colaux and G. Terwagne, Nucl. Instr. and Meth. B 240 (2005) 429–433

[Kno79] Glenn F. Knoll, (eds.), Radiation Detection and Measurement, John Wiley n and Sons, Canada (1979).

[Kok06] M. Kokkoris, S. Kossionides, Ch. Zarkadas, A. Lagoyannis, R. Vlastou, C. T. Papadopoulos, A. Kontos, Nucl. Instr. and Meth. B 249 (2006) 77-80

[Kua64] H. M. Kuan and T. W. Bonner, J. R. Risser, Nucl. Phys. 51 (1964) 481

[May98] M. Mayer, A. Annen, W Jacob, and S. Grigull, Nucl. Instr. and Meth. B 143 (1998) 244

[Mar56] J. B. Marion and G. Weber, Phys. Rev., 103 (1956), 167

[McI92] L.C. McIntyre, Jr, J.A. Leavitt, M.D. Adshbaugh, Z. Lin and J.O. Stoner, Jr, Nucl. Instr. and Meth B 66 (1992) 221.

[Pur63] K. H Purser and B.H. Widenthal, Nucl. Phys. 44 (1963) 22

[Ter97] G. Terwagne, Nucl. Instr. and Meth. B122 (1997) 1

[Tes95] J.R. Tesmer, M. Nastasi (Eds.), Handbook of Modern Ion beam Materials Analysis, Materials Research Society, Pittsburgh, PA, (1995).

[www01] http://www.ulg.ac.be/ipne/iba/html taken on 03/04/06

[www02] http://www.iop.org/EJ/abstract/0022-3727/32/22/320 taken on 07/02/06.

[www03] http://www.weizmann.ac.il/fluids/klein/techniques_nra.html

[www04] http://www.webelements.com/webelements/elements/text/C/geol.html taken on 06/06/06

[www05] http://wwww.ibl.gov/abc/wallchart/teachersguide/pdf/chap11.pdf taken on 15/06/06

[www06] http://www.physics.nd.edu/pdf/20005%20reu%20papers/rasmussen.pdf taken on 15/06/06

[www07] http://www.scienceclarified.com/Oi-Ph/Particle-Accelerators.html taken on 20/06/06

[www08] http://www.pbmr.co.za/download/FuelSystem.pdf taken on 14/09/06.

[www09] http://www-nds.iaea.org/ibandl/ taken on 07/10/06